Managing light in engineered nonlinear optical structures

Xin Chen

November 2017

A THESIS SUBMITTED FOR THE DEGREE OF
DOCTOR OF PHILOSOPHY

OF THE AUSTRALIAN NATIONAL UNIVERSITY

Department of Laser Physics Centre

Research School of Physics and Engineering

College of Physical and Mathematical Sciences

The Australian National University

Declaration

This thesis reports the research I conducted during 2013 and 2017, at the Department of Laser Physics Centre, the Australian National University, Canberra, Australia.

To the best of my knowledge, the material reported here is original except where acknowledged and reference in appropriate manner. It has not been previously published by others, or submitted in whole or in part for any university degrees.

Xin Chen

November 2017

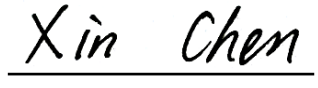

Acknowledgement

I would like to express my most sincere gratitude to all the people who directly and indirectly helped me during my PhD study.

First of all, I would like to thank to my supervisory panel: Professor Wieslaw Krolikowski, Dr. Yan Sheng, and Dr. Vladlen Shvedov. It is my great honour to be a student of Professor Wieslaw Krolikowski. His broad knowledge, deep insights and scientific visions are always inspirational. Every time I talk to him I can learn something new and get much useful advice on my work. I would also like to thank him for supporting my attendance to those conferences and the research travel to Texas A&M University at Qatar. My special thanks go to Dr. Yan Sheng, who is always inspiring and encouraging me, especially when I get stuck in experiment. Thanks to Dr. Vladlen Shvedov for useful discussions on my projects.

Thanks to all the staff and colleagues of Research School of Physics and Engineering (RSPE). In particular, I would like to thank Dr. Pawel Karpinski for teaching me how to control experimental hardware using MATLAB. He also shared with me his experiences and skills in conducting experiments with femtosecond lasers at the beginning of my PhD study. Thanks to Professor Barry Luther-Davis, Dr. Xin Gai, Dr. Cyril Hnatovsky and Professor Rode Andrei for their professional support in laser maintenance and adjustment. To Dr. Rongping Wang who offered me valuable advice on mechanical polishing. To Associate Professor Duk-Yong Choi who trained me and also helped me on chemical etching. To John Bottega and Craig MacLeod from the mechanical workshop for the numerous parts they manufactured for me, without which my experiments would be difficult to conduct. I am also grateful that I was surrounded by so many talented and friendly collaborators and colleagues in this school, like Professor Jiandong Ye, associate Professor Fangfang Ren, Dr. Xiangyuan Cui, Dr. Li Li, associate Professor Xiaopeng Hu, Dr. Yi Yu, Dr. Kunlun Yan, Dr. Pan Ma, Mr Tianxiang Xu, Dr. Zhisong Qu, Mr Haitao Chen, Dr. Qixiang Zhao, Dr.

Xinyu Yang, Dr. Tong Wang, Dr. Wenguo Zhu, Dr. Siwei Xu, Dr. Fajun Li, Dr. Jun Cheng and Mr Haijie Zuo, and this list goes on and on. To LPC department administrator Ms. Sonia Padrun, RSPE HDR administrator Ms. Liudmila Mangos and Ms. Karen Nulty, Centre for Plasmas and Fluids Plasma Research Laboratory administrator Ms. Uyen Nguyen and Mrs. Susie Radovanovic, for their great efforts to handle students' administrative work.

None of my projects can go forward without the essential equipment and technical support from Centre for Advanced Microscopy (CAM). Thanks to Mr. Daryl Webb, who offered me enormous help in using and analyzing results from confocal microscopy. Otherwise my projects cannot proceed smoothly. Thanks to Dr. Hua Chen for his help on SEM measurement. Thanks to CAM administrator Ms. Josie Smith, for her kind assistance in getting my access to the facilities in CAM.

During my PhD study, Professor Wieslaw Krolikowski offered me an opportunity to visit his research group in the Science Program at Texas A&M University at Qatar. It was a very eye-opening experience for me. I worked there for four weeks, Professor Wieslaw Krolikowski and Dr. Krzysztof Świtkowski provided me continuing guidance in laboratory and also great help in life in Doha.

My friends in Australia deserve a special acknowledgement. To Mr. Naiyin Wang, Mr. Zhe Li, Ms. Na Yu, Ms. Kunrong Yang, Mr. David Lockwood, Dr. Fenglin Xian, Dr. Yujie Ma, Mr. Peng He, Dr. Weizong Xu, Dr. Guogang Zhang and Mr. Rongping Tang. Doing a PhD abroad is hard, but all these nice friends and peers make my life in Canberra much easier.

I acknowledge the financial support of the China Scholarship Council and Australian National University (ANU) Tuition Fee Scholarship, which made my study at ANU possible.

Last but not least, I would like to express my deepest gratitude to my family members, my father and mother, who have always been supportive, especially in the hard times of my life. And to Bijun, my wife, thanks for your accompany and thank you for everything you did for me!

Abstract

Optical frequency conversion process allows one to generate coherent light in wavelength ranges that are not readily available. It is well known that because of dispersion, the phase mismatch between interacting waves leads to low efficiency of frequency generation. Quasi-phase matching (QPM) that uses crystals with a spatial modulation of the second-order nonlinear coefficient $\chi^{(2)}$, also known as nonlinear photonic crystals (NPC), is an important technique to solve the phase mismatch problem. With proper design of the quadratic nonlinearity modulation, one can not only obtain efficient frequency conversion, but also make diverse applications possible, including beam and pulse shaping, all-optical processing, entangled photon generation and manipulation.

This thesis explores the fabrication, properties and application of various types of NPCs. In particular, we discuss NPC fabricated in single-domain ferroelectric crystals by using all-optical poling with near infrared femtosecond laser pulses and high voltage electric poling; as grown ferroelectric crystals with random sized ferroelectric domains; and orientation patterned semiconductors grown by hydride vapour phase epitaxy. Specifically, this research work involved the following topics:

1. Systematic investigation of a novel technique of direct writing of ferroelectric domains using near-infrared femtosecond laser pulses. Domain inversion in a $LiNbO_3$ crystal was realized by its illumination with ultra-short infrared pulses only, without applying any external electric field. The quality of the inverted domains was characterized by Cerenkov second harmonic microscopy (CSHM) and selective chemical etching, respectively. The optically poled regions were not confined to the surface, but extended deep into the crystal. This is a significant result surpassing the capability of the traditional ultraviolet (UV) all-optical poling technique. As an experimental demonstration,

a QPM structure in a $LiNbO_3$ channel waveguide was fabricated by this infrared laser poling technique allowing efficient frequency doubling of 815 nm light beam.

2. Experimental studies of the application of as-grown calcium barium niobate (CBN) crystal for a broadband frequency conversion. This frequency conversion process is similar to broadband harmonic generation in commonly used strontium barium niobate (SBN) crystal, but results in higher conversion efficiency reflecting a larger effective nonlinear coefficient of the CBN crystal. We also analyzed the spatial distribution of the intensity of the generated radiation as well as its polarization properties. This study contributes to a simpler and more efficient realization of broadband frequency conversion devices in a wide class of nonlinear optical media.

3. Experimental studies of multistep cascading frequency conversion processes in a custom-cut periodically poled lithium niobate crystal. By employing the total internal reflection inside the sample, we combined quasi-phase matched collinear and Cerenkov nonlinear sum frequency mixing to achieve enhanced fourth harmonic generation in a single periodically poled lithium niobate crystal.

4. Experimental investigation of nonlinear diffraction in an orientation-patterned semiconductor. By employing a new transverse geometry of interaction, nonlinear Cerenkov, nonlinear Raman-Nath and nonlinear Bragg diffractions were identified according to different configurations of quasi-phase matching conditions. The study extends the concept of transverse nonlinear parametric interaction toward infrared frequency conversion in semiconductors. It also offers an effective nondestructive method of visualization and diagnostic of spatial variations of second-order nonlinearity inside semiconductors.

Publications

Journal articles

[1] **Xin Chen**, Pawel Karpinski, Vladlen Shvedov, Kaloian Koynov, Bingxia Wang, Jose Trull, Crina Cojocaru, Wieslaw Krolikowski, and Yan Sheng. Ferroelectric domain engineering by focused infrared femtosecond pulses. Applied Physics Letters, Vol. 107, Iss. 14, pp. 141102, 2015.

[2] **Xin Chen**, Pawel Karpinski, Vladlen Shvedov, Andreas Boes, Arnan Mitchell, Wieslaw Krolikowski, and Yan Sheng. Quasi-phase matching via femtosecond laser induced domain inversion in lithium niobate waveguides. Optics Letters, Vol. 41, No. 11, pp. 2410-2413, 2016.

[3] **Xin Chen**, Krzysztof Switkowski, Xiaopeng Hu, Wieslaw Krolikowski, and Yan Sheng. Enhanced fourth harmonic generation via nonlinear Cerenkov interaction in periodically poled lithium niobate crystal. Optics Express, Vol. 24, No. 26, pp.29948-29954, 2016.

[4] **X. Chen**, V. Shvedov, P. Karpinski, K. Koynov**,** A. Boes, A. Mitchell, J. Trull, C. Cojocaru, W. Krolikowski, and Y. Sheng. Ferroelectric domain patterning with ultrafast light. Optics & Photonics News, Vol. 27, special issue: Optics in 2016, pp.50, 2016.

[5] **Xin Chen**, Pawel Karpinski, Vladlen Shvedov, Bingxia Wang, Jose Trull, Crina Cojocaru, Andreas Boes, Arnan Mitchell, Wieslaw Krolikowski, and Yan Sheng. Two-dimensional domain structures in Lithium Niobate via domain inversion with ultrafast light. Photonics Letters of Poland, Vol. 8, No. 2, pp. 33-35, 2016.

[6] Yan Sheng, **Xin Chen**, Tadeusz Lukasiewicz, Marek Swirkowicz, Kaloian Koynov, and Wieslaw Krolikowski. Calcium barium niobate as a functional material for broadband optical frequency conversion. Optics Letters, Vol. 39, No. 6, pp. 1330-1332, 2014.

[7] Pawel Karpinski, **Xin Chen**, Vladlen Shvedov, Cyril Hnatovsky, Arnaud Grisard, Eric Lallier, Barry Luther-Davies, Wieslaw Krolikowski, and Yan Sheng, "Nonlinear diffraction in orientation-patterned semiconductors", Optics Express, Vol.23, No. 11, pp. 14903-14912, 2015.

[8] Vladlen Shvedov, Pawel Karpinski, Yan Sheng, **Xin Chen**, Wenguo Zhu, Wieslaw Krolikowski, and Cyril Hnatovsky. Visualizing polarization singularities in Bessel-Poincaré beams. Optics Express, Vol. 23, No. 9, pp. 12444-12453, 2015.

Conference papers

[1] **Xin Chen**, Pawel Karpinski, Vladlen Shvedov, Kaloian Koynov, Bingxia Wang, Jose Trull, Crina Cojocaru, Wieslaw Krolikowski, and Yan Sheng. Direct writing of inverted domains in lithium niobate using infrared femtosecond pulses. International Conference on Nanoscience and Nanotechnology (ICONN), 2016.

[2] **Xin Chen**, Pawel Karpinski, Vladlen Shvedov, Cyril Hnatovsky, Andreas Boes, Arnan Mitchell, Wieslaw Krolikowski, and Yan Sheng. Direct writing of inverted domain patterns in lithium niobate waveguides using femtosecond infrared pulses. Conference on Lasers and Electro-Optics (CLEO): Applications and Technology, paper ATu4K.4, 2016.

[3] **Xin Chen**, Pawel Karpinski, Vladlen Shvedov, Cyril Hnatovsky, Andreas Boes, Arnan Mitchell, Wieslaw Krolikowski, and Yan Sheng. Ferroelectric domain engineering using infrared femtosecond laser and its application to optical frequency conversion. Photonics and Fiber Technology, paper NM3A.6, 2016 (**invited talk**).

[4] **Xin Chen**, Wieslaw Krolikowski, and Yan Sheng. Ultrafast-laser-inscribed nonlinear photonic crystals for frequency conversion. Collaborative Conference on Materials Research (CCMR), 2017.

[5] Pawel Karpinski, **Xin Chen**, Vladlen Shvedov, Cyril Hnatovsky, Arnaud Grisard, Eric Lallier, Barry Luther-Davies, Wieslaw Krolikowski, and Yan

Sheng. Visualization of the Internal Structure of Orientation-Patterned III-V Semiconductors. Conference on Lasers and Electro-Optics (CLEO): Science and Innovations, paper STh1H.6, 2015.

Acronyms and Symbols

AC	Alternating current
AFM	Atomic force microscopy
$BaNb_2O_6$	Barium niobate
$BaTiO_3$	Barium titanate
BN	Barium niobate
BPM	Birefringent phase matching
CBN	Calcium barium niobate
CLN	Congruent lithium niobate
CSHG	Cerenkov second harmonic generation
CSHM	Cerenkov second harmonic microscopy
CW	Continuous wave
DFG	Difference frequency generation
EFP	Electric field poling
Er: YAG	Erbium-doped yttrium aluminium garnet laser
FB	Fundamental beam
FHG	Fourth harmonic generation
GaAs	Gallium arsenide
GaN	Gallium nitride
GaP	Gallium phosphide
HF	Hydrofluoric acid
HNO_3	Hydrogen nitrate
HVPE	Hydride vapour phase epitaxy
InGaAs	Indium gallium arsenide
IR	Infrared
KDP	Potassium dihydrogen phosphate
KTA	Potassium titanyl arsenate

$KTiOAsO_4$	Potassium titanyl arsenate
LAP	Light assisted poling
$LiNbO_3$	Lithium niobate
$LiTaO_3$	Lithium tantalate
LN	Lithium niobate
MgO: LN	Magnesium-doped lithium niobate
NA	Numerical aperture
NLD	Nonlinear diffraction
NPC	Nonlinear photonics crystals
OP	Orientation patterned
OPA	Optical parametric amplifiers
OP-GaAs	Orientation patterned gallium arsenide
OPO	Optical parametric oscillators
PFM	Piezoresponse force microscopy
PI	Poling inhibition
PPLN	Perodically poled lithium niobate
QCL	Quantum cascade laser
QPM	Quasi-phase matching
QPOS	Quasi-periodic optical supperlattice
$RbTiOPO_4$	Rubidium titanyl phosphate
RLV	Reciprocal lattice vector
RTP	Rubidium titanyl phosphate
SBN	Strontium barium niobate
SFM	Sum frequency mixing
SHG	Second harmonic generation
SN	Strontium niobate
SNDM	Scanning nonlinear dielectric microscopy
$SrNb_2O_6$	Strontium niobate

SVEA	Slowly varying envelope approximation
TEM	Transmission electron microscopy
THG	Third harmonic generation
TTB	Tetragonal tungsten bronze
UV	Ultra-violet
WGM	Whispering gallery mode
ZnSe	Zinc selenide

Table of Contents

List of Figures

List of Tables

Chapter 1 Introduction

1.1 Laser and nonlinear optics

Light amplification by stimulated emission of radiation, also known as laser, is one of the most revolutionary invention in the twentieth century. Schawlow and Townes proposed a technique for the generation of laser in the infrared and visible region of the spectrum in 1958 [1]. After that, lots of researchers compete with each other for realization of the first laser. In 1960, Mainman created the first laser at the Hughes Research Laboratory in California, by shining a high power flash lamp on a ruby rod with silver coated surfaces [2].

The invention of laser marks the beginning of an exciting and extremely active research field, nonlinear optics, which describes the light-matter interaction in optical media, in which the dielectric polarization P responds nonlinearly to the electric field E, of the light. The extraordinary high intensity electric field of laser beams make nonlinear phenomena observable. The first nonlinear phenomenon was second harmonic generation reported by P. A. Franken, et al. in 1961 [3]. They doubled the frequency of a pulsed ruby laser (694.3 nm to 347.2 nm) by focusing it inside a crystalline quartz sample. After that, subsequent nonlinear phenomena were reported at a tremendously rapid rate. These include sum frequency generation [4, 5], difference frequency generation [6], parametric amplification and oscillation [7, 8], multi-photon absorption [9], self-focusing[10], stimulated scattering [11], etc.

In the meantime, J. A. Armstrong and N. Bloembergen, et al. theoretically investigated some essential issues in nonlinear optics and presented the explicit analytical solutions to three and four coupled wave nonlinear equations. They proposed for the first time that the phase matching condition could be fulfilled by periodically changing the sign of nonlinear susceptibility. This technique, now known as quasi-phase matching (QPM) [12], has become a universal solution to the problem of phase mismatch.

Subsequently Kleinman published a paper discussing the physical mechanisms of nonlinear dielectric polarization in optical media [13]. He systematically studied the notation used to describe nonlinear properties of crystals. Previously used 18 independent components of nonlinear susceptibility were reduced to at most 10 nonlinear coefficients which greatly simplified calculations involving nonlinear susceptibility tensor. Midwinter and Warner then comprehensively investigated the effect of the symmetry properties of the second-order susceptibility tensor on the strength of the phase matched output signal at particular azimuthal angles for all non-centrosymmetric uniaxial crystals [14]. They also tabulated the second-order susceptibility tensor for each of the uniaxial crystals. Since then the studies of nonlinear optics progressed rapidly and expanded into a new domain with the help of tunable lasers and ultra-short pulsed lasers. Applications of nonlinear optics have become increasingly sophisticated.

The goal of this chapter is to review the basic principles of nonlinear optics in quadratic media. Section 1. 1 is a brief mathematical derivation of phase matching condition in nonlinear frequency conversion. We will derive the nonlinear wave equations from Maxwell's equations. Then by considering SHG in a uniform and isotropic nonlinear medium, we will obtain the phase matching condition in section 1. 2. Section 1. 3 introduces mainly two approaches to solve phase mismatch, namely birefringent phase matching and QPM. Section 1. 4 briefly introduces noncollinear second harmonic diffractions in one dimensional quadratic nonlinear media. Section 1. 5 explains the motivation for the investigations presented in this work and arrangement of the following chapters within this dissertation.

1.2 Nonlinear wave equation

One of the key point of nonlinear optics is to describe the propagation of electromagnetic waves through nonlinear media. The nonlinear wave equation describes the evolution of amplitude of light beams propagating in a nonlinear medium. It is the main tool required to conduct theoretical analysis and numerical studies of nonlinear light-matter interactions. We will derive the nonlinear wave equations from Maxwell's equations (in international

system of units), which describe the propagation of electromagnetic fields in medium:

$$\nabla \times \boldsymbol{E} = -\frac{\partial \boldsymbol{B}}{\partial t}, \qquad (1.\ 1.\ a) \qquad\qquad \nabla \bullet \boldsymbol{D} = \rho, \qquad (1.\ 1.\ b)$$

$$\nabla \times \boldsymbol{H} = \boldsymbol{J} + \frac{\partial \boldsymbol{D}}{\partial t}, \quad (1.\ 1.\ c) \qquad\qquad \nabla \bullet \boldsymbol{B} = 0, \qquad (1.\ 1.\ d)$$

where $\boldsymbol{E}$ and $\boldsymbol{H}$ are electric and magnetic field vectors respectively, $\boldsymbol{D}$ is a dielectric displacement, $\boldsymbol{B}$ is magnetic induction, $\boldsymbol{J}$ is electric current density and ρ is electric charge density. We also need the constitutive relations, also known as material equations, which describe the effect of electromagnetic fields on a material:

$$\boldsymbol{B} = \mu_0 \boldsymbol{H} + \boldsymbol{M}, \qquad (1.\ 2.\ a)$$

$$\boldsymbol{D} = \epsilon_0 \boldsymbol{E} + \boldsymbol{P}, \qquad (1.\ 2.\ b)$$

where ϵ_0 and μ_0 are the permittivity and permeability of the vacuum. In this thesis we consider charge and current free nonmagnetic medium, so ρ = 0, $\boldsymbol{J}$ = 0 and $\boldsymbol{M}$ = 0. First, we substitute magnetic induction $\boldsymbol{B}$ and electric displacement $\boldsymbol{D}$ in Eq. (1. 1. a) and Eq. (1. 1. c) using Eqs. (1. 2). Next, we take the curl of Eq. (1. 1. a) and utilize Eq. (1. 1. c) to eliminate $\boldsymbol{H}$. We obtain

$$\nabla \times \nabla \times \boldsymbol{E} + \frac{1}{c^2}\frac{\partial^2 \boldsymbol{E}}{\partial t^2} = -\frac{1}{\epsilon_0 c^2}\frac{\partial^2 \boldsymbol{P}}{\partial t^2}, \qquad (1.\ 3)$$

By replacing μ_0 with $1/\epsilon_0 c^2$ and using the relation $\nabla \times \nabla \times = \nabla(\nabla \bullet) - \nabla^2$, we obtain the most general nonlinear wave equation:

$$\nabla(\nabla \bullet \boldsymbol{E}) - \nabla^2 \boldsymbol{E} + \frac{1}{c^2}\frac{\partial^2 \boldsymbol{E}}{\partial t^2} = -\frac{1}{\epsilon_0 c^2}\frac{\partial^2 \boldsymbol{P}}{\partial t^2}, \qquad (1.\ 4)$$

The polarization $\boldsymbol{P}$ is induced by the electric field $\boldsymbol{E}$ of the propagating light in the medium. In the case of linear interaction, as shown in Figure 1. 1(a), the polarization $\boldsymbol{P}$ is proportional to the electric field $\boldsymbol{E}$: $\boldsymbol{P} = \epsilon_0 \chi^{(1)} \boldsymbol{E}$, where $\chi^{(1)}$ is the linear electric susceptibility of the medium. If the optical

electric field is strong enough, the polarization $\boldsymbol{P}$ becomes nonlinear and can be expressed as:

$$\begin{aligned}\boldsymbol{P} &= \epsilon_0\chi^{(1)}\boldsymbol{E}+\epsilon_0\chi^{(2)}\boldsymbol{E}^2+\epsilon_0\chi^{(3)}\boldsymbol{E}^3+\cdots=\epsilon_0\boldsymbol{E}(\chi^{(1)}+\chi^{(2)}\boldsymbol{E}+\chi^{(3)}\boldsymbol{E}^2+\cdots)\\ &= \boldsymbol{P}^{(1)}+\boldsymbol{P}^{(2)}+\boldsymbol{P}^{(3)}+\cdots=\boldsymbol{P}^{L}+\boldsymbol{P}^{NL},\end{aligned} \tag{1.5}$$

where $\chi^{(1)}$, $\chi^{(2)}$, $\cdots$, $\chi^{(n)}$ are the linear, second, third and n-th order susceptibility, $\boldsymbol{P}^L = \boldsymbol{P}^{(1)}$ is linear polarization and $\boldsymbol{P}^{NL}=\boldsymbol{P}^{(1)}+\boldsymbol{P}^{(2)}+\boldsymbol{P}^{(3)}+\cdots$ represents all the nonlinear terms.

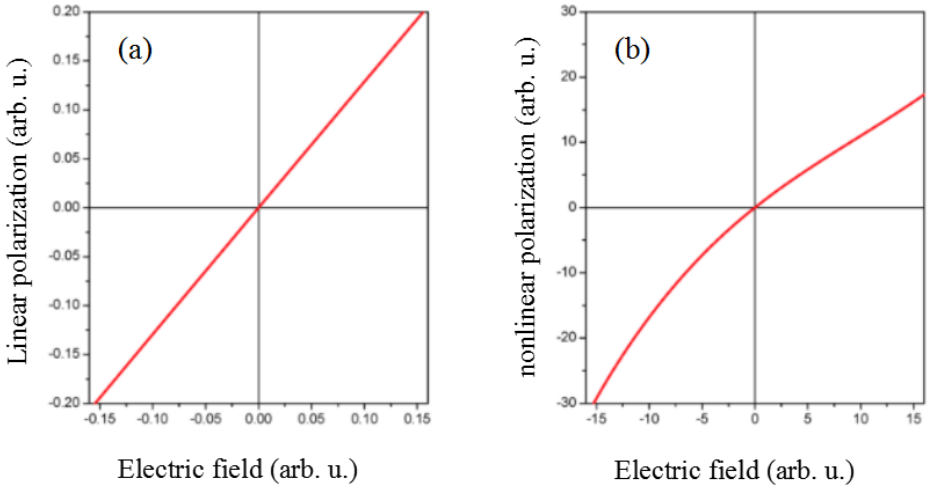

Figure 1.1 Typical (a) linear and (b) nonlinear polarization versus electric field curves.

We substitute $\epsilon_0\chi^{(1)}\boldsymbol{E}+\boldsymbol{P}^{NL}$ for $\boldsymbol{P}$ and obtain:

$$\nabla(\nabla\cdot\boldsymbol{E})-\nabla^2\boldsymbol{E}+\frac{1}{c^2}\frac{\partial^2}{\partial t^2}(\epsilon^{(1)}\cdot\boldsymbol{E})=-\frac{1}{\epsilon_0 c^2}\frac{\partial^2\boldsymbol{P}^{NL}}{\partial t^2}, \tag{1.6}$$

where $\epsilon^{(1)}=1+\chi^{(1)}$ is a relative dielectric permittivity tensor. Since we consider dispersive media, the relative dielectric permittivity is a function of the frequency of the propagating light, $\epsilon^{(1)}=\epsilon^{(1)}(\omega)$. The time dependent electric field and the nonlinear polarization can be expressed as:

$$\boldsymbol{E}(\boldsymbol{r},t)=\sum_n \boldsymbol{E}_n(\boldsymbol{r})e^{-i\omega_n t}+c.c., \tag{1.7}$$

$$\boldsymbol{P}^{NL}(\boldsymbol{r},t)=\sum_n \boldsymbol{P}_n^{NL}(\boldsymbol{r})e^{-i\omega_n t}+c.c., \tag{1.8}$$

If we insert the electric field and polarization from Eq. (1. 7) and Eq. (1. 8) into Eq. (1. 6), we obtain:

$$\nabla(\nabla \bullet \boldsymbol{E}_{\mathrm{n}}(\boldsymbol{r})) - \nabla^2 \boldsymbol{E}_{\mathrm{n}}(\boldsymbol{r}) - \frac{\omega_{\mathrm{n}}^2}{c^2}\epsilon^{(1)}(\omega_n) \bullet \boldsymbol{E}_{\mathrm{n}}(\boldsymbol{r}) = \frac{\omega_{\mathrm{n}}^2}{\epsilon_0 c^2}\boldsymbol{P}_n^{NL}(\boldsymbol{r}), \qquad (1.\ 9)$$

In typical situation the term $\nabla(\nabla \bullet \boldsymbol{E}_{\mathrm{n}}(\boldsymbol{r}))$ is much smaller than $\nabla^2 \boldsymbol{E}_{\mathrm{n}}(\boldsymbol{r})$. In particular, for a plane wave, $\nabla(\nabla \bullet \boldsymbol{E}_{\mathrm{n}}(\boldsymbol{r}))=0$. Neglecting this term in Eq.(1.9), we obtain:

$$\nabla^2 \boldsymbol{E}_{\mathrm{n}}(\boldsymbol{r}) + \frac{\omega_{\mathrm{n}}^2}{c^2}\epsilon^{(1)}(\omega_n) \bullet \boldsymbol{E}_{\mathrm{n}}(\boldsymbol{r}) = -\frac{\omega_{\mathrm{n}}^2}{\epsilon_0 c^2}\boldsymbol{P}_n^{NL}(\boldsymbol{r}), \qquad (1.\ 10)$$

In real applications, we can choose the crystal orientation in such a way that the above vectorial equation can be simplifies to a scalar equation:

$$\nabla^2 \boldsymbol{E}_{\mathrm{n}}(\boldsymbol{r}) + k_{\mathrm{n}}^2 \boldsymbol{E}_{\mathrm{n}}(\boldsymbol{r}) = -\frac{\omega_{\mathrm{n}}^2}{\epsilon_0 c^2}\boldsymbol{P}_n^{NL}(\boldsymbol{r}), \qquad (1.\ 11)$$

where we replaced $\frac{\omega_{\mathrm{n}}^2}{c^2}\epsilon^{(1)}(\omega_n)$ by k_{n}^2. The Eq.(1.11) constitutes the time independent nonlinear wave equation.

1.3 Phase matching condition

Efficient nonlinear interaction depends sensitively on the relative phases between interacting beams. Different optical frequencies propagate with different phase velocities in a nonlinear medium because the refractive index is wavelength dependent. Collinear second harmonic generation in a uniform and isotropic nonlinear medium is the most prototypical and simplest nonlinear optical process. In this section, the phase matching condition in collinear second harmonic generation will be deduced from time independent nonlinear wave equation.

A fundamental plane wave with complex amplitude $\boldsymbol{E}_1$ propagating in z direction of a nonlinear medium, will generate the second harmonic wave $\boldsymbol{E}_2$. The electric fields of both waves can be expressed as:

$$\boldsymbol{E}_1 = \mathrm{A}_1(z)e^{-ik_1 z} \quad , \qquad (1.\ 12)$$

$$\boldsymbol{E}_2 = \mathrm{A}_2(z)e^{-ik_2 z} \quad , \qquad (1.\ 13)$$

where $k_1 = 2\pi n_1 / \lambda_1$ and $k_2 = 2\pi n_2 / \lambda_2$ are the wave vectors of the fundamental beam (FB) and second harmonic (SH), n_1, λ_1, and n_2, λ_2 are refractive indices and wavelengths of FB and SH, respectively. By applying Eq. (1. 12) and Eq. (1. 13) in Eq. (1. 11), we obtain:

$$\frac{d^2 \boldsymbol{E}_1(\mathrm{z})}{dz^2} + k_1^2 \boldsymbol{E}_1(z) = -\frac{\omega_1^2}{\epsilon_0 c^2} \boldsymbol{P}_1^{NL}(z), \qquad (1.\ 14)$$

$$\frac{d^2 \boldsymbol{E}_2(\mathrm{z})}{dz^2} + k_2^2 \boldsymbol{E}_2(z) = -\frac{\omega_2^2}{\epsilon_0 c^2} \boldsymbol{P}_2^{NL}(z), \qquad (1.\ 15)$$

According to Kleinman [13], the nonlinear polarization terms in the right hand side of Eq.(1.14) and (1.15) can be expressed as:

$$\boldsymbol{P}_1^{NL}(\mathrm{z}) = 4\epsilon_0 d_{\mathrm{ij}} \boldsymbol{E}_2(\mathrm{z}) \boldsymbol{E}_1^*(\mathrm{z}), \qquad (1.\ 16)$$

$$\boldsymbol{P}_2^{NL}(z) = 2\epsilon_0 d_{\mathrm{ii}} \boldsymbol{E}_1^2(\mathrm{z}), \qquad (1.\ 17)$$

The nonlinear coefficient d_{ij} represents elements of the quadratic susceptibility tensor $\chi^{(2)}$ by considering the so called Kleinman symmetry conditions. The nonlinear coefficient d_{ij} is a 3×6 matrix whose non-zero components depend on the point group of the nonlinear medium. The following two examples depict nonlinear coefficient d_{ij} for lithium niobate ($LiNbO_3$, 3m point group) and calcium barium niobate (CBN, 4mm point group).

$$d_{LiNbO_3} = \begin{pmatrix} 0 & 0 & 0 & 0 & d_{31} & -d_{22} \\ -d_{22} & d_{22} & 0 & d_{31} & 0 & 0 \\ d_{31} & d_{31} & d_{33} & 0 & 0 & 0 \end{pmatrix}, \qquad (1.\ 18)$$

$$d_{\mathrm{CBN}} = \begin{pmatrix} 0 & 0 & 0 & 0 & d_{15} & 0 \\ 0 & 0 & 0 & d_{15} & 0 & 0 \\ d_{31} & d_{31} & d_{33} & 0 & 0 & 0 \end{pmatrix}, \qquad (1.\ 19)$$

If we insert the electric fields and nonlinear polarizations from Eqs. (1. 12) and (1. 13) into Eqs. (1. 14) and (1. 15), and use the so called slowly varying envelope approximation (SVEA), which means $\left|\frac{d^2\boldsymbol{A}_n}{dz^2}\right| \ll \left|2ik_n\frac{d\boldsymbol{A}_n}{dz}\right|$, we obtain

$$\frac{d\boldsymbol{A}_1(z)}{dz} = -\frac{2id_{ij}w_1^2}{c^2k_1}\boldsymbol{A}_2(z)\boldsymbol{A}_1^*(z)e^{-i\Delta kz}, \qquad (1.\ 20)$$

$$\frac{d\boldsymbol{A}_2(z)}{dz} = -\frac{id_{ij}w_2^2}{c^2k_2}\boldsymbol{A}_1^2(z)e^{i\Delta kz}, \qquad (1.\ 21)$$

where Δk is the so-called phase mismatch parameter, which represents the dispersion induced difference in phase velocities of the FB and SH, and $\Delta k = k_2 - 2k_1$.

We can further simplify Eq. (1. 21) by using the so called undepleted pump approximation, which assumes that the amplitude of the FB does not change with propagation distance when the conversion efficiency is very low. In this case, $\boldsymbol{A}_1(z)$ is constant, and the above coupled wave equations reduce to one equation

$$\frac{d\boldsymbol{A}_2(z)}{dz} = -\frac{id_{ij}w_2^2}{c^2k_2}\boldsymbol{A}_1^2e^{i\Delta kz}, \qquad (1.\ 22)$$

The solution to Eq. (1. 22) is

$$\boldsymbol{A}_2(z) = -\frac{iA_1^2d_{ij}w_2^2}{c^2k_2}z\,\mathrm{sinc}\left(\frac{\Delta kz}{2}\right)e^{\frac{i\Delta kz}{2}}, \qquad (1.\ 23)$$

where the sinc function $\mathrm{sinc}(x) = \sin(x)/x$. Therefore, the intensity of emitted second harmonic $I_2 = 2n_2\epsilon_0c|A_2|^2$ can be expressed as

$$I_2(z) = \frac{2d_{ij}^2I_1^2\omega_1^2}{c^3n_1^2n_2\epsilon_0}z^2\mathrm{sinc}^2\left(\frac{\Delta kz}{2}\right). \qquad (1.\ 24)$$

Equation (1. 24) is a well-known equation which describes the intensity variation of SH when conversion efficiency is very small. Although it is obtained for plane waves in a specific case of collinear interaction using SVEA and undepleted pump approximation, it reflects some important characteristics for SHG. First of all, the intensity of SH is proportional to the square of the intensity of the fundamental beam. Second, the SH intensity depends strongly on the phase mismatch parameter Δk.

Phase mismatch between the interacting waves propagating in nonlinear materials is a major problem in early research of nonlinear optics [12, 15]. The essential reason for phase mismatch is that normally all nonlinear materials are dispersive. In the simplest case of SHG, the FB propagates with wave vector $k_1 = 2\pi n_1 / \lambda_1$ while the SH propagates with wave vector $k_2 = 2\pi n_2 / \lambda_2$. We can see from Eq. (1. 24) that the strongest SHG could be achieved when Δk is zero, which means exact phase matching. In this case, we obtain Eq. (1. 25) and we can see that the intensity of SH increases quadratically with propagation distance.

$$I_2(z) = \frac{2I_1^2\omega_1^2}{c^3 n_1^2 n_2 \epsilon_0} d_{ij}^2 z^2, \qquad (1.\ 25)$$

In order to obtain exact phase matching, both energy conservation and momentum conservation are required, which can be expressed as

$$\omega_1 + \omega_1 = \omega_2, \qquad (1.\ 26)$$

$$n_1\omega_1 + n_1\omega_1 = n_2\omega_2, \qquad (1.\ 27)$$

We can deduce from the above two equations that this requires $n_1 = n_2$. However, because almost all the materials are dispersive, the refractive indices are frequency-dependent. It is difficult to fulfill $n_1(\omega_1) = n_2(\omega_2)$ in real materials what results in nonzero phase mismatch

$$\Delta k = k_2 - 2k_1 = 4\pi\left(n_2(\omega_2) - n_1(\omega_1)\right)/\lambda_1, \qquad (1.\ 28)$$

Equation (1. 25) can be written as $I_2(z) = RI_1^2 z^2 \left(\frac{\sin(\Delta kz/2)}{\Delta kz/2} \right)^2$, where $R = \frac{2d_{ij}^2 \omega_1^2}{c^3 n_1^2 n_2 \epsilon_0}$. From the mathematical point of view, this is a periodic function with a period of $L_c = \pi/\Delta k$, as shown in Figure 1. 2. The parameter L_c, defining the length of the nonlinear medium providing the maximum SHG efficiency, is referred to as the coherence length and will be discussed in more details in section 1.3. From the physical point of view, the relative phase between FB and SH determines the direction of the energy flow between the interacting waves. Therefore, non-zero phase mismatch results in periodic alternation of the direction of energy flow between both waves. Initially the energy flows from fundamental to second harmonic and then back, after the relative phase between both waves reaches π.

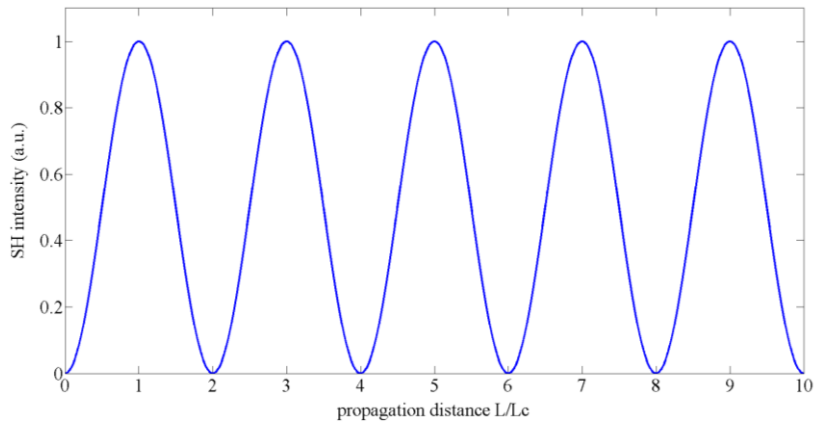

Figure 1.2 Periodic oscillation of phase mismatched SHG along the propagation direction.

P. D. Marker reported the experimental observation of SH intensity oscillation with propagation distance in quartz [16], as shown in Figure 1. 3. In order to change the propagation distance, a quartz platelet was inclined with respect to the direction of ruby laser beam by rotating about its *z* axis.

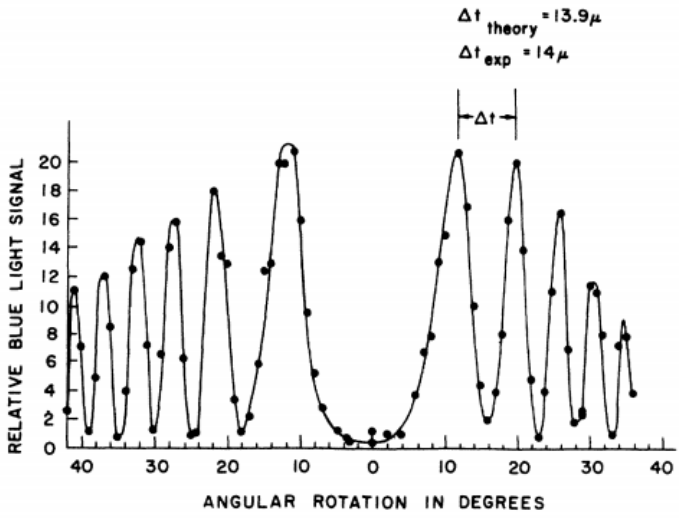

Figure 1.3 Dependence of phase mismatched SHG as a function of propagation distance in a thick quartz platelet [16].

Figure 1. 4 shows a typical curve for SH intensity as a function of Δk. We can see that a small deviation of Δk would lead to a dramatic decrease of SH intensity. In real applications, the phase mismatch in most nonlinear crystals is an order of 1 μm^{-1} making efficient SHG almost impossible to achieve.

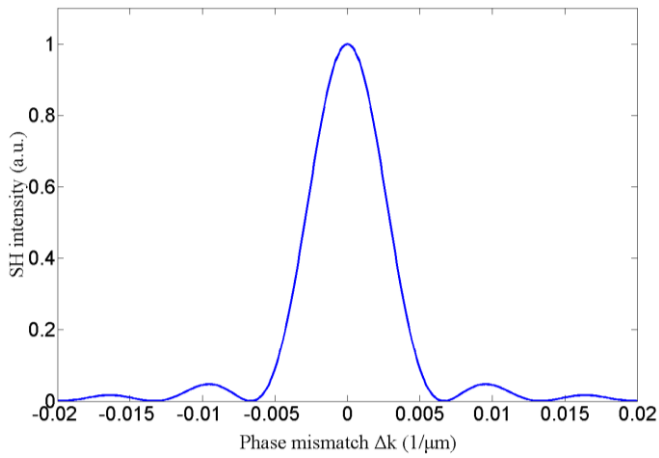

Figure 1.4 Dependence of phase mismatched SH intensity as a function of propagation distance in a thick quartz platelet.

Numerous strategies have been developed to solve the phase-matching problem. For example, using waveguide dispersion to compensate for the phase mismatch caused by the material dispersion in waveguide regimes [17]. Another example is harmonic generation in the gas phase, which can be phase-matched by using an optimization of the content of the gas mixture

[18]. However, the most practically significant solutions are birefringent phase matching (BPM) [19, 20] and quasi phase matching (QPM) in nonlinear photonics crystals (NPCs) [12]. In the following section, we will mainly introduce BPM and QPM. The first one eliminates the phase mismatch by adjusting the phase velocities of the interacting waves. The second one provides a net compensation for the phase mismatch by modulating nonlinearity of the material. The advantages and disadvantages of these two techniques are discussed and compared.

1. 4 Methods of phase matching

1.4.1 Birefringent phase matching

Giordmaine and Maker, et al. independently reported that the phase mismatch of FB and SH in potassium dihydrogen phosphate (KDP) could be balanced out by carefully choosing the polarization of waves and propagation direction [8, 16]. This phase matching resulted in a 300-fold increase of SH intensity. Midwinter, et al. extended this technique, now known as birefringent phase matching (BPM), or index phase matching, to a more general case of three-wave mixing [14].

The crystal they used in the experiment, KDP, is a typical birefringent crystal. The refractive index of a birefringent crystal depends on the polarization and propagation direction of light. Usually crystal with non-cubic crystal structure is birefringent and one or two its special directions govern the optical anisotropy whereas all directions perpendicular to it (or at a given angle to it) are optically equivalent. Therefore, rotating the material around this axis does not change its optical behavior. This special direction is known as the optic axis of the crystal. Depending on the number of optic axes in a birefringent crystal, the latter is either a uniaxial or a biaxial. Light whose polarization is perpendicular to the optic axis is governed by the ordinary refractive index n_o, while that whose polarization is in the direction of the optic axis sees an extraordinary optical index n_e.

Here we take $LiNbO_3$ as an example to illustrate the theory of BPM. $LiNbO_3$ is a negative uniaxial crystal which means that n_e is smaller than n_o at the same wavelength ($n_e < n_o$). Most of the nonlinear media have normal dispersion, which means the refractive index of FB is smaller than the refractive index of SH, $n(\omega) < n(2\omega)$. In order to fulfill the phase matching condition, the SH should be chosen as extraordinary wave, while for the FB we have two possibilities. In the first case, known as type-I phase matching, both FB photons have the same polarization (ordinary light). In the second case, known as type-II phase matching, two FB photons are mutually orthogonally polarized, i.e. one is ordinary and the second one extraordinary.

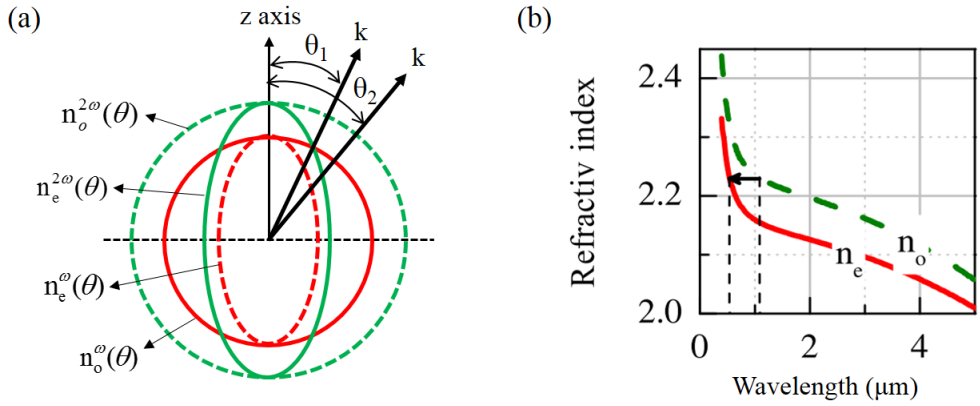

Figure 1.5 (a) Birefringent phase matching diagram in $LiNbO_3$. (b) Refractive index curves for the ordinarily and extraordinarily polarized beam in $LiNbO_3$ [17].

Figure 1. 5 (a) shows the phase matching diagram for $LiNbO_3$. The refractive indices of ordinary and extraordinary light are indicated by a circle and an ellipse. We can see that at a certain propagation angle θ_1, the refractive index of an ordinary FB equals to the refractive index of an extraordinary SH. We obtain the type-I phase matching condition.

$$n_o(\omega_1) = n_e(2\omega_1), \qquad (1.29)$$

At this propagation direction in the crystal, the differently polarized FB and SH components have the same phase velocities so that the phase matching condition is satisfied. Figure 1. 5 (b) shows the refractive index curves for $LiNbO_3$. We can see that if the FB is ordinarily polarized at a wavelength of 1.078 μm and the SH is extraordinarily polarized at 0.539 μm,

they will experience the same refractive index and consequently the phase matching condition will be fulfilled.

In the case of type-II phase matching, in order to eliminate the phase mismatch, the following equation should be fulfilled

$$k_{2e} = k_{1o} + k_{1e}, \tag{1.30}$$

where k_{1o} , k_{1e} and k_{2e} represent the wave vector of the ordinary FB, extraordinary FB and extraordinary SH. We can deduce from Eq. (1. 30) that

$$n_{2e} = (n_{1o} + n_{1e}) / 2, \tag{1.31}$$

where n_{1o}, n_{1e} and n_{2e} represent the refractive indices of the ordinary FB, extraordinary FB and extraordinary SH, respectively. The propagation angle of type-II phase matching is indicated as θ_2 in Figure 1. 5 (a). The polarizations of interacting beams and the orientation of the crystal are rigorously chosen to fulfill the phase-matching condition. This phase-matching technique is called angle tuning. Because it is very sensitive dependent on the angle of propagation, angle tuning is also known as critical phase matching.

Since refractive indices depend on temperature, one can obtain exact phase matching in a small range of FB wavelengths by tuning the temperature of the crystal [20]. Simultaneous control of both temperature and propagation direction makes it possible to fulfill exact phase matching condition in a continuous wavelength ranges of incident beams, ensuring very high conversion efficiency. Therefore, BPM technique is widely used in generating tunable coherent light sources, like optical parametric oscillators (OPO) and optical parametric amplifiers (OPA).

Despite the wide application of BPM, this technique suffers from several drawbacks. One undesirable effect, especially in angle tuning, is that the optical frequencies involved do not propagate collinearly with each other. This is due to the fact that the extraordinary wave propagating through a birefringent crystal possesses a Poynting vector that is not parallel to the propagation vector. As a result, ordinary and extraordinary beams with

parallel propagation vectors quickly diverge from one another as they propagate through the crystal. This so-called walk-off effect limits the effective interaction length of the two waves and decreases the efficiency of any nonlinear mixing process involving such waves [21]. Although this problem could be solved by temperature tuning, the other two connatural disadvantages of BPM make it necessary to develop alternative phase matching techniques. First of all, due to the restrictive angular, temperature and wavelength acceptances, it is impossible to fulfill phase matching condition in arbitrary crystals and for arbitrary wavelengths. Some materials (like gallium arsenide, GaAs) may possess no birefringence, or may have insufficient birefringence to compensate for the dispersion over the desired wavelength range. For example, in $LiNbO_3$ blue and ultra-violet (UV) spectral range are inaccessible for BPM. Because of the vicinity of absorption edge, the dispersion curves change rapidly, and even by angle and temperature tuning, the phase matching condition could not be satisfied. The second disadvantage is that the BPM technique is limited to off-diagonal nonlinear tensor elements. In many crystals, like $LiNbO_3$, lithium tantalate ($LiTaO_3$) and potassium titanyl phosphate ($KTiOPO_4$ or KTP), the off-diagonal components of nonlinear tensor are modest, typically below 5 pm/V (see table 1.1), resulting in low conversion efficiency.

Table 1.1 Nonzero nonlinear tensor components of $LiNbO_3$, $LiTaO_3$ and KTP [22].

$LiNbO_3$ (pm/V)	$LiTaO_3$ (pm/V)	KTP (pm/V)
		$d_{15} = 2.7$
$d_{22} = 2.7$	$d_{22} = 2.0$	$d_{24} = 2.7$
$d_{31} = 4.5$	$d_{31} = 1.0$	$d_{31} = 2.7$
$d_{33} \approx 27\text{-}34$	$d_{33} = 21$	$d_{32} = 4.35$
		$d_{33} = 16.9$

1.4.2 Quasi-phase matching

Quasi-phase matching (QPM) was a technique first proposed by Armstrong and Bloembergen in 1962 in their pioneering paper "Interactions between Light Waves in a Nonlinear Dielectric" [12]. As we discussed above, the SH intensity in a phase mismatched condition is a periodic function with a period of coherence length $L_c=\pi/\Delta k$. The curve A in Figure 1. 6 shows the SH intensity as a function of propagation distance in a phase mismatched condition. In the first coherence length, the relative phase between FB and SH is smaller than π, therefore, the energy flows from FB to SH. However, in the second coherence length, the relative phase exceeds π, the energy is transferred back from SH to FB. As a result, the SH intensity oscillates with propagation distance. The basic idea of QPM is to periodically correct the relative phase every other coherence length. Armstrong and Bloembergen suggested many different ideas to obtain this phase correction [12]. They include, for instance, periodic refractive index modulations (gratings) [23, 24]. However, this method generally results in relatively low conversion efficiency. Another more efficient and commonly used QPM technique is based on changing the sign of second order susceptibility $\chi^{(2)}$, which is the most commonly used QPM technique nowadays. Changing the sign of nonlinear susceptibility means inducing a π phase shift between FB and SH. Periodic modulation of the nonlinear susceptibility ensures the relative phase between interacting waves is always less than π, therefore, the energy keeps flowing from FB to SH. The SH intensity in a QPM structure is illustrated as curve B in Figure 1. 6.

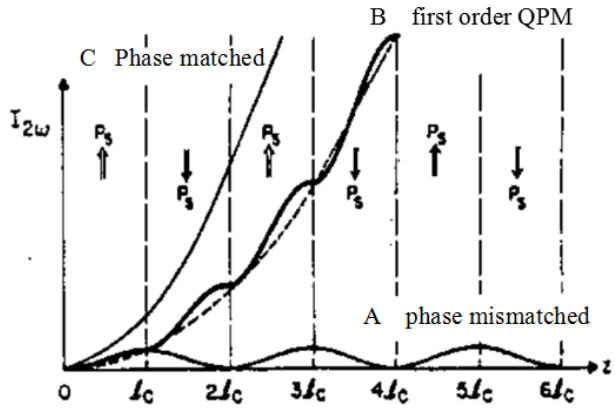

Figure 1.6 Intensity of SHG as a function of propagation distance in phase mismatched (curve A), QPM (curve B) and the exact phase matched (curve C) condition [12].

Periodic modulation of the nonlinear susceptibility can be realized not only by changing the sign of nonlinearity, but also by changing the value of the nonlinear coefficient. Chapter 2 will give more detailed introduction to different ways to fabricate QPM structures.

The SH intensity generated by a one dimensional QPM structure is mathematically described in the following part of this section. This will help us to better understand the mechanism of QPM and its advantages over BPM technique. The nonlinearity of a one-dimensional QPM structure with a period of Λ can be expressed as Fourier series

$$d(z) = \sum_{l=-\infty}^{\infty} D_l e^{-il\frac{2\pi}{\Lambda}z} = \sum_{l=-\infty}^{\infty} D_l e^{-iG_l z}, \qquad (1.\ 32)$$

where D_l is the Fourier coefficient of the l-th spatial frequency component and $G_l = lk_0 = 2l\pi/\Lambda$ is the l-th multiple of the fundamental spatial frequency. Replacing d_{ij} in Eq. (1. 21) with d(z) and assuming undepleted pump approximation $A_1(z) = A_1$, we obtain

$$\frac{dA_2(z)}{dz} = -\frac{i\omega_2^2}{c^2 k_2} A_1^2 \sum_{l=-\infty}^{\infty} D_l e^{-i(G_l - \Delta k)z}, \qquad (1.\ 33)$$

This equation can be solved by integration of the right-hand side over z. Considering that only the terms of the sum over l, denoted as m, contribute significantly to A_2, we obtain

$$A_2(z) \simeq -\frac{iA_1^2\omega_2^2}{c^2k_2} zD_m \operatorname{sinc}\left(\frac{(G_m-\Delta k)z}{2}\right) e^{i\frac{(G_m-\Delta k)z}{2}}, \qquad (1.\ 34)$$

and the intensity of SH

$$I_2(z) = \frac{2|D_m|^2 I_1^2\omega_1^2}{c^3 n_1^2 n_2 \epsilon_0} z^2 \operatorname{sinc}^2\left(\frac{(G_m-\Delta k)z}{2}\right), \qquad (1.\ 35)$$

By contrast, equation 1.2. describes the SH intensity in a phase mismatched condition in homogenous crystal as

$$I_2(z) = \frac{2d_{ij}^2 I_1^2\omega_1^2}{c^3 n_1^2 n_2 \epsilon_0} z^2 \operatorname{sinc}^2\left(\frac{\Delta kz}{2}\right), \qquad (1.\ 24)$$

We can see that the original phase mismatch parameter Δk is replaced by the term ($G_\mathrm{m} - \Delta k$), and nonlinearity d_ij by Fourier coefficient D_m. The quasi phase match condition for efficient SHG is

$$\Delta k_{\mathrm{QPM}} = \Delta k - G_m = 0, \qquad (1.\ 36)$$

where Δk_{QPM} is the quasi phase match parameter and vector $G_m = 2\pi m / \Lambda$ is reciprocal lattice vector (RLV) of the QPM structure. RLV is provided by the periodicity of the structure to ensure momentum conservation $2k_1 + G_m = k_2$. Therefore, quasi phase matching condition can be written as

$$\Delta k_{\mathrm{QPM}} = k_2 - 2k_1 - G_m = 0, \qquad (1.\ 37)$$

And the SH intensity becomes

$$I_2(z) = \frac{2|D_m|^2 I_1^2\omega_1^2}{c^3 n_1^2 n_2 \epsilon 0} z^2 \operatorname{sin} c^2\left(\frac{\Delta k_{\mathrm{QPM}} z}{2}\right), \qquad (1.\ 38)$$

The nonlinearity of the QPM structure, denoted by $d(z)$, can be expressed as a square wave function

$$d(z) = d_{\mathrm{eff}} \operatorname{sign}\left[\cos(2\pi z / \Lambda)\right], \qquad (1.\ 39)$$

where d_{eff} denotes the nonlinear coefficient for the propagation direction and polarization, sign (x) is a sign function and denotes the sign of x, Λ is the

period of the QPM structure. The spatial variation of d(z) can be described in terms of a Fourier series

$$d(z) = d_{\text{eff}} \sum_{m=-\infty}^{m=\infty} F_m e^{-iG_m z}, \qquad (1.\ 40)$$

F_{m} is the Fourier coefficient given by

$$F_m = \frac{2}{m\pi} \sin(m\pi D), \qquad (1.41)$$

where $D = l_{\text{d}}/\Lambda$ is the duty cycle of the QPM structure, l_{d} is the length of the inverted domain and Λ the period of reversal. For the QPM interaction, the period of the structure can be given by

$$\Lambda = 2\pi m / \left(k_2 - 2k_1\right), \qquad (1.\ 42)$$

The SH intensity strongly depends on the modulation of nonlinearity d(z) via the Fourier coefficients D_{m}. In the case of a duty cycle of D = 50%, the strongest Fourier coefficient $D_{\text{m}} = d_{\text{ij}} \cdot 2/(m\pi)$ is achieved. Therefore, we obtain the SH intensity in a quasi-phase matched process

$$I_2(z) = \frac{2 d_{ij}^2 \omega_1^2 I_1^2}{c^3 n_1^2 n_2 \epsilon_0} \frac{4}{m^2 \pi^2} z^2, \qquad (1.\ 43)$$

Note that the tendency for $I_2(z)$ to decrease with increasing values of m, it is most desirable to achieve quasi-phase-matching with a first-order (m = 1) interaction. In this case, comparing the above formula with the SH intensity in BPM condition in Eq. (1. 25), we can see that the SH intensity in QPM condition is reduced by a factor of $4/(\pi^2)$. However, as we discussed in last part of section 1.3.1, the BPM technique is limited to off diagonal elements of the nonlinear tensor d_{ij} while QPM technique can utilize the strongest element. As a numerical example, the maximal component for congruent $LiNbO_3$ (CLN) in BPM is d_{31} = 4.5 pm/V, and the strongest nonlinear coefficient is d_{33} = 34.4 pm/V. If the first order QPM condition is fulfilled, then the effective nonlinearity will be $d_{\text{eff}} = d_{33} \cdot 2/\pi \approx 21.9$ pm/V, which means more than 4 times increase in SH intensity. Therefore, although there is a decrease factor $4/(\pi^2)$ in the formula, QPM technique can achieve higher SH intensity

comparing with BPM. The advantages of QPM also include the flexibility and versatility of this technique. In principle, it allows for efficient nonlinear interactions in at any frequencies in the transparency range of the material, including materials without birefringence and wavelength range that BPM is inaccessible. In addition, the beam walk-off effect can be avoided in a QPM process by forcing all interacting waves to propagate at 90° angle with respect to the optical axis of the crystal. Furthermore, the period of a QPM structure can be adjusted in order to obtain a desired phase-matching temperature. Operation at or near room temperature is therefore often possible without resorting to critical phase matching or noncollinear phase matching. This option is important for nonlinear interactions in waveguides, where noncollinear beams usually cannot be used.

1.5 Noncollinear second harmonic generation

In the above sections, we introduced collinear SHG in nonlinear media and obtained the phase matching conditions. Second harmonic generation with harmonics emitted at nonzero angles with respect to the FB, i.e. noncollinear SHGs, have also been demonstrated both theoretically and experimentally. Considering the simplest case when FB propagates perpendicularly to the periodic modulation of the nonlinear susceptibility, as shown in Figure 1. 7, second harmonic waves can be emitted in different directions. As the emission of harmonics resembles the standard diffraction from the periodic index modulation, this process is called nonlinear diffraction [25].

In order to generate efficient noncollinear SHs, the following vectorial quasi phase matching condition needs to be fulfilled

$$\boldsymbol{k}_2 = 2\boldsymbol{k}_1 + \boldsymbol{G}_m, \qquad (1.\ 44)$$

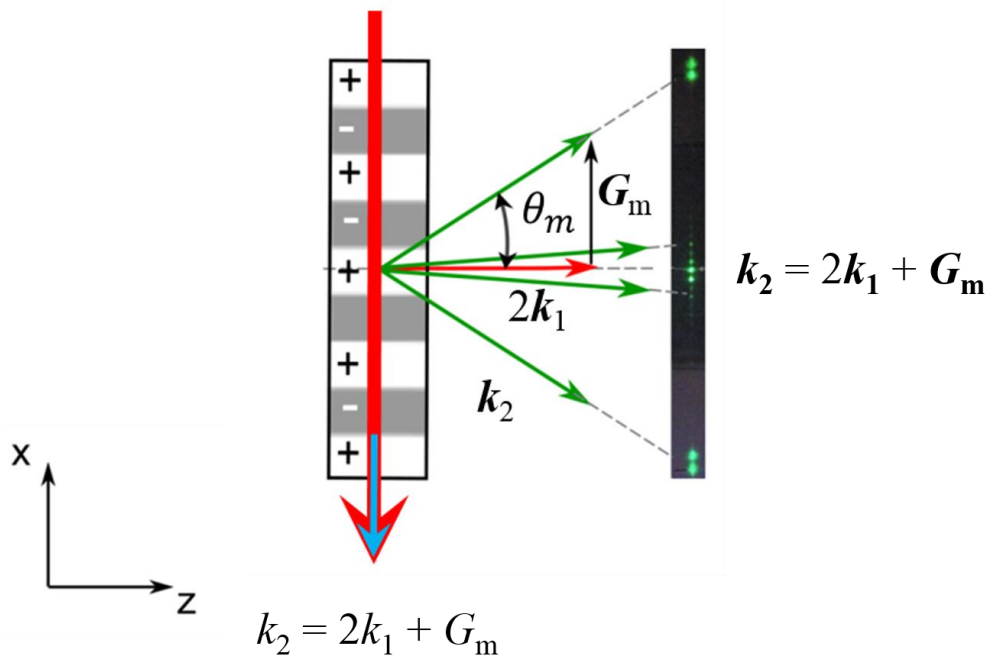

$$k_2 = 2k_1 + G_{\mathrm{m}}$$

Figure 1. 7 Collinear and noncollinear SHGs in a one dimensional nonlinear medium. The red arrows and green arrows indicate the wave vectors of the FB and SHGs. The green dots on the black background represent the far field of noncollinearly emitted second harmonic beams recorded by a CCD camera.

The quasi phase matching condition of nonlinear diffraction can be decomposed into the longitudinal component $k_2 \cos\theta_{\mathrm{c}} = 2k_1$, and the transverse component $k_2 \sin\theta_{\mathrm{m}} = G_m$.

It has been shown in Eq. (1. 38) that the efficient SH will be generated by satisfying only longitudinal phase matching condition. If this happens, the generated SH beam is called Cerenkov SH (CSH) [26-28]. This beam propagates at an angle defined as

$$\theta_{\mathrm{c}} = \arccos\left(\frac{2k_1}{k_2}\right), \qquad (1.\ 45)$$

On the other hand, when only the transverse phase matching condition is satisfied, a number of the SH beams is emitted at angles determined as

$$\theta_{\mathrm{m}} = \arcsin\left(\frac{G_m}{k_2}\right), \qquad (1.\ 46)$$

This SH emission is called the nonlinear Raman-Nath SH [29], in analogy with standard Raman-Nath diffraction in linear optics. Finally, when both transverse and longitudinal phase matching conditions are simultaneously satisfied the SH generation process is called nonlinear Bragg diffraction [30], again in analogy with the well known Bragg diffraction process in linear optics. The phase matching diagrams for nonlinear Bragg, Cerenkov and nonlinear Raman-Nath diffractions are shown in Figure 1. 8.

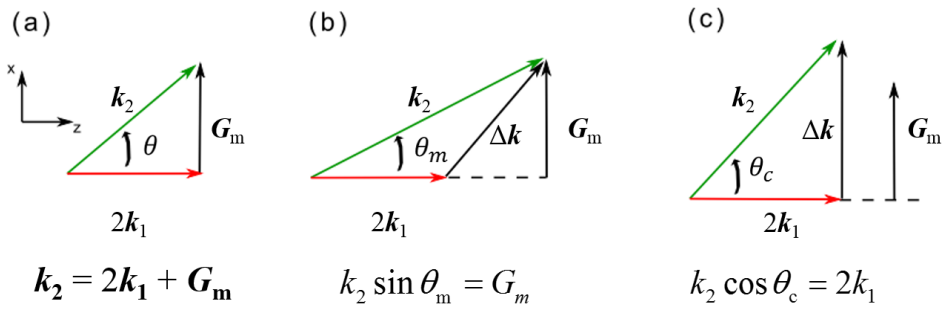

Figure 1. 8 Phase matching diagrams for (a) nonlinear Bragg diffraction, (b) nonlinear Raman-Nath diffraction and (c) nonlinear Cerenkov diffraction.

The CSHG was first theoretically predicted by Kleinman in 1962 and has been intensively investigated since its first experimental observation in 1968 [26-28]. It is of great interest in applications like all-optical signal processing, owing to its unique properties including high conversion efficiency and noncollinear emission. One can manipulate the emission properties of the CSHG by either changing the angle of the FB, or by introducing reciprocal lattice vectors along the propagation direction of the FB [31-33]. It has also been demonstrated that the intensity of the CSHG is sensitive to the wavelength, diameter and position of the incident FB [34-36]. Cerenkov harmonic irradiations have also been experimentally observed in other parametric processes, including difference frequency generation (DFG) and high order cascading processes [37, 38].

The nonlinear Raman-Nath diffractions, however, have been experimentally observed much later than the nonlinear Bragg diffraction, which is mainly due to the lack of high intensity laser sources. Nowadays, owing to the widely available femtosecond lasers, nonlinear Raman-Nath diffraction, including forward Raman-Nath SH, back scattering and the

cascaded Raman-Nath THG, have been readily observed and studied in nonlinear media with spatially modulated $\chi^{(2)}$ [39, 40].

1.6 Motivation and thesis arrangement

Quasi-phase matching allows for efficient nonlinear interactions by spatially modulating second order susceptibility, $\chi^{(2)}$, which brings appropriate reciprocal lattice vectors in phase matching diagrams and makes it a flexible and versatile method for applications like optical frequency conversion, beam shaping, quantum entanglement manipulation, etc. The development of QPM technique relies on advances in $\chi^{(2)}$ engineering approaches and inventions of novel $\chi^{(2)}$ structures in versatile material systems. This thesis explores further improvement of QPM technique in these three aspects. Specifically, four key topics were investigated, including an advanced technique for fabricating QPM structures, a new material for broadband optical frequency conversion, a custom cut periodically poled lithium niobate (PPLN) for cascading frequency conversion processes and nonlinear diffraction in orientation-patterned semiconductors. This thesis is organized as follows.

Chapter 2 provides an overview of QPM techniques, various QPM structures, as well as details on fabrication and visualization of $\chi^{(2)}$ spatially modulated structures. This chapter also reviews the milestones in literatures which have contributed to the developments of QPM.

Chapter 3 presents a detailed study on femtosecond laser poling technique and its application to QPM. Laser poling is a direct writing technique which can be easily employed for fabrication of various domain structures without the requirement for any high voltage facility, photolithography masks or ultra-clean environment. The parameters for optical poling using an infrared femtosecond laser were systematically investigated. As a demonstration of this all optical poling technique, a QPM structure was inscribed on a $LiNbO_3$ channel waveguide for frequency doubling of a 815 nm light.

Chapter 4 presents a study of application of calcium barium niobate ($Ca_xBa_{(1-x)}Nb_2O_6$, or CBN) crystals for broadband optical frequency

conversion. The commonly used SBN crystal suffers from a low Curie temperature, which limits its applications at high pump powers. $Ca_{0.28}Ba_{0.72}Nb_2O_6$ (CBN-28) crystal possesses a much higher phase transition temperature and therefore could be used as a broadband frequency converter even in elevated temperature. The spatial distribution and polarization properties of the emitted radiation were analyzed.

Chapter 5 presents a study on multistep cascading frequency conversion processes in a custom-cut PPLN. The traditional collinear QPM interaction and noncollinear Cerenkov frequency generations were combined in one single PPLN crystal. This approach offers the advantages of both interaction mechanisms to achieve higher conversion efficiency of high order harmonic generation via cascading processes. As a demonstration, enhanced fourth harmonic generation (FHG) was experimentally realized.

Chapter 6 presents a study on nonlinear diffraction in orientation patterned semiconductors. QPM in semiconductors offers a variety of nonlinear interactions, in particular, in infrared. However, in most cases only the collinear interaction along direction of the second order nonlinearity modulation has been considered. This chapter demonstrates noncollinear quadratic interactions in orientation patterned GaAs (OP-GaAs). It is also shows that the Cerenkov SHG can be used as an effective nondestructive technique for 3D visualization and diagnosis of domain structures inside semiconductors.

Chapter 7 concludes the thesis with a summary of the key innovations and suggestions for future investigations.

Chapter 2 Fundamental aspects of nonlinear optics in quadratic media

2.1 Introduction

In 1962, Armstrong and Bloembergen, et al. proposed a technique, now known as quasi-phase matching (QPM), to compensate the phase-mismatch between the interacting waves [12]. By periodically correcting the relative phase every other coherence length, the relative phase mismatch between interacting waves stays below π and the energy keeps flowing from the pump frequency to the signal frequency. Many ideas have been suggested to achieve this phase correction, and QPM based on changing the sign of second order susceptibility $\chi^{(2)}$, is the most commonly used. Figure 2.1 shows a typical one dimensional QPM structure, also known as optical superlattice. In the 1970s, people fabricated QPM structures by stacking thin plates of a nonlinear medium where adjacent layers were 180° rotated [41-44]. These structures suffered from multiple Fresnel reflections and transmission losses, resulting in very low conversion efficiency. Another disadvantage of this method is the difficulty in fabricating and stacking plates thinner than 100 μm due to the technical limitation of that time. This severely limited the output wavelength range of a QPM structure, making spectral ranges like visible and infrared impossible to reach.

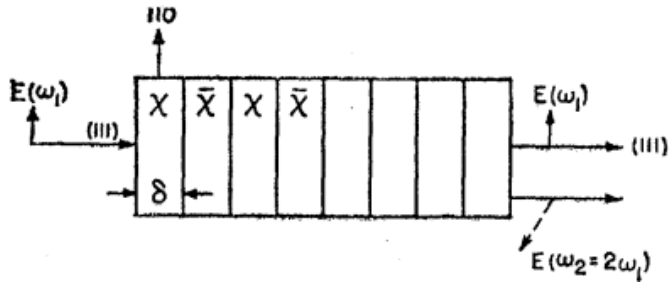

Figure 2. 1 A stack of thin plates of nonlinear medium periodically rotated by 180° to realize QPM [12].

Over the past 40 years, improvements in photolithography method and breakthrough in external electric filed poling (EFP) make QPM a mature industrial technique. Parallel to the advances in technology are the emergences of abundant new materials and structural schemes, all of which have promoted the application of QPM in more areas. This chapter provides an overview of the milestones in literatures which have contributed to the developments of QPM. Specifically, four aspects of QPM technique are discussed, including commonly used QPM materials, advanced design of QPM structures, development of poling techniques for ferroelectrics crystals and QPM structures visualization methods.

2.2 QPM materials

With increasing demands for QPM technique operating at higher efficiencies over a broader range of powers as well as extended wavelength ranges, increasing attention has been paid to other parameters of QPM materials besides nonlinear susceptibility. These parameters include low absorption and scattering losses, high surface-damage threshold, high thermal conductivity, low thermo-optic coefficients, ease of crystal growth and processing, and environmental stability. This subsection gives a brief literature review on two kinds of commonly used QPM materials, including ferroelectric crystals and orientation patterned semiconductors.

2.2.1 Domain engineering in ferroelectrics

Lithium niobate ($LiNbO_3$ or LN) is a negative uniaxial ferroelectric crystal with 3m point symmetry at room temperature [45]. The structure can be

visualized as a hexagonal close-packed configuration forming oxygen octahedra, as illustrated in Figure 2. 2 (a). In the ideal stoichiometric composition, meaning a ratio of Li: Nb: O = 1: 1: 3, the centres of these oxygen octahedra are filled one third by each of lithium ions, niobium ions and vacancies. However, because of the weaker bond of Li^{+} - O^{2-} comparing with the Nb^{5+} - O^{2-} bond [46], Li incorporation into the crystal is difficult, resulting in a tendency towards the congruent composition of Li: Nb = 0.942 [47]. Congruent $LiNbO_3$ (CLN) is more common and technically easier to grow. All the $LiNbO_3$ crystals used in this thesis are CLN.

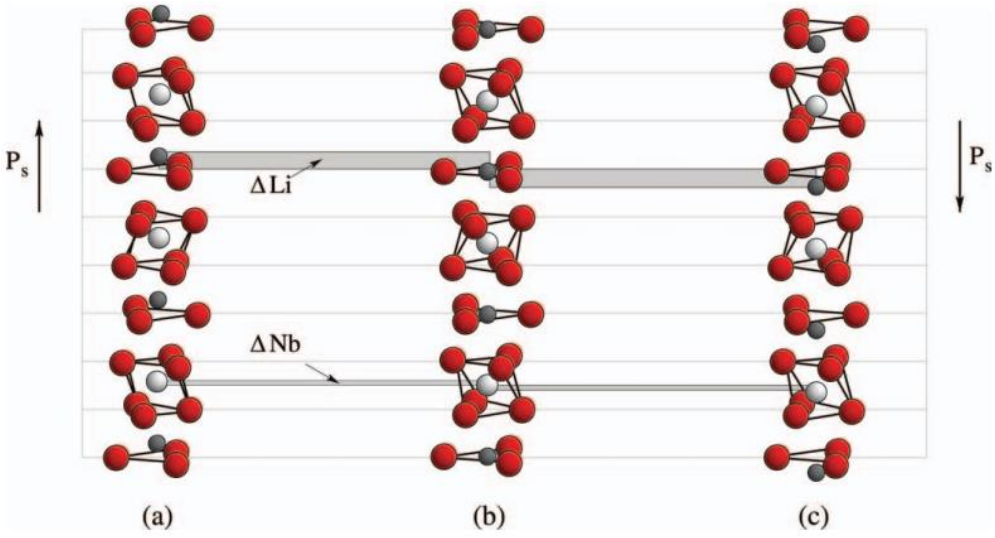

Figure 2. 2 Schematic of the structure of $LiNbO_3$ in the (a) and (c) ferroelectric phase and (b) paraelectric phase. ΔLi stands for the displacement of the Li ions (in gray) from the oxygen (in red) planes, whereas ΔNb stands for the displacement of the Nb atoms (in white) from their positions in the paraelectric phase. Both displacements occur along the crystal c-axis. Selected from reference [48].

The crystallographic orientation of $LiNbO_3$ is usually described with respect to a set of Cartesian (x, y, z) coordinates and the z axis, corresponding the crystallographic c axis, which is also the ferroelectric and optical axis of the crystal. Above the Curie point (around 1200 °C), $LiNbO_3$ is in the paraelectric phase. As shown in Figure 2. 2 (b), the Li atoms lie in an oxygen layer and the Nb atoms are at the centre of the octahedral oxygen cages. Below the Curie point, Nb atoms are no longer centred at the oxygen cages and the Li atoms are located either above or below the oxygen layers.

Because of the Coulomb repulsion, both cations are displaced in the same direction with respect to the oxygen layers, as shown in Figure 2. 2 (a) and (c). This atomic rearrangement yields two important consequences. The first one is that the crystal changes from inversion symmetric to noncentrosymmetric. This endows the crystal with second-order nonlinearity and makes it possible for frequency conversion applications. Second, the centre of mass of the positive and negative charges are displaced, giving rise to a spontaneous polarization as large as 0.7 C/m^2 along the z-axis of the crystal. A region with the same direction of spontaneous polarization is called a ferroelectric domain. By applying an external electric field with enough intensity to a domain region, the spontaneous polarization in the region can be reverted.

$LiNbO_3$ is an outstanding ferroelectric crystal for frequency conversion via QPM, not only for its desirable properties like broad transmission window (0.35 to 4.5 μm) and large nonlinear susceptibility [49], but also for its mature growth and processing industry, which make it relatively easy to obtain with different optical grades, crystal cuts, stoichiometries and dopings [50-53].

Although $LiNbO_3$ crystal is a versatile material, the relatively low optical damage and the photorefractive effect hinder its applications in high power laser devices. These disadvantages could be eliminated by doping it with 5 mol% MgO, which would raise the optical damage threshold by 2 orders of magnitude and reduce the coercive field by 80% [54, 55]. Actually, the coercive field of MgO-doped $LiNbO_3$ (MgO: LN) crystal could be further reduced at elevated temperatures [56]. Sugita, et al. investigated the side growth of the inverted domains in periodically poled MgO: LN (MgO: PPLN) and proposed to utilize multiple short pulses for electric poling to suppress the side growth effect [57]. In 2003, Ishizuki and coworkers applied multiple short pulses to a 3 mm thick 5 mol% MgO: LN crystal which was heated to 80 °C, and succeeded in obtaining a domain structure with a period of 30 μm [58]. Two years later, they improved the thickness to 5 mm for MgO: PPLN as well as MgO doped periodically poled lithium titanate (MgO: PPLT) [59, 60]. In 2002, they reported a 10 mm thick MgO: PPLN, as shown in Figure 2. 3, and used it to construct an efficient optical parametric oscillator (OPO) with an output energy of 0.54 J [61]. Apart from $LiNbO_3$, crystals like

$LiTaO_3$, KTP, potassium titanyl arsenate ($KTiOAsO_4$ or KTA) and rubidium titanyl phosphate ($RbTiOPO_4$ or RTP) have also been demonstrated for QPM [62, 63], and the aperture could exceed 5 mm [64-68].

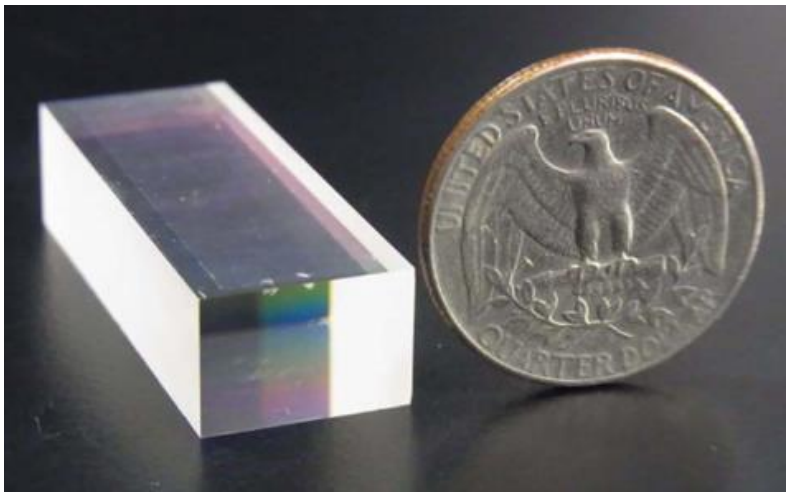

Figure 2. 3 A 10 mm thick MgO: PPLN crystal with QPM period of 32.2 μm [61].

In order to generate efficient nonlinear interactions, the ferroelectric crystals mentioned above require an elaborate poling process to obtain designed domain structures. This poling process usually requires complex and expensive photolithography equipment and high voltage electric field poling facility. In addition, usually one specially designed structure could only work for one wavelength or a very small wavelength range by tuning incident angle and temperature of the crystal. Working in another wavelength range would require another photolithography mask and poling a new crystal again. Of all the ferroelectric crystals, those as grown crystals with random-sized ferroelectric domains have natural advantage in nonlinear parametric processes. These as-grown ferroelectric crystals exhibit an irregular multi-domain structure with rod-like domains, which leads to spatially random modulation of the quadratic nonlinearity of the crystal [69-72]. Therefore, a pool of reciprocal lattice vectors with random orientations and random magnitudes, as illustrated in Figure 2. 4 (a), is available for phase matching over a broad spectrum of wavelengths without any temperature or angular tuning of the crystal. This technique is known as random quasi-phase matching.

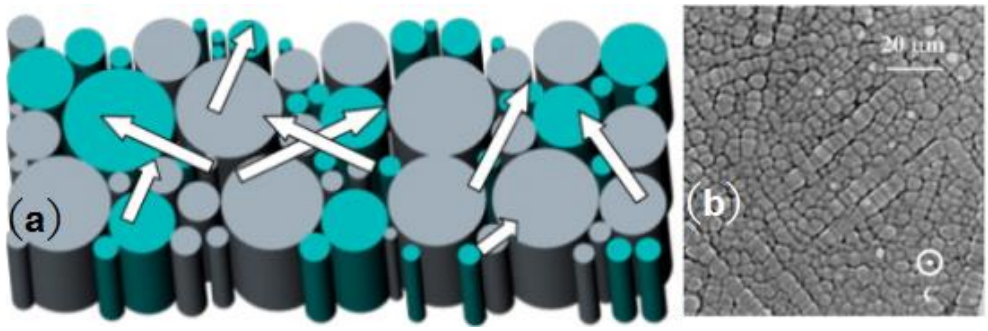

Figure 2. 4 Schematic diagram for reciprocal lattice vectors (represented by white arrows) in a randomly distributed domain structure. (b) Random domain structures in the *x*-*y* plane of a SBN crystal visualized after chemical etching [73].

A typical example of the as-grown random ferroelectric crystals is strontium barium niobate ($Sr_xBa_{1-x}Nb_2O_6$ or SBN), which is a ferroelectric solid solution between $BaNb_2O_6$ (BN) and $SrNb_2O_6$ (SN) with tetragonal tungsten bronze (TTB) structure and 4 mm point symmetry [74-76]. At room temperature, a SBN crystal possesses a spontaneous polarization along the *z*-axis. Figure 2. 4 (b) shows the typical random domain structure in SBN crystal visualized by chemical etching [73].

Apart from its random distribution of domain structure, other outstanding properties of SBN include high linear electro-optical and nonlinear optical coefficients, strong photorefractive effect and excellent pyroelectric property [77-79]. Therefore, SBN crystal has attracted a considerable attention in recent years for applications in nonlinear parametric interactions. In 1993, Horowitz and coworkers were the first to demonstrate quasi-phase matched SHG for a broad input wavelength range of 750-1064 nm in SBN crystals [80]. Later, the output wavelength range of SBN crystals has been extended to the whole visible and a part of near infrared spectral ranges [81-83]. Molina, et al. reported for the first time a qualitative observation of third harmonic generation (THG) in SBN crystals, which was the obtained by cascading of SHG and sum frequency mixing (SFM) [73]. Wang, et al. then obtained broadband THG in the range between 400 nm to 520 nm in SBN crystals, and quantitatively investigated the spatial and polarization properties of the emitted spectrum [84, 85]. Besides its applications in broadband frequency generation, SBN also shows great

potential for conical and planar emissions, femtosecond pulse monitoring and diagnostics, as well as frequency mapping from visible to infrared spectra [86-90].

However, the phase transition temperature, also known as Curie temperature T_c, of SBN is not very high. Sakamoto, et al. found that the solid phase of $Sr_xBa_{1-x}Nb_2O_6$ exists in composition where x = 0.25-0.75 [91]. Within the whole available composition range, the Curie temperature varies from 60 to 250 °C [92]. This is a main drawback of SBN for high pump power applications, where under increased temperature the crystal would undergo a transition to paraelectric state, and consequently the nonlinear optical effects would disappear. Therefore, finding new as-grown ferroelectric crystals with higher Curie temperature becomes a necessity.

2.2.2 Orientation patterned semiconductors

The infrared radiation has been widely used in spectroscopy, environmental gas monitoring, military confrontation, telecommunication and biomedical treatment, owing to its excellent properties including strong absorption by various molecular species, less prone to scattering from microscopic dust particles and water droplets [93-95]. Ferroelectric crystals like $LiNbO_3$, $LiTaO_3$ and KTP all have a multi-phonon absorption edge around 4 to 5 μm, which limits the infrared transmission range for these materials. Table 2.1 compares properties of $LiNbO_3$ and several semiconductors. We can see that semiconductors such as GaAs, GaP, ZnSe and GaN have broader transmission ranges in the infrared, as well as larger nonlinear coefficients comparing with traditional ferroelectric materials, making them ideal candidates for generating infrared radiations.

Table 2. 1 Properties of several QPM materials. Data selected from reference [96].

Material	Transmission range (μm)	Maximal nonlinear coefficient (pm/V)	Thermal conductivity (W/m·K)
GaAs	0.9-17	107	52
GaP	0.5-11	45	110
ZnSe	0.5-20	25	19
GaN	0.4-6.7	12	200
$LiNbO_3$	0.4-4.5	27	4.6

Since these semiconductors lack birefringence, QPM is necessary to ensure efficient nonlinear interactions. Unlike flipping ferroelectric domains in ferroelectric crystals, spatial modulation of the nonlinear coefficient in semiconductors is realized by varying the crystal orientation. Usually two kinds of methods were used to modulate the crystal orientation of semiconductors. The first one is to bond a stack of semiconductor plates with alternating orientations. Similar with the early stack-of-plate method in ferroelectrics, Fresnel reflections and transmission losses at the interfaces are non-ignorable. The second approach involves growth of orientation patterned semiconductors by epitaxial growth techniques. Owing to the mature epitaxial growth technique, orientation patterned semiconductors with total thickness up to 1 mm, periods down to 30 μm and attenuation as low as 0.005 cm^{-1} have been realized [96].

There are several other technologies for infrared light generation. Gas (helium–neon, CO_2) and solid state (Cr^{2+}: ZnSe, Er: YAG) lasers have very limited output wavelength range [97, 98]. Chemical lasers like hydrogen halide lasers can generate infrared radiations in wavelength range of 3-5 μm, but the complex structure, large equipment footprint and expensive construction are undesirable in real applications [99]. Recently quantum cascade lasers (QCLs) have been investigated for infrared emission from the mid-infrared (below 3 μm) to the far-infrared (~ 100 μm). However, the output power of QCLs is relatively low [100, 101]. Comparing with the above mentioned techniques, semiconductor QPM devices have several advantages. First of all, one single device can generate a broad wavelength

range in the infrared and the output average power is much higher. In addition, QPM based technique can be integrated with developed infrared fiber lasers, allowing for miniaturization of all solid-state laser devices.

2.3 Versatile QPM structures

With the increment of types of QPM materials, a large variety of QPM structures with different functions have been proposed and demonstrated. In the early days of QPM researches, scientists focused on finding poling techniques for fabricating QPM structures with high optical quality, large aperture and sub-micrometer periodicity. By meticulous designing of QPM structures, one single crystal with high performance and multifuncitons can be fabricated. The following paragraphs give a review on various QPM structures which can be used for a variety of applications like broadband frequency conversion, multistep parametric cascading processes, beam shaping, manipulation of quantum entanglement, etc [102-105].

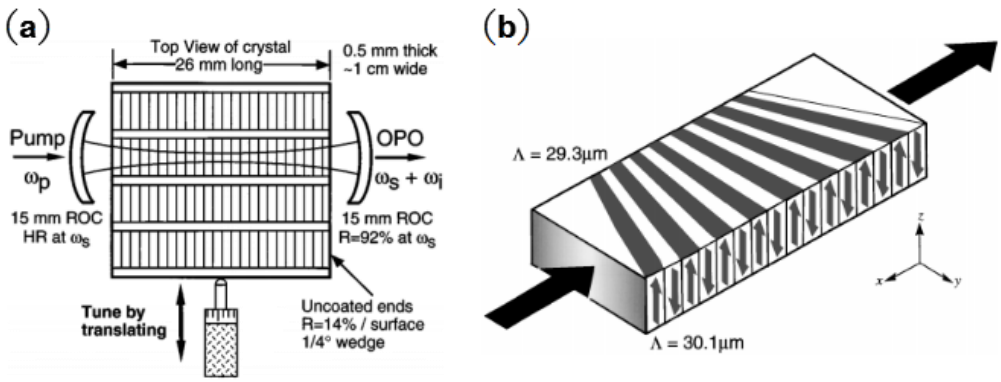

Figure 2. 5 (a) Multigrating QPM structure for OPO. By translating the crystal, the pump beam interacts with different grating sections. (b) A PPLN crystal with the fan-out domain pattern. The poling directions are indicated by the arrows on the side of the crystal [106, 107].

In order to obtain tuneable QPM structures in one single crystal, the simplest way is to use sequential or spatially varying QPM gratings. In 1996, Myers, et al. fabricated a PPLN crystal with 25 gratings in the transverse direction. The period of the gratings varied from 26 to 32 μm in 0.25 μm steps. By translation of the crystal through the resonator and temperature tuning, as shown in Figure 2.5 (a), they obtained tuneable infrared output

from 1.36 to 4.83 μm with a 1.064 μm pump laser [106]. An alternative method suggested by Powers, et al. is the so called fan-out grating design [107], in which the period is slowly changing from one edge of the crystal to the other, as shown in Figure 1.6 (b). This fan-out design provides a continuous tuning of output wavelength without temperature tuning, which is desirable for crystals that cannot be temperature tuned. Both two methods mentioned above are still widely used in tunable OPOs.

Apart from transversely varying QPM gratings, longitudinally sequential gratings can be useful for applications like generating cascaded nonlinear interactions. Kintaka and coworkers reported a THG of 355 nm ultraviolet light generated by a channel waveguide with two different periods of domain inverted gratings. The first grating is for SHG and the second one is for sum frequency generation (SFG) between the pump and the SHG [108]. Later, Bosenberg, et al. also reported generation of continuous wave 629 nm laser with a crystal consisting of two different gratings [109]. This method however limits the available crystal length and the conversion efficiency, because each grating period occupy one part of the crystal. In order to obtain higher conversion efficiency, investigations on aperiodic and quasi periodic domain structures, also known as optical super lattices, have attracted increasingly attentions.

Zhu and coworkers suggested to introduce quasi periodic domain structures into nonlinear optical materials for efficient high order harmonics [110]. They designed and fabricated a domain structure in which two antiparallel 180° domains building blocks were arranged as a Fibonacci sequence. Figure 2. 6 shows a detailed illustration of a typical Fibonacci quasi-periodic optical superlattice (QPOS), which can be used to generated efficient THG through a coupled parametric process of SHG and SFG. Apart from Fibonacci QPOS, a variety of other aperiodic and quasi periodic domain structures have been investigated, such as phase-reversed gratings, periodically chirped gratings and summed Fourier component gratings [111-113], just to name a few. By diversifying the Fourier spectrum of the domain structure, these aperiodic and quasi-periodic $\chi^{(2)}$ gratings can provide several

reciprocal lattice vectors for multiple phase matching conditions to be satisfied.

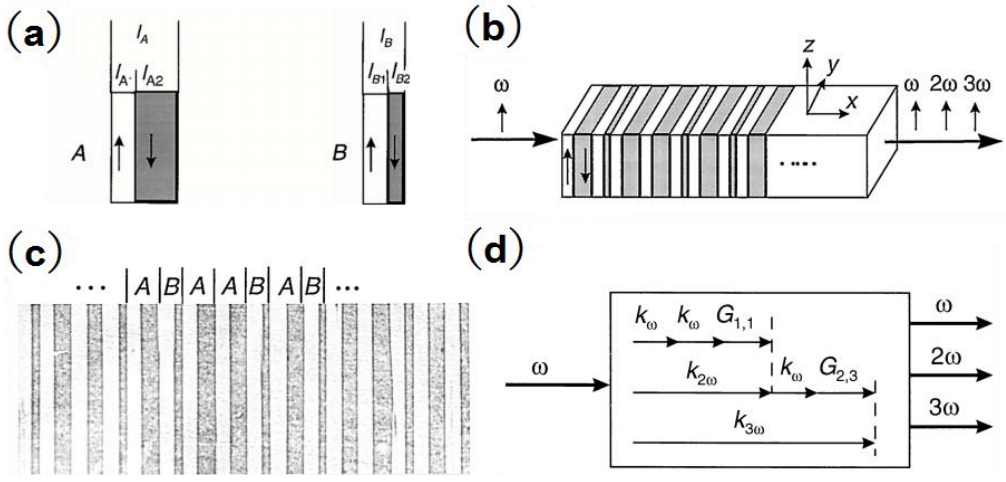

Figure 2. 6 Illustration of a typical QPOS. (a) Two building blocks A and B, each composed of ferroelectric domains with opposite directions, which are indicated by arrows. (b) A QPOS composed of two blocks arranged in Fibonacci sequence. The polarization of the FB is parallel to the *z* axis of the crystal in the THG process. (c) QPOS domain structures of a single $LiTaO_3$ crystal visualized after chemical etching. (d) Phase matching diagrams of the process of THG in a QPOS, which has two specially designed reciprocal vectors to compensate both mismatches in the SHG and SFG processes. Images selected from reference [110].

In 1998, Berger proposed to use crystals with two dimensional (2D) periodic nonlinear susceptibility for nonlinear frequency conversion [114]. These so called nonlinear photonic crystals (NPCs) have spatial variation of nonlinear susceptibility tensor while the refractive index is constant. Two dimensional NPCs increase the flexibility of the domain structures, and allow to phase match several different processes in different directions. Broderick, et al. first reported fabrication of a PPLN with a hexagonal domain pattern, as shown in Figure 2.7, which provides multiple reciprocal lattice vectors for efficient quasi-phase-matched SHG at different angles [115]. Other application examples of 2D NPCs include generation of third and fourth harmonics, simultaneous wavelength interchange, all optical deflection and splitting [116-119].

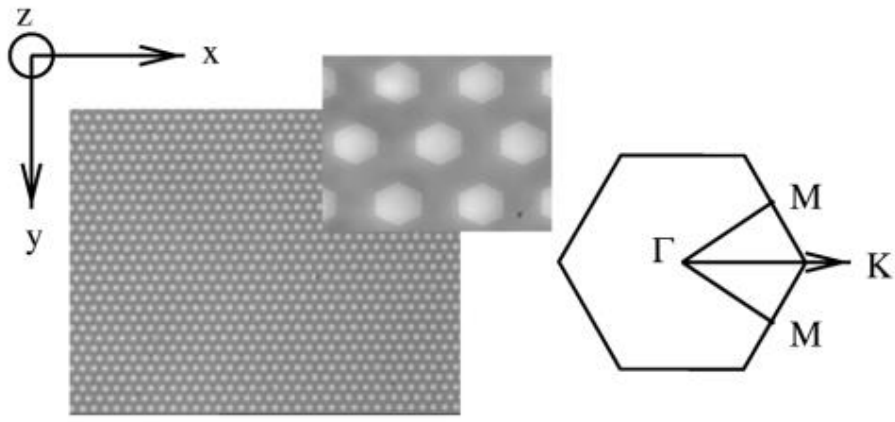

Figure 2. 7 Image of a 2D PPLN with a period of 18.05 μm and the first Brillouin zone [115].

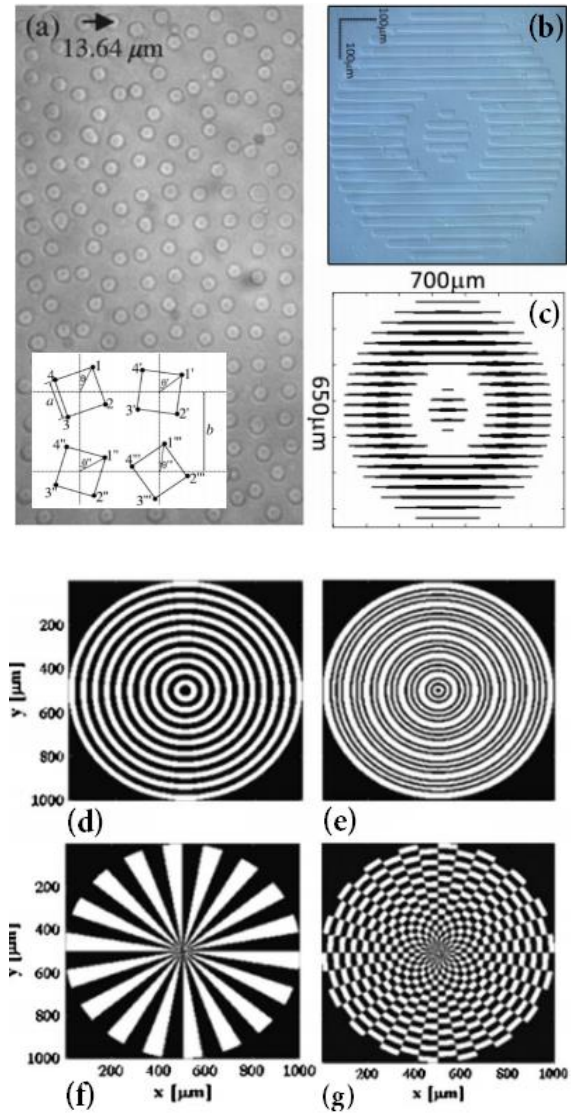

Figure 2. 8 Images of some quasi periodic and disordered 2D NPCs. (a) A short-range ordered NPC created by putting randomly oriented basic units, as shown in the

insert picture, on a square lattice. (b) Microscope image and (c) theoretical design of a NPC designed based on the concept of binary nonlinear holograms. (d-g) Family of radial photonic structures. The domains with opposite directions are denoted by black and white areas, respectively.

In 2004, Baudrier-Raybaut, et al. demonstrated that disordered polycrystalline ZnSe can produce 20 times more efficient difference frequency generation (DFG) than that obtained from an ordered ZnSe single crystal [120]. This has broken the existing perception that nonlinear frequency conversion should be done in crystals with ordered domain structures. Since then, the ideas of aperiodicity, quasi-periodicity and even disorder have been introduced to NPCs. For instance, short range ordered 2D NPCs, as shown in Figure 2.8 (a), have been demonstrated for broadband efficient SHG and even cascade THG [90, 121, 122]. Other more complicated structures like twisted NPCs and radial symmetric NPCs, also shown in Figure 2.8 (b-g), have been used in applications like cascading, nonlinear beam shaping, wave front engineering, nonlinear polarization switching and others [104, 123-125]. For instance, asymmetric nonlinear photonic crystal was used for nonlinear generation and manipulation of Airy beams by using three-wave mixing processes [126].

2.4 Poling techniques

Ferroelectric crystals are the most commonly used materials for various nonlinear-optical applications. The development and commonly used poling techniques for ferroelectric crystals are presented in this section. Early poling techniques for ferroelectrics were utilized during crystal growth. In 1980, Feng, et al. reported deliberate fabrication of a laminar domain structure in a Czochralski growth system, along with a demonstration of enhanced second harmonic generation (SHG) in lithium niobate ($LiNbO_3$) crystals grown in this way [127]. They applied a modulated electric current or an eccentric rotation to control the temperature fluctuation during crystal growth, which results in periodic solute concentration fluctuation, or the so called growth striation, along the direction of crystal growth. This growth striation induced periodic ferroelectric domains when the crystal cools through the Curie

temperature. Similar works were accomplished in chromium doped $LiNbO_3$ and lithium tantalate ($LiTaO_3$) [128, 129]. Fejer's group also reported the formation of periodic domains using laser-heated pedestal growth [130, 131].

Another way to fabricate domain structures is post-growth engineering of single domain crystals using chemical diffusion and impurities substitution [132, 133]. Fejer and his coworkers demonstrated periodic poled lithium niobate (PPLN) waveguide using titanium diffusion. They periodically deposited titanium on the +*z* surface of a $LiNbO_3$ wafer and a subsequent heat treatment in the 1000-1100 °C range produced domain reversal in the patterned areas. By utilizing this technique, they demonstrated the first quasi-phase-matched green, blue and infrared light generations [134-136]. Bierlein, et al. also fabricated periodically segmented potassium titanyl phosphate ($KTiOPO_4$ or KTP) waveguides by titanium diffusion [137, 138].

2.4.1 Electric field poling

All the poling techniques mentioned above were not suitable for mass production. The real breakthrough came with the invention of external electric field poling (EFP). In 1991, Matsumoto, et al. reported periodic poling of $LiTaO_3$ crystal by patterning aluminum electrodes on the +*z* face, heating to temperature near the Curie point, then applying a small voltage (~1.4 V) to the electrodes as the crystal cooled and flipping the spontaneous polarization at the electrodes [139]. Changing the orientation of spontaneous polarization or reversing the ferroelectric domain, is equivalent to changing the sign of $\chi^{(2)}$. By defining the ferroelectric domain structure through patterned electrodes, $\chi^{(2)}$ of the material becomes spatially modulated. Yamada, et al. then achieved a breakthrough in 1993, by demonstrating periodic poling of $LiNbO_3$ by external electric field at room temperature [140]. In order to avoid dielectric breakdown before the coercive field was exceeded, they used thinned $LiNbO_3$ substrates. They obtained high power of second harmonic generation (SHG) with a conversion efficiency of 600%/W. This result sparked interest in domain engineering by high voltage electric field poling (EFP) technique. Further optimization of this technique was accomplished by Myers, et al., who used lithographic patterning and a liquid

electrolyte consisting of LiCl in deionized water [141]. Figure 2.9 shows a typical setup for EFP. This technique has proved to be reliable for fabricating domain patterns with controlled period at a wafer scale. For instance, Myers demonstrated 3 inch diameter $LiNbO_3$ with uniform domain structures [142].

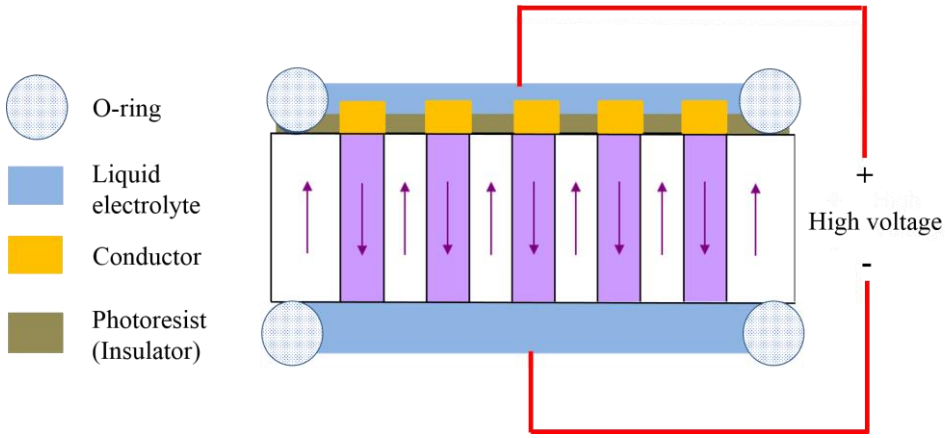

Figure 2. 9 A typical setup for electric field poling of ferroelectric crystals. Under the applied electric field will be reversed those domains below the patterned electrodes (conductor). The arrows indicate the directions of the spontaneous polarization after the poling process.

Although EFP is the most commonly used technique for domain engineering, it suffers from several drawbacks. The first is the relatively low resolution of inverted domain structures by EFP. Usually the minimal period is 3-5 μm and it remains challenging in fabricating domain structures with sub-micron period. This limits its application in areas like generating SHs in wavelength ranges shorter than visible light and generating backward SHs [66]. Although fabricating domain structures with a period of 700-800 nm has been recently demonstrated, these structures are restricted to one dimension [66, 143]. Also, the side growth of these inverted domains makes it difficult to accurately control the duty cycle of the structure. Secondly, the electric field could only be applied along the spontaneous direction to reverse domains. Therefore, in order to pole crystals like *x*- or *y*- cut $LiNbO_3$, it requires very complex electrode design [144, 145]. This is a significant disadvantage, since many devices require other crystallographic orientations, such as the electro-optic modulators and whispering gallery mode (WGM) harmonic resonators, where *x*-cut $LiNbO_3$ crystal is favoured. This drawback

of EFP also means it is almost impossible to fabricate three-dimensional domain structures using EFP. In addition, this poling technique is an inflexible method because of the requirement of specialized high-voltage poling setups based on photolithographically fabricated electrodes. Any new design or even a minor modification of the domain structure such as a change of its periodicity requires a new set of structured electrodes.

2.4.2 UV poling

Due to the strong absorption of UV light in ferroelectrics, the UV light induced high temperature near the surface of the crystal can reach and even exceed the melting temperature. The extraordinary high temperature as well as the precipitous temperature gradient result in two kinds of totally different effects on the crystal poling. One is the so called poling inhibition (PI) which denotes the effect that the area illuminated by UV laser resists of electric field poling. The other one is that intense UV radiation can directly reverse domains without any external electric fields.

Poling inhibition is a two-step poling technique consisting of UV illumination followed by homogeneous electric field poling. It has been demonstrated in a variety of crystals using continuous-wave (CW) lasers with wavelength ranging from 244 to 364 nm. Specifically, for $LiNbO_3$ crystals, all the poling inhibition experiments were performed on the $+z$ face of the crystal. Steigerwald, et al. investigated the physical origin of poling inhibition in $LiNbO_3$ crystals [146]. It was found that the lithium ions became mobile under the UV light-induced high temperature and diffused out of the irradiation area. Since basically the coercive field increases with the increase of lithium deficiency, the coercive field of the irradiated area is enhanced and therefore the designed domain pattern can be transferred to the crystal under a homogeneous electric field.

The poling inhibited domains are defined by the laser tracks, therefore are not confined by the lattice structure. It is also interesting that the PI domains are not sensitive to overwriting. This is demonstrated in Figure 2.10 (a), where two subsequent laser tracks produced crossed line domains without

indication of interaction with each other. In addition, the minimal separation between two PI line domains can be a few hundred nanometers, as shown in Figure 2.10 (b). However, the poling inhibited domains are very limited in depth (less than 5 μm), which restrict the application of this technique in fabricating real devices.

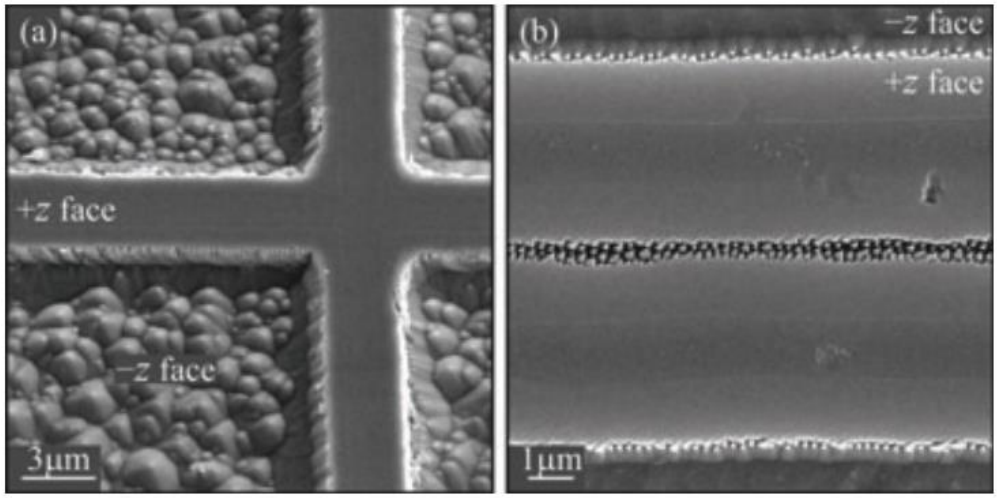

Figure 2. 10 SEM images of (a) a PI domain crossing obtained by two subsequent laser tracks and (b) two PI line domains with a submicron gap. Replotted from reference [147].

Under certain conditions, UV laser radiation can directly reverse domains in the irradiated area without application of any external electric field. This UV poling method has been demonstrated utilizing both CW and pulsed UV lasers.

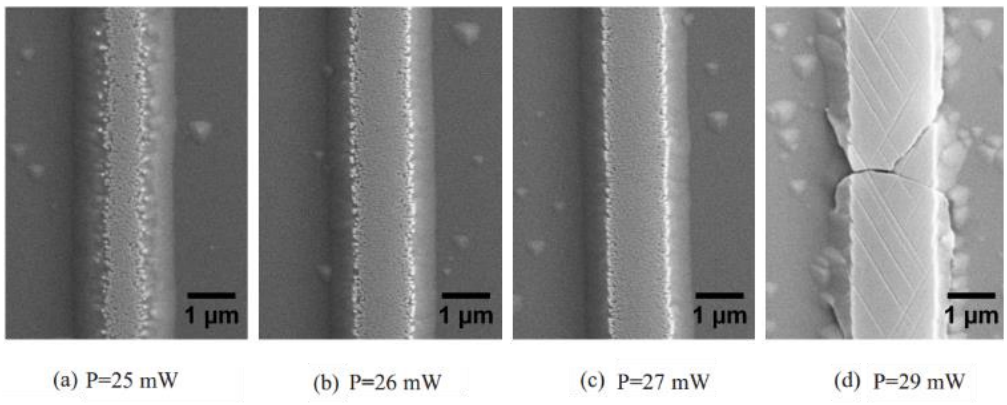

Figure 2. 11 SEM images of laser induced domain patterns on the -*z* surface of an etched undoped CLN crystal written with different incident powers. Replotted from Replotted from reference [148].

The use of CW UV laser to directly write domain patterns was first demonstrated by Muir and coworkers [148]. A UV laser of wavelength 244 nm was focused and scanned on both the positive and negative *z* faces of undoped CLN, iron doped CLN and titanium in-diffused CLN crystals. The optically poled domain patterns were visualized by both HF etching and PFM measurements. It was found that the quality of laser induced domains were strongly dependent on incident power. As shown in Figure 2. 11, when the laser power was low, the domain pattern consists of dense nano-sized domains and when the laser power was high enough, all the nano-domains merged into a continuous domain, which however was usually accompanied by undesirable thermal damage.

Muir, et al. found that using CW UV laser allows for a direct writing of domain patterns on both -*z* and +*z* surfaces of CLN crystals. However, the reversed domains on the +*z* surface could only be visualized by etching instead of piezoresponse force microscopy (PFM) [148]. This is because the depth of reversed domains on +*z* surface was only in the order of 10-20 nm, which is beyond the depth sensitivity of PFM measurement. They also proposed a model to explain the domain inversion process using CW UV laser, as well as the different behaviour on the two surfaces. Figure 2. 12 depicts a schematic diagram of the proposed model. Ferroelectric crystal possesses a spontaneous polarization P_s which is associated with an electric depolarization field E_{dep}. Before laser irradiation, the crystal is in equilibrium and E_{dep} is screened by free charges and defects in the crystal, which create a compensation field E_{scr} with the same magnitude but in the opposite direction to E_{dep}, as shown in Figure 1.9 (a). When the laser beam irradiates the crystal, Li and Nb ions move toward the paraelectric positions, which reduces the Ps and consequently E_{dep}. Because E_{scr} is too low to react [149], a net field E_{net} is created, as shown in Figure 2. 12 (b). In the meantime, the crystal absorbs the energy of laser and produces electron-hole pairs. A fraction of them drifts under the E_{net} and creates a photo-induced space charge field $E_{sc\text{-}ph}$, antiparallel to E_{scr}. When the crystal cools, the E_{dep} again increases and compensates E_{scr}, leaving a net field $E_{sc\text{-}ph}$. If the $E_{sc\text{-}ph}$ is higher than the coercive field, the domain will be reversed. This model agrees well with their

experiments results of dependence of domain width on the incident power and scanning speed. They attributed the different domain depths on the two faces to the different mobilities of electrons and holes generated near the irradiated surfaces.

CW UV lasers have also been used for direct domains writing on *x*- and *y*-cut $LiNbO_3$ crystals. This was was first reported by Steigerwald, et al., who found that the scanning direction of the laser beam had a great impact on the emergence and width of the reversed domains [150]. They suggested that the domains were inverted by a bipolar electric field which was created by laser induced temperature gradient. Further investigations carried out by Boes, et al. showed that, CW UV laser irradiation can not only write, but also erase previously written domain patterns, which makes it possible for tailoring domain patterns [151].

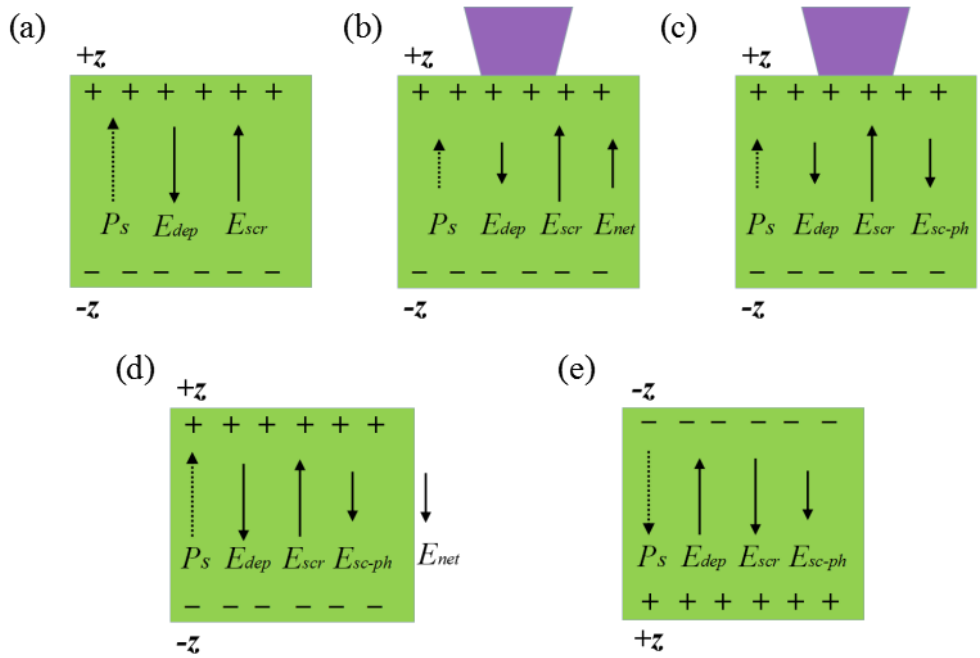

Figure 2. 12 Schematic of mechanism for domain inversion using CW UV laser beam. (a) Equilibrium state before laser irradiation. (b) Laser induced heat reduces P_s and E_{dep}, creating a net field E_{net}. (c) Charges separation produces $E_{sc\text{-}ph}$. (d) When cool, P_s and E_{dep} increase, creating a net field anti-parallel to P_s. (e) If $E_{sc\text{-}ph}>E_c$, then domain inverts. Replotted from reference [148].

Direct writing domains have also been demonstrated using pulsed UV laser irradiation. It was found that UV irradiation on the -*z* and +*z* faces of the

crystal lead to quite different domain patterns. Therefore, the results of irradiation on -*z* and +*z* faces are discussed separately in the following paragraphs.

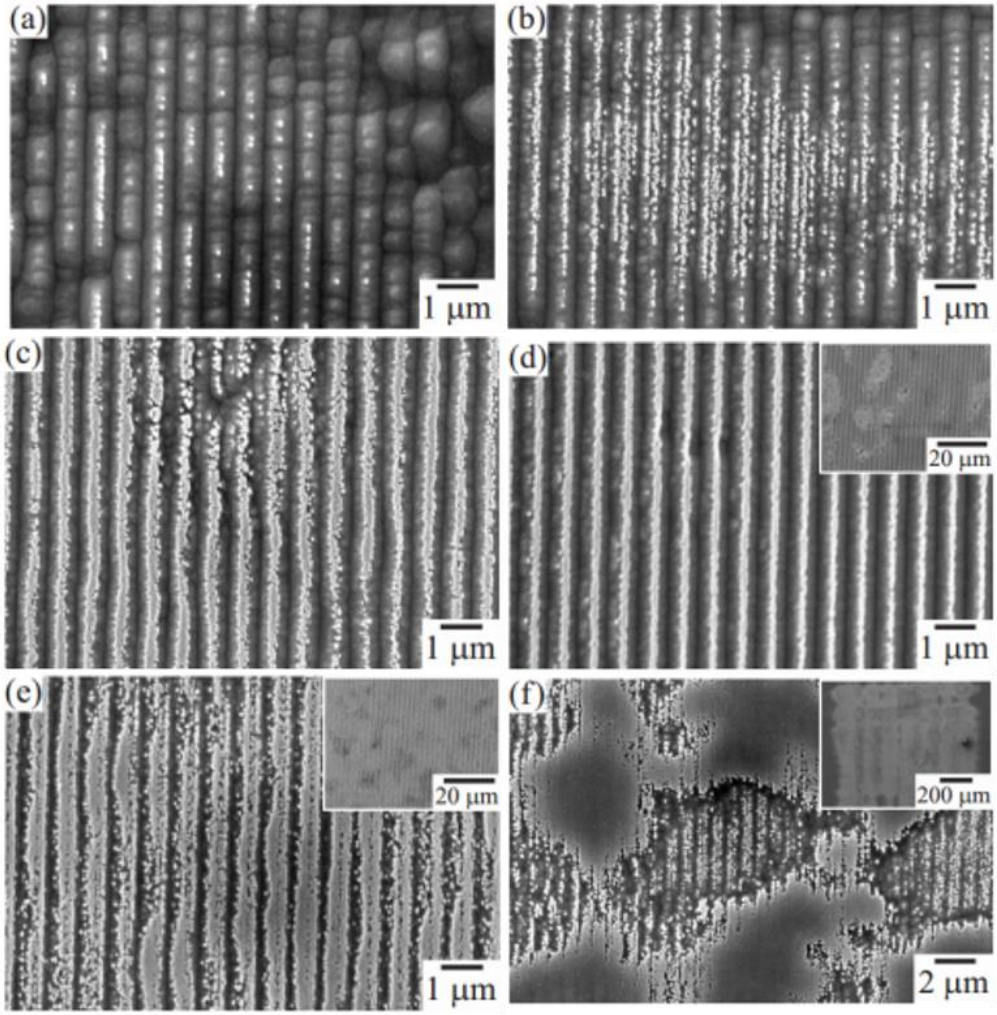

Figure 2. 13 SEM images of UV laser induced domain patterns using a 248nm laser beam with different intensities (a) 340, (b) 370, (c) 400, (d) 430, (e) 460 and (f) 490 mJ/cm2. A phase mask was used to form periodic domain patterns, which were revealed by HF acid etching. Replotted from reference [152].

In 2002, Mailis, et al. reported a modification of etching properties of the -*z* facet of CLN crystals after irradiating the crystal surface with the laser pulses of 248 nm [153]. Soon after many other researchers observed this phenomenon using pulsed UV lasers with different wavelengths and pulse durations [154-156]. Further PFM measurements proved that this modification was caused by domain inversion after UV laser irradiation. The laser irradiated area usually consists of arbitrarily distributed nano-sized

domains, which requires a phase mask to be transferred into desired structure. Valdivia and coworkers fabricated PPLN structures by illuminating the crystal with different intensity of incident beam through a phase mask [152]. As shown in Figure 2.13, with increasing intensity of the laser beam, the nano-sized domains become denser and form continuous domain lines in Figure 2. 13 (d). Further increase of the intensity results in widening of the lines and finally large areas of merged domains.

Irradiating the +*z* face of $LiNbO_3$ crystals can also produce domain patterns, which however have quite different morphology comparing with domains on -*z* face. As shown in Figure 2. 14 (a), self-organized domain patterns were obtained by using 298 nm UV laser pulses with intensity higher than the ablation threshold [152]. These domains consist of lines aligned parallel to each of the three crystalline *y* axes of the crystal. It is interesting that when approaching neighboring domain lines, they never join or cross each other. The width of the individual line was around 160 nm, which was not sensitive to the intensity of the laser, while the density of the lines increases with the laser intensity. In order to control the self-organized domain patterns to obtain desired domain structures, a phase mask which is orientated in one of the crystalline *y* directions of the crystal. Figure 2. 14 (b) shows such a periodic domain structure obtained by irradiating a 266nm laser beam through a phase mask. Most part of the structure was aligned along the grating lines however, domain lines parallel to the other two *y* directions were observed in the bottom part, which was caused by the inhomogeneous irradiating condition.

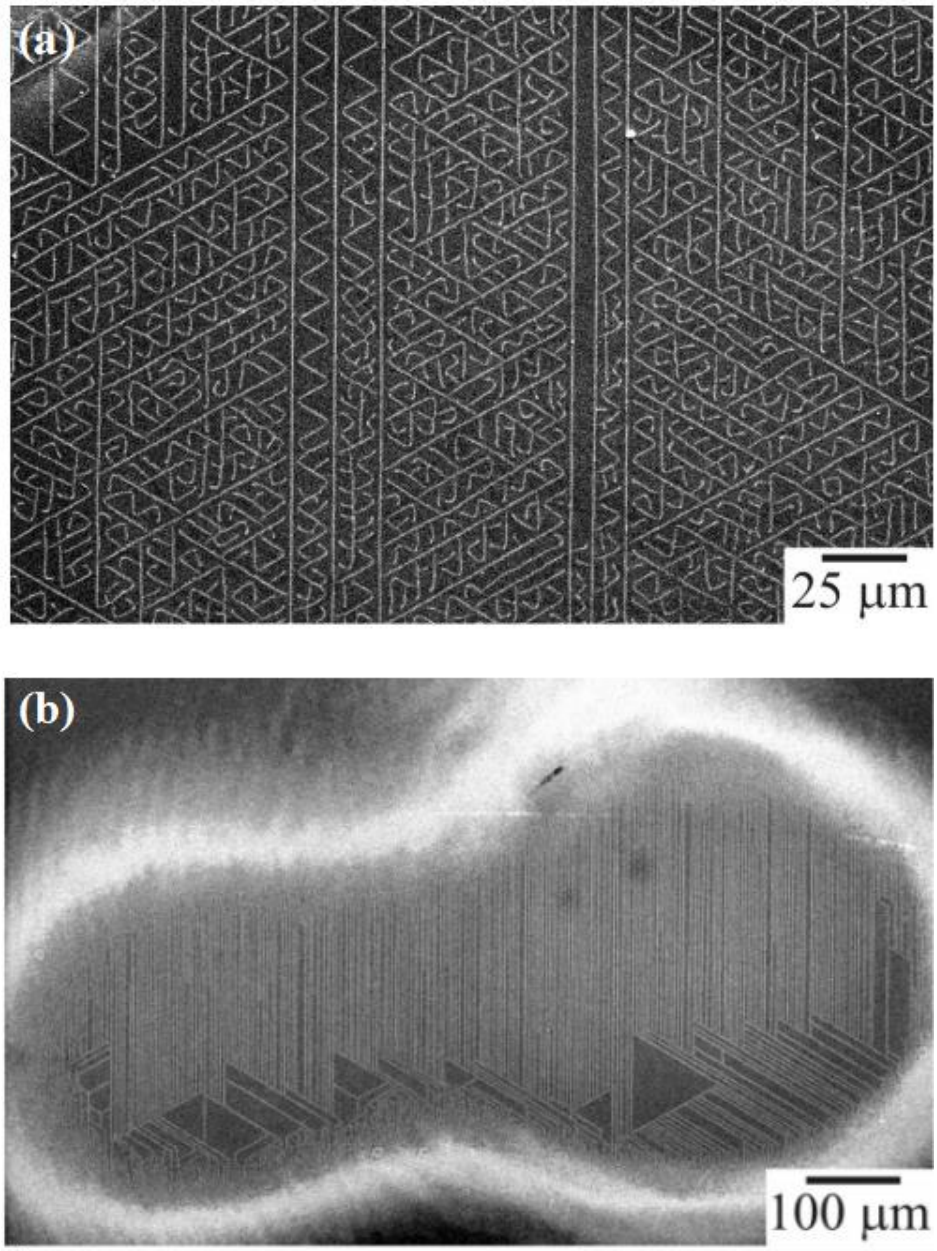

Figure 2. 14 SEM images of the +*z* face of undoped CLN crystals after pulsed UV laser irradiation and chemical etching. (a) Self-organized domain patterns without using a phase mask. (b) Periodic domain strucutre obtained by illumination through a phase mask. Replotted from reference [152].

Pulsed UV irradiation can directly reverse domains on both polar faces of CLN crystals. The exact mechanism is still under investigation, however, several factors connected with UV illumination may be responsible for domain reversal. Firstly, UV light is highly absorbed within a shallow depth of the crystal, and the induced high temperature creates a reactive ablation force, compressing the crystal and moving the Li and Nb ions closer to their

paraelectric phase positions [157]. As a result, the spontaneous polarization and the coercive field are reduced. Heating can also remove the surface compensation charge and reduce the effect of bulk screening, leaving the uncompensated depolarization field that supports domain inversion [158]. Secondly, UV laser possesses a photon energy higher than the band gap energy and therefore can excite electron-hole pairs directly. These photo generated charges can drift in the photovoltaic field, creating electric field that is opposite to direction of spontaneous polarization. Thirdly, in the cooling stage, pyroelectric charge can induce an electric field that may also play a role in domain inversion [148]. As for the different behavior of inverted domains on the $+z$ face of the crystal, it is believed that these domains are composed of charged domain walls with an angle to the spontaneous polarization. These charged domain walls are the source of the electro-static interaction between the UV laser reverted domains, forcing them to deflect along an alternative path when they approach each other. Regular domains have vertical domain walls which have no charge, and therefore tend to merge rather than deflect their growth [152].

Although UV laser poling can directly reverse ferroelectric domains without the need for photolithography and high electric field equipment, the rather small depth of inverted domains and the undesired damages are fatal drawbacks that prevent this method from fabricating nonlinear photonic devices for real applications. Up to now, no practical devices have been reported based on such UV inscribed ferroelectric domain structures.

2.4.3 Other poling techniques

Apart from EFP and UV poling, there are also other poling techniques. For instance, light-assisted poling (LAP) uses weakly absorbed laser beam (mainly visible to near IR range, but also some UV wavelengths) to reduce the coercive field of the crystal and a relatively lower homogeneous electric field to reverse ferroelectric domains [159]. The essence of this LAP method is still EFP. Other poling method uses scanning force microscopy or electron beam irradiation for micro to nanoscale ferroelectric domain engineering, but

the obtained domain structures are still limited to a very shallow surface layer of the crystal [160, 161].

2.5 Domain visualization

Domain visualization is an indispensable part of domain engineering process, not only because it can reveal whether the designed structure is realized, but also gives us better understanding of ferroelectric domain growth and helps us to better control the domain fabrication process. Therefore, domain visualization is usually required after or even during the fabrication process of domain structures. A variety of techniques have been proposed and demonstrated for this purpose. Some of them, like decoration of the crystal surface with charged particles to reveal the orientation of the domains, have relatively poor lateral resolution [162]. Other techniques, like transmission electron microscopy (TEM), have very high lateral resolution and even allow the detection of 90° domains, but require extremely thin samples [163]. This thesis mainly focuses on investigation of materials with 180° domains, which means anti-parallel domains with opposite orientation of spontaneous polarization or with different sign of $\chi^{(2)}$. In this section, three kinds of domain visualization techniques are presented and discussed. For more comprehensive introductions to domain visualization techniques, one may refer to the reference [164].

2.5.1 Chemical etching

Selective chemical etching is one of the most commonly used technique for high-resolution visualization of ferroelectric domain structures. The following figure illustrates the selective etching process in PPLN. Due to the different etching rates of the positive and negative ends of ferroelectric dipoles, domain structures can be revealed as topographical features. After chemical etching, surface profiling methods like scanning electron microscopy (SEM) and atomic force microscopy (AFM) can provide reliable images of domain structure with high resolution.

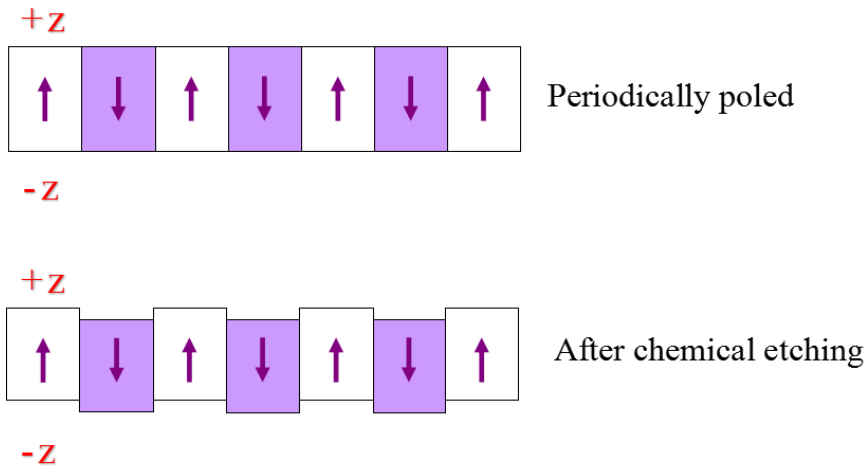

Figure 2. 15 Schematic of chemical etching of *z*-cut PPLN, viewed in cross section. The arrows stand for the direction of the domains (spontaneous polarization).

The first chemical etching experiment was conducted in Barium titanate ($BaTiO_3$) using hydrofluoric acid (HF) [165]. It has been shown that the positive end of the electric polarization etches much faster than the negative one. Since then, results for etching of domains in different crystals have been reported. Normally, the etchant for $LiNbO_3$ is pure HF acid or a 1: 2 mixture of HF and hydrogen nitrate (HNO_3). All the etching experiments for $LiNbO_3$ in this thesis were conducted in pure HF acid at room temperature. In this condition, it was reported that the etch rate of -*z* face of $LiNbO_3$ is about 0.8 μm/h, whereas the +*z* face remains virtually untouched after 600 hours [166].

Chemical etching is a fast, relatively simple method and can achieve a resolution < 0.1 μm. However, it suffers from several drawbacks. First of all, it is a destructive process for the surface of the crystal, which means the etched crystal may not be able to use for further applications. Secondly, it does not provide in situ visualization of domain reversal process. Lastly, it is almost impossible for chemical etching to visualize three-dimensional profile of domain structures. Chemical etching basically only reveals the surface domain structures. If we want to visualize the domain structure deep inside the crystal, a series of polishing and etching would be required. Considering the difficulty in rebuilding the three-dimensional profile with massive two-dimensional images of domains, as well as the time needed for the whole

process, it is virtually impossible for chemical etching to provide three-dimensional imaging of domain structures.

2.5.2 Piezoresponse force microscopy

As a variant of atomic force microscopy (AFM), piezoresponse force microscopy (PFM) can not only image the topography, but also the domain structures in a ferroelectric crystal. A typical experimental setup for PFM is illustrated in Figure 2.16. PFM was first demonstrated for visualization of ferroelectric domains by oscillating the probe tip on a $Gd_2(MoO_4)_3$ crystal and detecting the resulting electrostatic forces via a lock-in amplifier [167]. Kolosov and coworkers then improved this technique and observed the dynamics of domain growth with a resolution of 10 nm [168]. This is achieved by contacting a ferroelectric surface with a sharp conductive probe and applying an alternating current (AC) bias between the probe and the sample. Since all ferroelectrics exhibit piezoelectricity, the applied electric field results in changes of dimensions of the ferroelectric sample. For 180° domains, the electric field causes the domains to either extend or contract along the electric field direction. As for 90° domains, instead of piezoelectric deformation along the electric field direction, a shear strain appears in the ferroelectric, leading to displacements of the sample surface parallel to itself and perpendicular to the polarization direction. By moving probe over the sample surface, collecting and analyzing the deflection of the probe cantilever, domain structures can be imaged with high resolution. The following picture illustrates the working principle of PFM. A further development of PFM is the so-called scanning nonlinear dielectric microscopy (SNDM) [169]. The information about the local domain orientation is obtained by measuring the point-to-point variation of the nonlinear dielectric constant of the sample. This technique can achieve atomic scale resolution; however, this usually requires an ultra thin sample with 100 nm thickness [170].

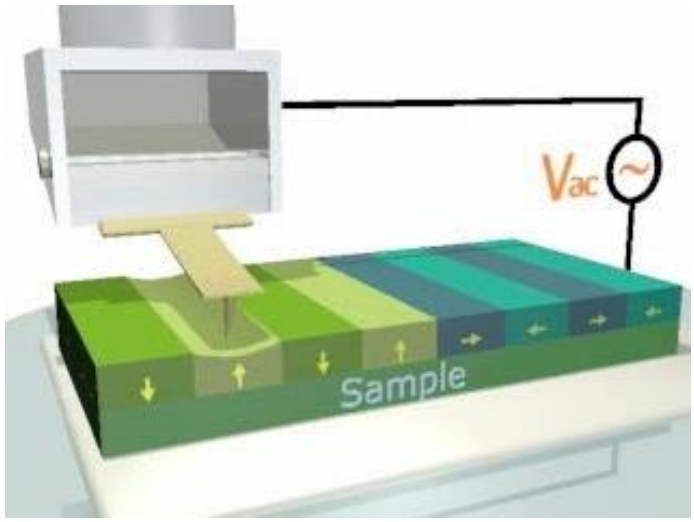

Figure 2. 16 Schematic setup for PFM. The arrow in each of the domain stands for the direction of the spontaneous polarization.

As a domain visualization technique, PFM is a nondestructive method with excellent lateral resolution and can monitor domain reversal in real time. However, the interpretation of the measurements is still challenging due to the physical complexity of ferroelectrics, as well as the quantities of possible interactions between the probe and the sample. In addition, the same with chemical etching, SFM cannot provide three dimensional images of domain structures.

2.5.3 Cerenkov second harmonic microscopy

The Cerenkov type frequency doubling process represents a nonconllinear SHG emitted at an angle determined by the longitudinal phase matching condition [27]. This name of Cerenkov SHG (CSHG) comes as a nonlinear analogy with the famous Cerenkov effect, which describes conical light radiation emitted when a charged particle moving at a speed greater than the phase velocity of light in the dielectric medium [171].

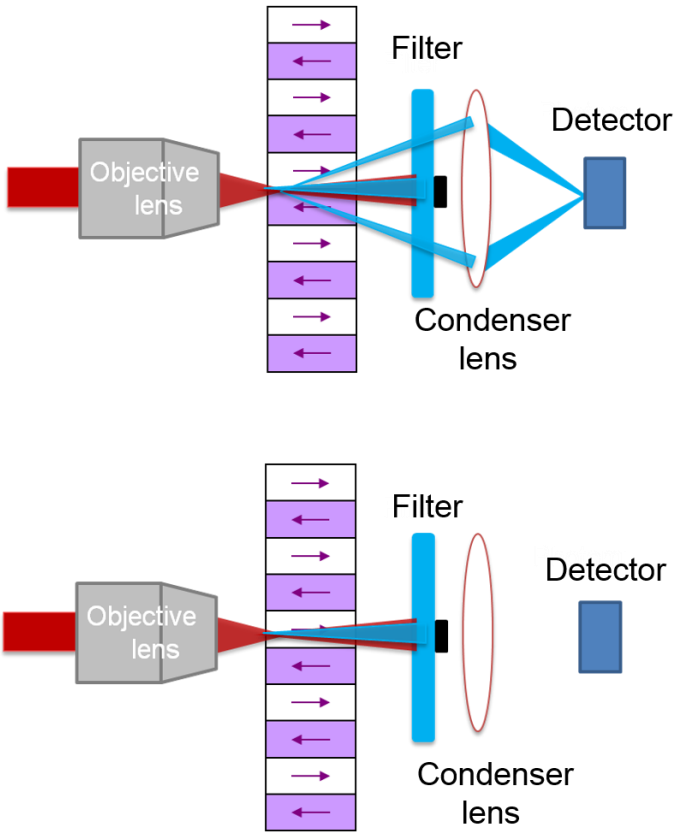

Figure 2. 17 Schematic of the CSHM. CSHG (a) can be detected when illuminating a domain wall and (b) is absent when illuminating inside a domain.

CSHG is observable when illuminating the boundary between two anti-parallel ferroelectric domains, while absent when the beam propagates inside a domain. By utilizing this special property, Sheng, et al. proposed to use CSHG as a tool for high resolution three-dimensional imaging of domain structures in NPCs [172]. Figure 2.17 illustrates the experimental setup for the so-called Cerenkov second harmonic microscopy (CSHM). The FB is tightly focused by a high numerical aperture (NA) objective lens. During the imaging process, the FB is scanning in three dimensions in a target zone inside the NPC. The collinear SHG is blocked and only CSHG generated in the NPC is collected by a condenser lens, measured by a photomultiplier and analyzed by a computer. This can eliminate the contribution of strong FB to the background noise. Since CSHG can only be detected when the FB illuminates a domain wall, a very high contrast between the CSHG from a domain wall and from a homogenous zone can be obtained.

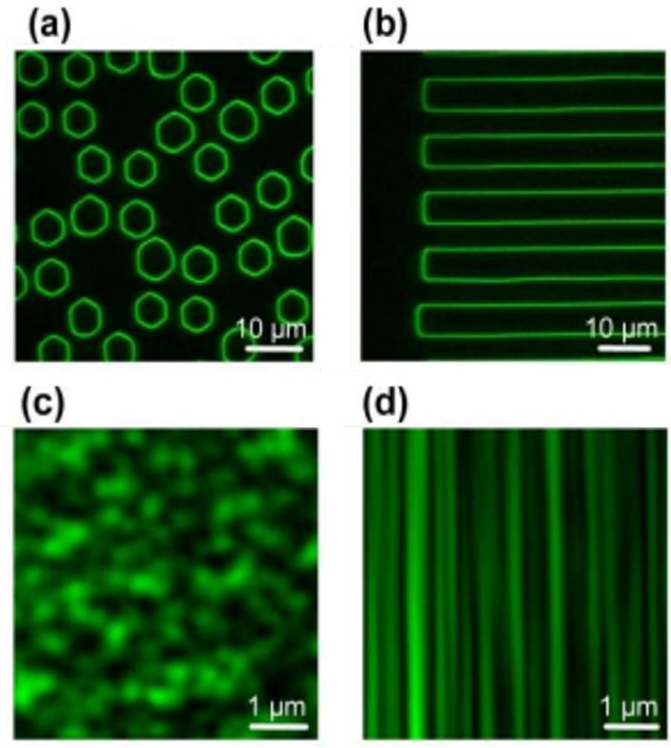

Figure 2. 18 Domain structures imaged by CSHM. (a) Congruent $LiNbO_3$ with 2D short-range ordered domain structure. (b) $KTiOPO_4$ with 1D periodic domain structure. As-grown SBN crystal at (c) *x*-*y* and (d) *x*-*z* planes, respectively. Images from reference [172].

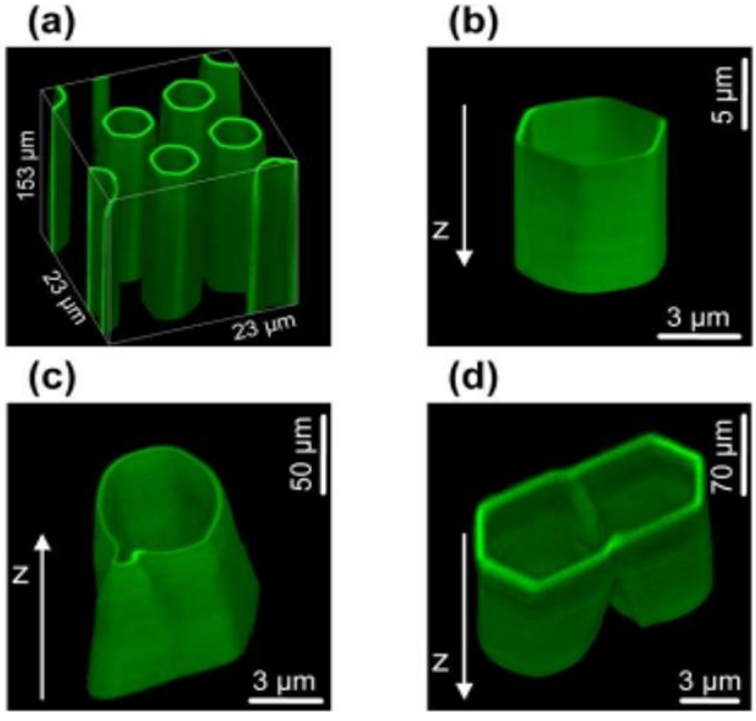

Figure 2. 19 (a) Three dimensional images of structures inside a CLN crystal recorded by CSHM. (b) Transformation of an initially circularly shaped domain to

hexagonally shaped (c) Formation of an irregular shaped domain due to the small defect in the domain pattern. (d) A merging process of two initially separated domains. Images from reference [172].

CSHM is a nondestructive technique which can provide direct imaging of domain structures with a sub-micrometer resolution. It has been demonstrated as a powerful tool for domain visualization in a variety of ferroelectric crystals, as shown in Figure 2. 18 [172]. It is worth mentioning that, the ability to provide 3D images of domain structures makes it an outstanding one comparing with other domain visualization techniques. This is realized by stacking 2D images recorded at different depths inside the NPC. Figure 2. 19 shows a group of 3D images of domain structures in a congruent $LiNbO_3$ crystal [172]. Figure 2. 19 (b) shows that a well-defined domain of initially circular shape on the +*z* surface transformed to hexagonal shape at a depth around 1 μm beneath the surface. Figure 2. 19 (c) and (d) show transition processes of irregular shaped domains. In addition, CSHM can provide real-time in situ monitoring of ferroelectric kinetics during the poling and growth processes of domains. Ayoub and coworkers reported an experimental investigation of monitoring the domain kinetics during an electric field poling process using CSHM [173]. They used an unpoled *z*-cut SBN crystal and applied an electric field stepwise until 4 kV/cm was reached. While increasing the electric field, a target region was scanned in three dimensional and the recorded images are shown in Figure 2. 20. We can clearly see the whole growth process of domains, including nucleation of nanosized domains, the growth of domains in length and lateral motion of the domain walls. Therefore, CSHM can help us better understanding the domain reversal process, and also better control of the fabrication of NPCs.

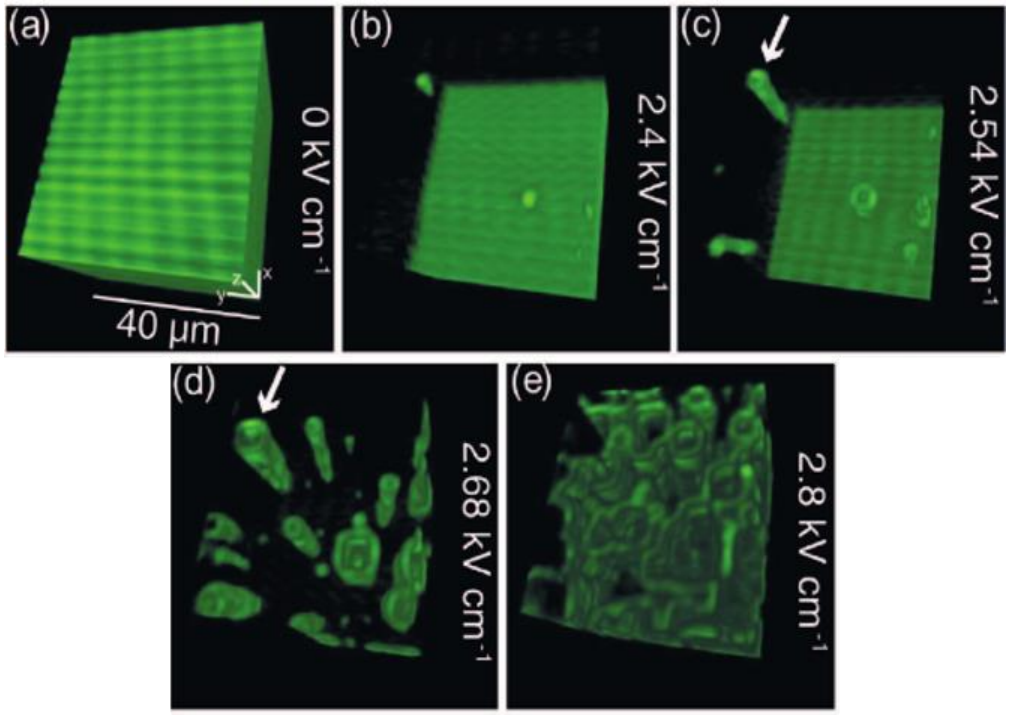

Figure 2. 20 Three dimensional images recorded by CSHM during the poling process of a *z*-cut SBN crystal. (a) Background signal for 0 kV/cm. (b-e) Growth process of domains with increasing electric field. Replotted from reference [173].

2.6 Summary

This chapter reviewed the early development of QPM technique in aspects of QPM materials, structures, domain engineering and visualization techniques. Reasonable selection of QPM materials, proper design of the structures, effective poling and visualization methods are key parameters that ensure efficient nonlinear interactions in the NPCs. Although the EFP has become a commercial and widely used technique for ferroelectric domain engineering, it suffers from inevitable drawbacks such as limited resolution, restricted crystallographic orientation and reliance upon inflexible photolithographic equipment.

Later it was found that intense light can assist EFP, and even directly reverse ferroelectric domains under certain conditions. UV direct laser poling has been used for fabricating domain structures with sub-micron resolution and also been applied in *x*- and *y* cut ferroelectric crystals. However, the optical poled domains were restricted to a very shallow subsurface layer and

were often accompanied with inevitable damages. Therefore, UV poling is an impractical method for ferroelectric domain engineering. Chapter 3 investigates the poling of $LiNbO_3$ crystals using IR femtosecond laser pulses in an effort to overcome the drawbacks of EFP and UV poling.

Chapter 3 All optical poling using IR femtosecond laser pulses

3.1 Introduction

Although, electric poling by means of periodic electrodes is at present conventionally applied to ferroelectric domain engineering, there has been growing interest to produce domain structures using light patterns [147], which can be manipulated more accurately with a resolution up to the diffraction limit. Therefore, it enables one to fabricate fine ferroelectric domains with better defined details than those produced by electric-field poling alone. Light mediated poling can also overcome the sensitivity of electric poling to the crystallographic orientation of the medium including the situation when the latter technique cannot be used at all [174]. As we discussed in chapter 2, the light field has been employed in ferroelectric domain engineering in two ways, i.e. LAP and UV laser poling. In LAP, selective illumination of the ferroelectric crystal leads to a spatially modulated coercive field E_c, which in turn results in spatially selective domain inversion with application of an external, homogeneous electric field [175, 176]. This method eliminates the need for structured electrodes, but still requires application of high voltage. The second approach represents the optical poling, where the illumination of a ferroelectric crystal with intense UV radiation (c.w. and pulsed) leads to local domain inversion via pyroelectric field, without applying any external electric field [148, 158, 163, 177-179]. The optical poling allows one to overcome a number of drawbacks of electric poling, in particular, the fundamental restriction that the electric field must be applied along the polar axis (i.e. *z* axis for $LiNbO_3$) of the crystal. Consequently, all optical poling allows one to create domain patterns in *x* or *y* cut wafers, which is otherwise difficult by using electric poling [144, 145]. However, as UV light is strongly absorbed by most ferroelectrics, the resulting ferroelectric domain inversion is restricted to a shallow surface layer

(few hundred nanometers) [151]. This severely limits the application of such optically created domain structures.

In this chapter, we present an experimental study on optical ferroelectric domain engineering using near-infrared femtosecond laser pulses. We show that the illumination of a $LiNbO_3$ crystal by focused ultrashort infrared pulses results in ferroelectric domain inversion, without applying any external electric field. Since the $LiNbO_3$ crystal is transparent in the infrared [53], the inverted ferroelectric domains are not confined to the surface, but extend deep into the crystal. As a demonstration of this poling technique, we fabricated an efficient QPM frequency convertor in a $LiNbO_3$ channel waveguide.

3.2 Experimental setup

The experimental setup of our optical poling is shown in Figure 3. 1(a). We used a 500 μm thick *z*-cut congruent $LiNbO_3$ (CLN) wafer which was mounted on a translational stage that can be positioned in three orthogonal directions with a resolution of 100 nm. The infrared laser was generated by a femtosecond oscillator (MIRA, Coherent) operating at 800 nm, with a pulse duration of 180 fs and a repetition rate of 76 MHz. The pulse energy can be continuously varied from 0 to 9 nJ by using a half wave plate followed by a polarizer.

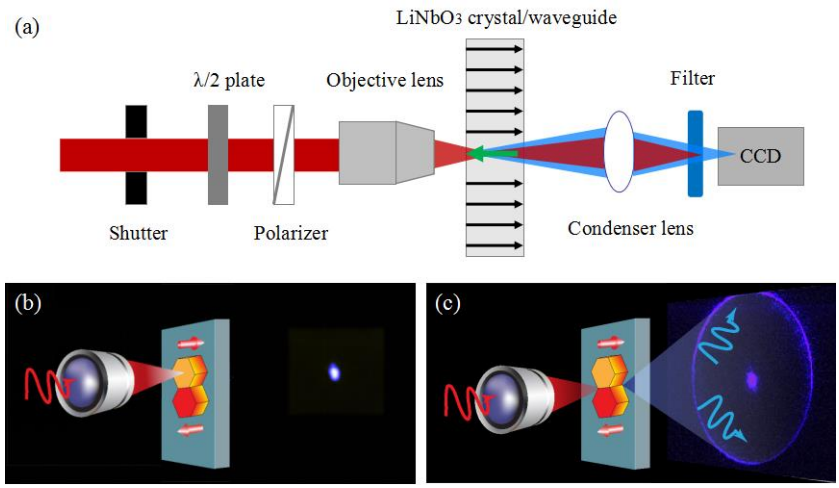

Figure 3. 1 (a) Experimental setup for femtosecond laser optical poling and in situ monitoring of ferroelectric domain inversion via Cerenkov second harmonic

generation. The black arrows in the sample indicate the direction of domains in the non-illuminated area, while the green arrow indicates the direction of laser reverted domain. (b) Only a collinear (forward) second harmonic signal is generated in a homogeneous area; (c) in addition to the collinear second harmonic signal, a conical Cerenkov signal is generated when a ferroelectric domain wall is produced.

A linearly polarized beam was incident normally to the surface of a $LiNbO_3$ wafer through a microscope objective. The shutter and the three axes of the translational stage were controlled by a computer using MATLAB programs. When writing a domain pattern, the shutter was initially closed, and the stage moved in three orthogonal directions to locate the beam on the front (-*z*) surface of the target position. Then the sample was translated along the *z* direction so that the position of the focal region moved from the -*z* toward the +*z* surface with an average speed of v = 10 μm/s. When the beam reached the back (+*z*) surface of the sample, the shutter was turned off and the stage moved to the next position and the process was repeated until the whole pattern was completed.

For an in-situ monitoring of the ferroelectric domain inversion, we used CSHG. In this process, the fundamental infrared beam generates two kinds of second harmonic signals. The first one, a non-phase-matched wave propagates collinearly with the fundamental beam. In addition, there is a non-collinear second harmonic signal emitted conically at the angle determined by the longitudinal phase matching condition. This Cerenkov signal is generated only when the fundamental beam illuminates a region, where $\chi^{(2)}$ is spatially modulated, for instance, a wall separating oppositely oriented ferroelectric domains [172, 180-183]. In other words, CSHG, which is normally not observable in a homogeneous ferroelectric crystal, will appear if a focused fundamental beam locally induces the domain inversion. To monitor the appearance of ferroelectric domain, we therefore used a lens and a CCD camera to collect and record the emitted Cerenkov second harmonic signal [see Figure 3. 1(a)]. We found that illumination of the crystal with a femtosecond beam led to the appearance of CSHG indicating the formation of spatially localized ferroelectric domains. The graphs in Figure 3. 1(b) and (c)

display typical images of second harmonic signals recorded before and after the ferroelectric domain inversion, respectively.

3.4 Domain engineering using ultra short pulses

Tightly focused femtosecond laser pulses with high peak energy can promote efficient nonlinear processes in transparent materials, including multiphoton absorption, optical breakdown, ionization and avalanche ionization. Sensible selection of laser parameters like wavelength, pulse energy, pulse duration and repetition rate enables nondestructive material modification and ablative laser machining.

In our experiment, the intensity of the laser in the irradiated position is a key parameter for laser writing. Here the laser intensity is mainly related to the incident power and the numerical aperture (NA) of the objective. Using the above mentioned experimental setup, we tried to write two dimensional dots with different NA (0.2, 0.3 and 0.65) and incident power. We found that with lower NAs and full power (about 700 mW), the IR laser irradiation could reverse domains. However, the laser reverted domains turned out to be randomly distributed domain islands after chemical etching, as shown in Figure 3.2 (a-b), which supposed to be two 5×5 domain matrixes with period of 30 μm. With NA 0.65 and incident power of 300 mW, the laser intensity was already high enough to reverse domains. In addition, the laser reverted domains were precisely distributed in the irradiated positions, as shown in Figure 3.2 (c). It was also found that there was a damage threshold above which the laser irradiation would produce ablation spots. Figure 3. 2 (d) shows ablation spots produced with NA 0.65 and pulse energy 5 nJ. Considering the beam size and NA of the objective we used, the estimated focus spot was 1.5 μm in diameter, which resulted in an ablation threshold F_{th} = 0.28 J/cm^2. This value is much smaller than the values using single laser shot in reference [184]. Apart from the difference in pulse duration, the main reason is that multiple laser shot in our experiment resulted in incubation effects which consequently lowers the ablation threshold in the crystal [185].

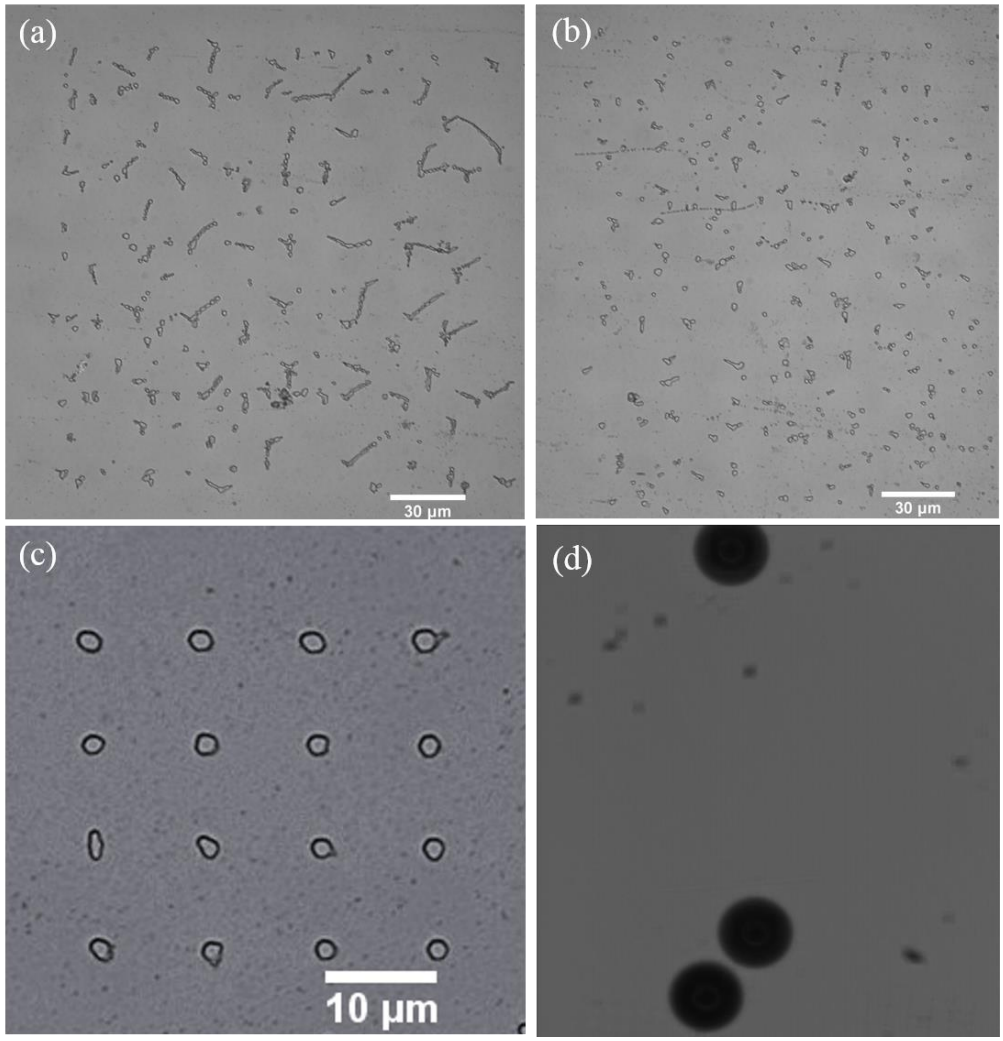

Figure 3. 2 HF etched domain patterns written with (a) NA 0.2 and pulse energy 9 nJ, (b) NA 0.3 and pulse energy 9 nJ, and (c) NA 0.65 and pulse energy 4 nJ. (d) Damages produced with NA 0.65 and pulse energy 5 nJ.

Using microscope objective of NA 0.65 and pulse energy of 4 nJ, we produced two-dimensional domain patterns with different periods. In particular, Figure 3. 3 depicts square lattices with periods equal to 2, 1.5, and 1 μm. The images shown in Figure 3. 2 depict the *z* surface of the samples after 5 min of etching in hydrofluoric (HF) acid. It is clearly seen that the inverted domains were uniform over the whole area. In our experiments, almost no domain merging was observed at a 1.5 μm separation between the centers of neighbouring inverted domains [Figure 3. 3(b)]. The average diameter of the inverted domains was less than 1.5 μm, which is comparable with the focal spot size of the femtosecond beam. The neighbouring ferroelectric domains merge when the distance between them is smaller than

1.5 μm, thus allowing the production of domains of various sizes and shapes [Figure 3. 3(c)]. Figure 3. 4 illustrates application of our optical poling technique to fabricate complex domain patterns. In particular, we show the optical microscopy images of square and hexagonal ferroelectric lattices, as well as decagonal quasi-periodic and short-range ordered domain structures.

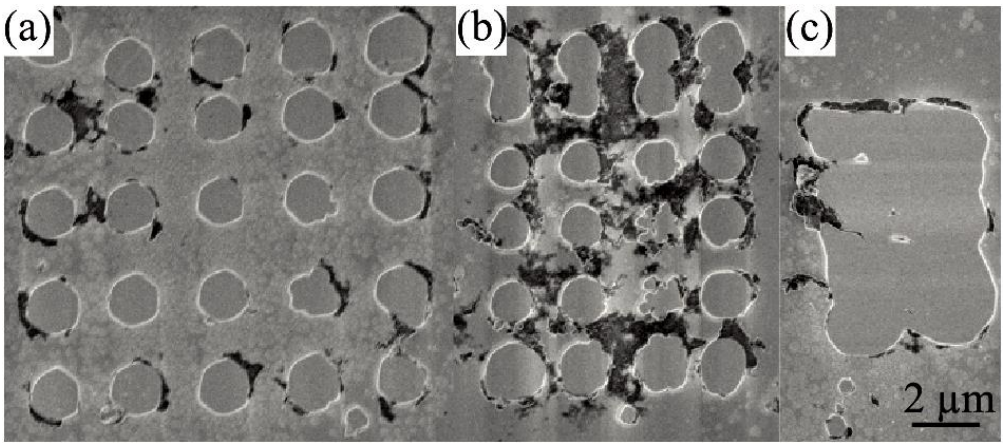

Figure 3. 3 Scanning electron microscopy images of square two-dimensional ferroelectric domain patterns (after HF etching) formed by infrared femtosecond laser optical poling. The period of the patterns is equal to (a) 2, (b) 1.5, and (c) 1 μm.

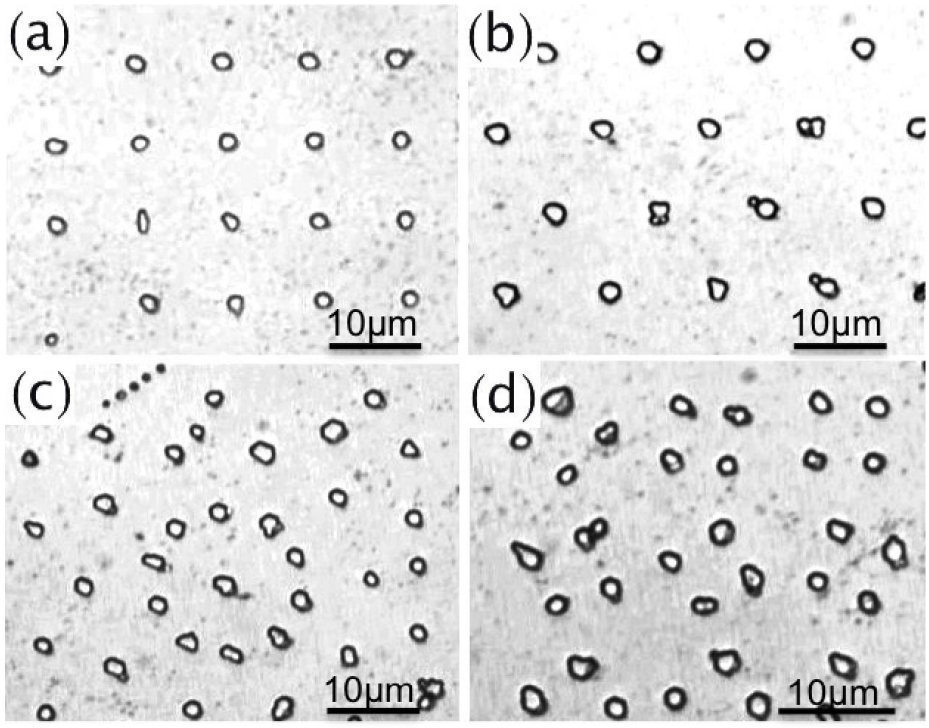

Figure 3. 4 Optical microscopic images of two-dimensional ferroelectric domain patterns (after HF etching) formed by femtosecond optical poling. (a) Square lattice;

(b) hexagonal lattice; (c) decagonal quasi-periodic; and (d) short-range ordered domain structures.

The reported here femtosecond domain inversion bears close similarities with the UV light poling technique [175, 178]. Therefore, it seems that in both cases we deal with the same underlying physical mechanism. We found, for instance, that domain inversion takes place only when the focus of the beam moves along the polar *z*-axis from the -*z* toward the +*z* surface. In fact, we could not observe any domain formation if the beam was tightly focused on the +*z* surface of the sample while efficient domain formation was taking place on the -*z* surface. These observations indicate the presence of thermoelectric or/and pyroelectric field in the focal volume of the femtosecond beam as a possible cause of domain inversion. In case of UV poling this field was induced by strong absorption of the UV light just below the surface of the crystal. The asymmetry of the thermal profile induces electric field of either thermoelectric or pyroelectric nature, which can locally invert the domain if it is oriented opposite to the direction of spontaneous polarization and its strength exceeds the coercive field. Since the thermal profiles at +*z* and -*z* surfaces are exactly opposite, only the profile near the latter surface results in thermoelectric field oriented against the direction of spontaneous polarization and hence is capable of domain inversion. As lithium niobate is transparent in the infrared, the multi-photon absorption of the high intensity light would heat the crystal in the focal area. While our fundamental wavelength 800 nm is too long for band to band two photon absorption (the band gap of lithium niobate is 4 eV) the process could involve two or higher order photon absorption as well as defects or impurity states within the gap [186]. The tight focusing within the crystal ensures high temperature gradient and, consequently, high strength of the poling field. In the region where this field exceeds the coercive field, the domain inversion takes place. Moving the focal spot toward the +*z* surface promotes the ferroelectric domain growth along the same direction.

It is worth mentioning that a different mechanism of domain reversal by ultrashort pulses has been proposed by Fahy and Merlin [187]. According to their theory the strong electric field of ultrashort pulses may accelerate ions in

ferroelectric crystal increasing their kinetic energy such that they would be able to switch between their two stable positions and subsequently flip the direction of spontaneous polarization. Lao, et al. claims experimental confirmation of this process [188]. However, no systematic studies of inverted domain structure had been presented in that work. We want to stress that this mechanism is entirely different from the one reported in our paper. First, in order to accelerate ions, the incoming beam has to be polarized along the polar axis of the crystal (*z*). In our experiments, the fundamental beam actually propagates along the z axis and is polarized along one of the other principal directions. Second, according to Fahy and Merlin, domain switching process should be very fast, on a picosecond time scale. In our experiments, the process of domain inversion was rather slow, so the crystal was illuminated with millions of pulses and this behavior clearly points towards time integrated process such as heating.

Having discussed the physical mechanism of domain inversion using IR femtosecond laser, we used CSHM to investigate the depth and quality of laser inverted domains in the *z* direction [172, 180, 183]. CSHM employs a weak, tightly focused fundamental beam that is scanned along the *x*, *y*, and *z*-directions inside ferroelectric crystal leading to the emission of Cerenkov second harmonic signal whenever the beam illuminates a ferroelectric domain wall. In this way, two- and three-dimensional maps of ferroelectric domain walls inside the crystal can be obtained. The power of this nondestructive technique is demonstrated in Figure 3. 5, which compares images of the same ferroelectric domain pattern inside a lithium niobate crystal obtained using traditional optical microscopy after HF etching [Figure. 4(a)] and the Cerenkov nonlinear microscopy [Figure. 4(b)].

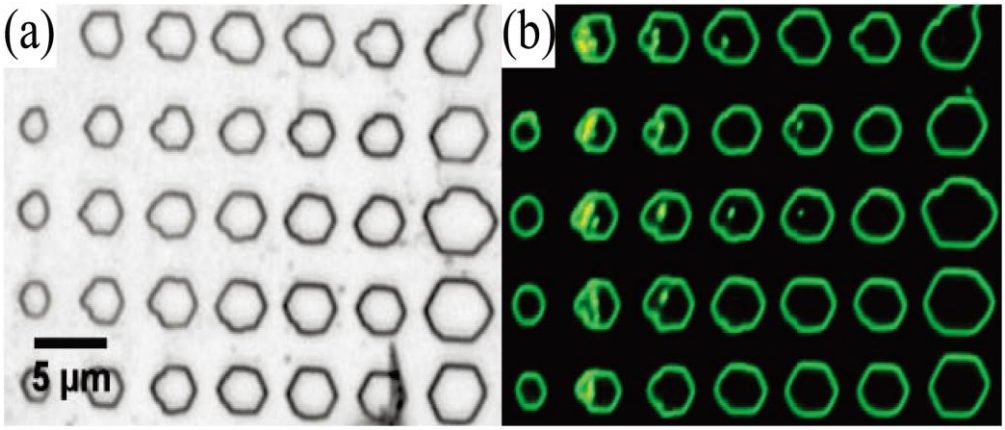

Figure 3. 5 Images of a square pattern of inverted domains in a lithium niobate crystal obtained (a) using optical microscopy of HF-etched samples and (b) Cerenkov second harmonic microscopy.

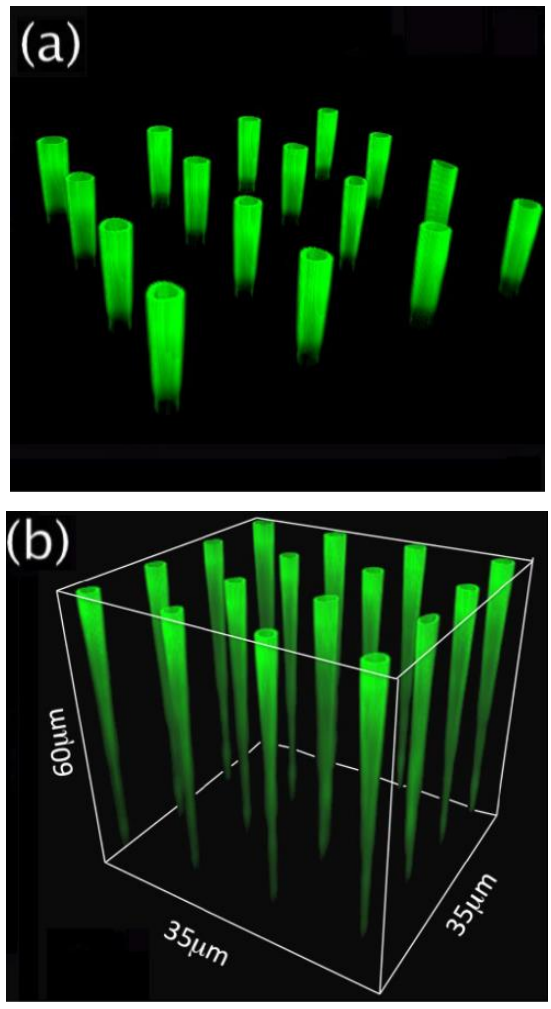

Figure 3. 6 Three-dimensional visualisation of a section of square pattern of inverted domains by Cerenkov second harmonic microscopy. (a) The first 15µm deep layer of the pattern (seen from the -*z* surface) illustrating good quality of the

inverted domains. (b) Degradation of the domains structure at greater depths inside the crystal.

The quality of domain reversal process is illustrated in Figure 3. 6, which depicts three-dimensional images of the section of the square domain pattern in lithium niobate from Figure 3. 2 (c). Figure 3.6 (a) shows the first 15 μm of the structure inside the crystal. It can be seen that our femtosecond optical poling indeed allows one to fabricate a high quality domain structure extending over tens of micrometers inside the crystal. In fact, we used a series of polishing and HF etching cycles to confirm independently the length of inverted domains inside the samples. It turns out that we were able to fabricate domain structures extending up to 60 μm into the crystal. However, at this depth domains were of rather poor quality. This is illustrated in Figure 3. 6 (b), which depicts the three dimensional image of the same fragment of the square lattice but extended deep inside of the lithium niobate crystal. The gradual deterioration of the domains is clearly visible.

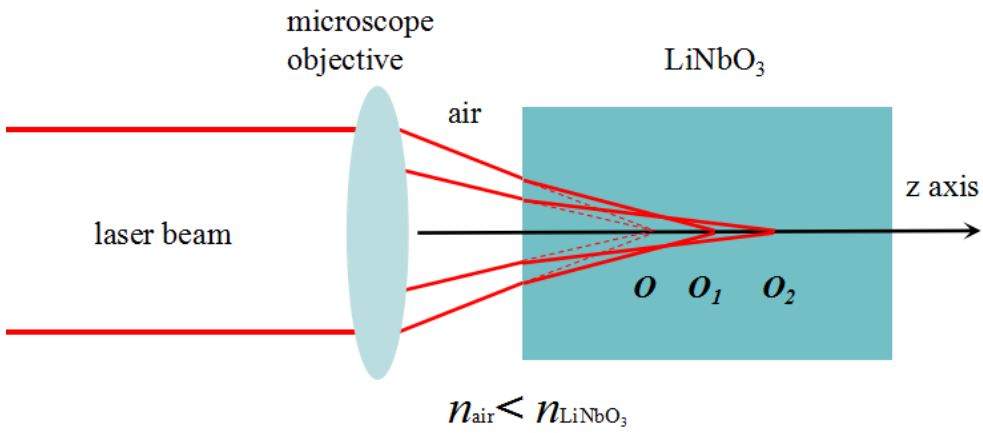

Figure 3. 7 Focusing of a plane wave laser beam through an interface of air and a $LiNbO_3$ crystal. *O* is the geometrical focus, while O_1 and O_2 are the aberrated focuses.

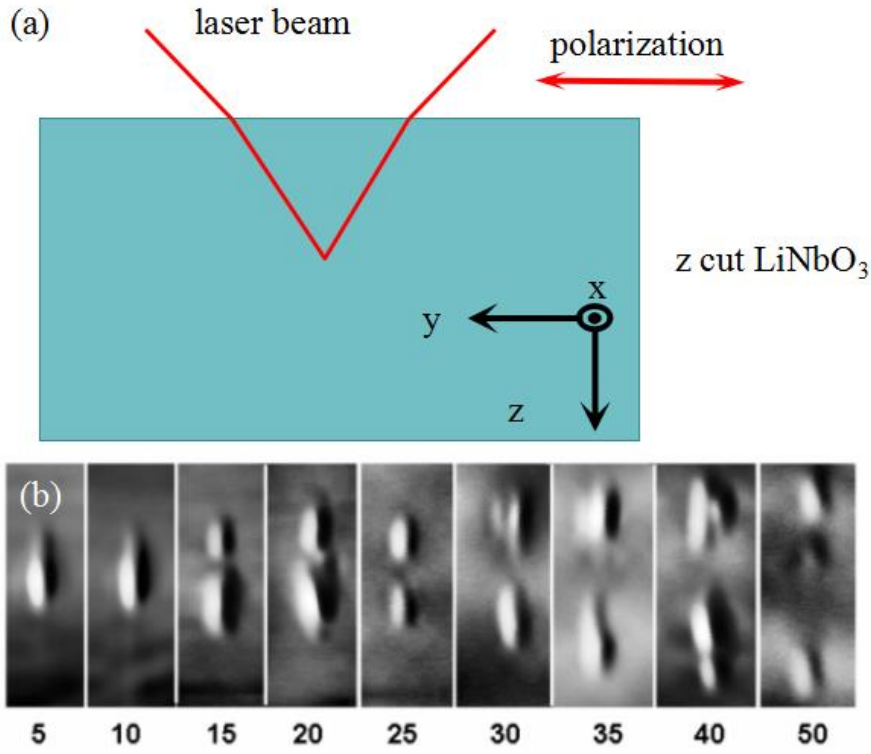

Figure 3. 8 Focus splitting in *z* cut $LiNbO_3$ crystal. (a) Writing amorphous regions, also known as voxels, along *z* direction of a $LiNbO_3$ crystal. Focus depth ranges from 5 to 50 μm. (b) Confocal transmission microscopy images of voxels in $LiNbO_3$, which resemble the corresponding intensity distributions in the focal region. Replotted from reference [189].

This is a consequence of few factors. First, the process of domain formation deep below the surface is affected by the properties of light focusing inside the crystal. It has been well known that high refractive index mismatch between lithium niobate and surrounding medium introduces spherical aberration, which under focusing conditions, leads to axial deformation of the focal region [190]. As shown in Figure 3.7, when the tightly focused laser beam is propagating from the air into a $LiNbO_3$ crystal, the rays of different incident angles are focused at different positions along the z axis of the crystal. As a result, light distribution in the focal region is enlarged along the axis direction the broadening of. Also, when light is tightly focused into a uniaxial crystal along its optical axis, focus splitting occurs [189]. Zhou, et al. observed this phenomenon when using tightly focused femtosecond laser beam to fabricate amorphous regions inside *z* cut $LiNbO_3$. As shown in Figure 3.8, focus splitting occurs at depths larger than

15 μm and becomes worse with increasing depth. All these effects reduce the peak intensity in the focus region and therefore limits the domain depth. In our experiments, no special measures were undertaken to counteract these effects. In principle, one may use spatial modulation of the incident beam to pre-compensate for the aberrations [191]. Second, domain reversal could be affected by the temperature-induced stress in the crystal as well as the photorefractive effect. In fact, the refractive index change was observed in the experiment but it disappeared following the annealing of the samples in 200 °C. The role of these and other factors, such as the focal spot size, heat diffusion, and the ambient temperature, on the quality and efficiency of the domain reversal process will be the subject of further investigations.

3.5 All optical poled QPM structure

Recently, the fabrication of QPM structures in ferroelectrics using near-infrared femtosecond laser radiation, at which the ferroelectrics are transparent, has been reported [174, 192]. However, the approach used in that work relied on decreasing the value of the $\chi^{(2)}$ nonlinearity instead of reversing its sign. The reduction of the $\chi^{(2)}$ was achieved by partially destroying the crystallographic structure of the medium. The drawback of this approach is that the fabricated QPM structure lead to a low conversion efficiency (on the order of a few percent), and the light exhibited high scattering losses (tens of decibels per centimetre). This problem can be solved by using our all optical domain inversion technique, which reverses the sign of the nonlinearity from + $\chi^{(2)}$ to - $\chi^{(2)}$ instead of reducing its value [193]. Therefore, propagation loss caused by material modification can be eliminated and high conversion efficiency can be expected.

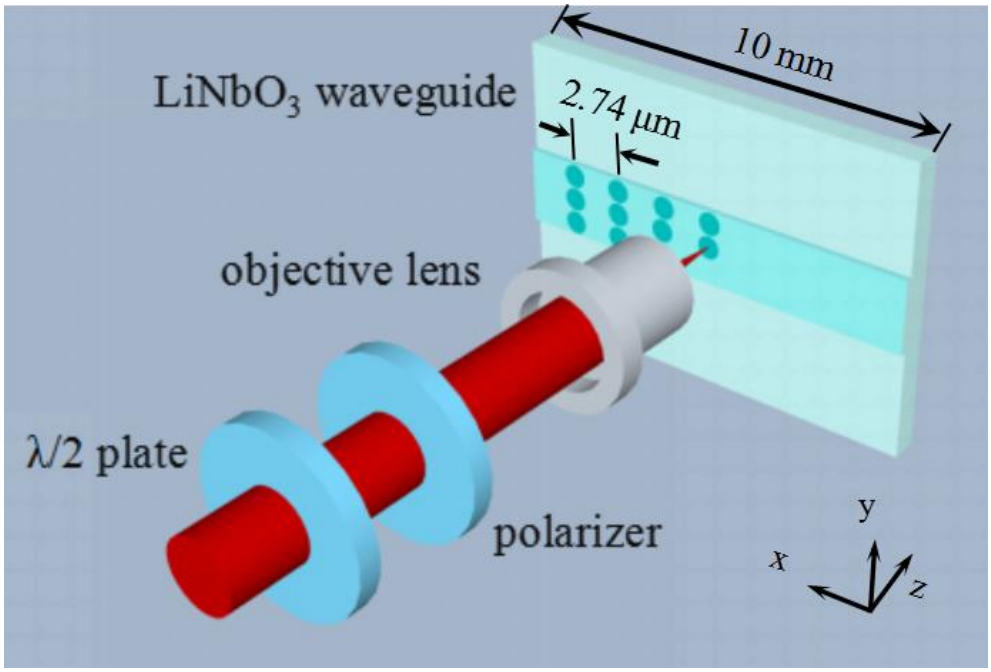

Figure 3. 9 Schematic of direct writing of ferroelectric domain patterns in a Ti:in-diffused $LiNbO_3$ channel waveguide using femtosecond infrared pulses.

Considering the fact that the depth of our laser inverted domains is in the order of tens of microns, we applied our technique to $LiNbO_3$ channel waveguides. The Ti-indiffused $LiNbO_3$ channel waveguide was formed on the -*z* surface of a 500 μm thick congruent crystal wafer. It was fabricated by diffusing a 35 nm thick Ti stripe with a width of 3 μm into the crystal surface, using a diffusion time of 22 h and a diffusion temperature of 1010 °C. The Ti waveguide was designed to be a single moded at the optical pump wavelength of 815 nm, with a refractive index contrast of approximately Δn = 0.001 and a mode depth of ~ 3 μm. The loss of the waveguide was measured to be around 0.1 dB/cm for both fundamental and second-harmonic TM modes.

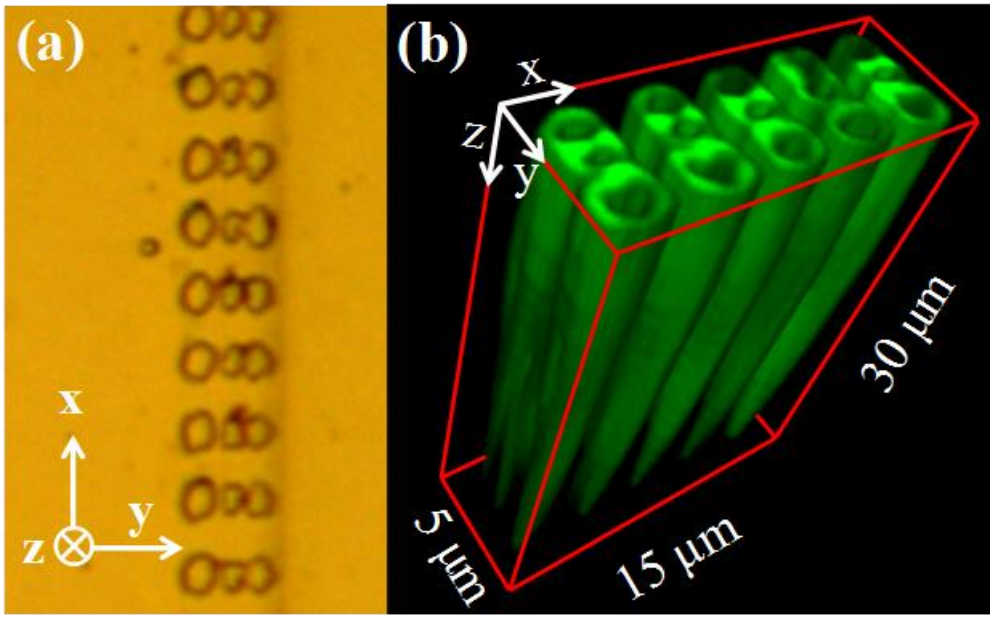

Figure 3. 10 Optical microscopic image of the 2-D optically poled domain pattern with the period of 2.74 μm in the *x* direction and 1.15 μm in the *y* direction. Individual inverted domains are visible as small circles. Waveguide boundaries are indicated with dashed lines. (b) Three-dimensional profiles of the inverted domains obtained by the Cerenkov second-harmonic microscopy.

For the fabrication of the inverted domains, the waveguide sample was mounted on a translational stage that can be positioned in three orthogonal directions with a resolution of 100 nm. The infrared light for domain inversion was generated by a femtosecond oscillator (MIRA, Coherent) operating at 800 nm, with a pulse duration of 180 fs, a repetition rate of 76 MHz, and a pulse energy up to 5 nJ. The light was focused by a 40 × microscope objective (NA = 0.65), and the diameter of the focus spot on the crystal surface was estimated to be around 1 μm [Figure 3. 9 (a)]. For each inverted domain, the focal spot of the laser beam was translated through the waveguide from the - *z* toward the + *z* surface with an average speed of v = 10 μm/s. An automatic shutter was used to block the laser beam when the sample moved to the next region of domain inversion.

Figure 3. 10 (a) displays a typical image of the obtained two dimensional (2-D) ferroelectric domain pattern after 5 min of etching in hydrofluoric (HF) acid. Prior to etching, the sample was annealed at 200 °C for 30 min to remove any residue of photorefractive effect from the domain inversion

process. The average QPM period is Λ = 2.74 μm (along the *x* axis), aimed at frequency doubling of 815 nm light. In the transverse direction (*y* axis), we realized domain reversion in a period as short as 1.15 μm. We also used the CSHM [172, 183] to visualize the 3D domain pattern and confirmed the inverted domains extending as deep as 28 μm [see Figure 3. 10 (b)] below the surface, therefore ensuring a good overlap with the waveguide modes of fundamental and second harmonic.

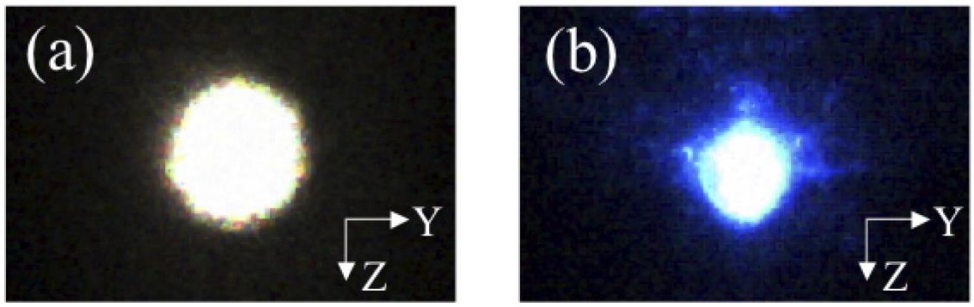

Figure 3. 11 Output intensity distribution of (a) the fundamental and (b) the second-harmonic waves in the far field. The coordinate system is that of the $LiNbO_3$ crystal.

The annealed $LiNbO_3$ waveguide with inscribed domain patterns was used to generate quasi-phase matched second harmonic wave. We used a NA = 0.1 microscopic objective to focus the 815 nm laser beam from the femtosecond oscillator (MIRA by Coherent) into the waveguide and collected the emitted second harmonic using a NA = 0.2 microscope objective. The polarization of the fundamental wave is parallel to the *z* axis of the $LiNbO_3$ sample (TM waveguide mode) to ensure that the largest nonlinear coefficient d_{33} is used in the frequency conversion process. Figure 3. 11 shows the far-field beam intensity distribution of the fundamental and second harmonic light after passing through the QPM structure. It can be seen that the beam shape is well maintained in the frequency doubling process and that, in both cases, the fundamental mode of the waveguide is excited, allowing for a high mode overlap between the fundamental and the second harmonic waves.

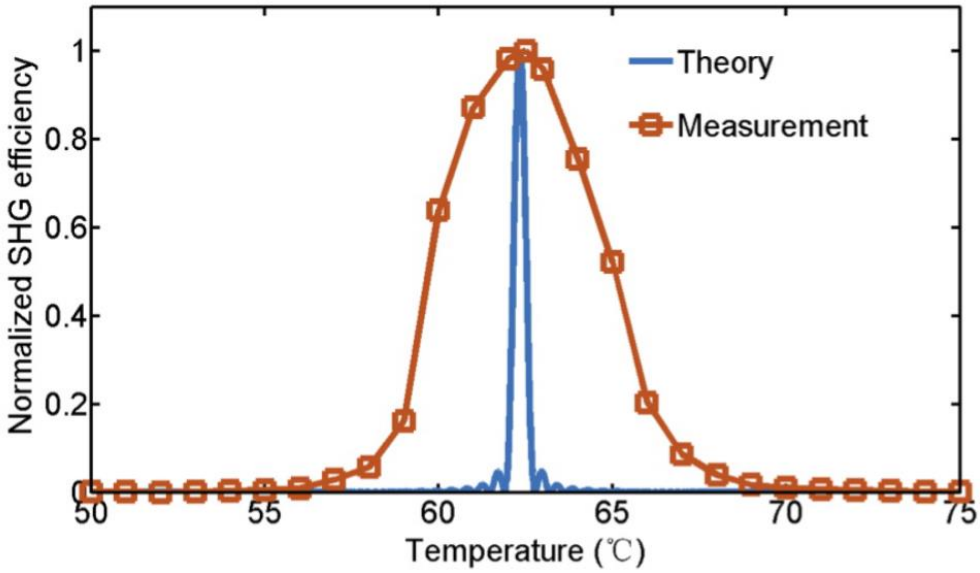

Figure 3. 12 Wavelength tuning response of the second-harmonic generation in an optically poled $LiNbO_3$ waveguide. The squares depict experimental results, while the narrow curve represents theoretical tuning curve of 10 mm long ideal periodic structure for a continuous wave case.

Temperature tuning was used to optimize the frequency doubling process of the optically poled waveguide, and it turned out that the maximal harmonic output occurred at 62.5°C (see Figure 3. 12). The measured temperature acceptance bandwidth is about 5°C, which is wider than theoretically predicted by using the Sellmeier equation for the $LiNbO_3$ crystal [194]. It is worth noting that the theoretic result represents the continuous wave case, while the experiment was performed with 150 fs pulses. The spectral width of such ultrashort pulses is around 15 nm. When the temperature of the waveguide is tuned away from the optimal value at which the central wavelength is quasi-phase matched, the contributions from the other spectral components to the second harmonic generation grow as they become phase matched. This results in the broadening of the experimental temperature acceptance bandwidth [195-197]. In addition, the group velocity mismatch between the fundamental and second-harmonic pulses restricted the effective interaction distance of the second-harmonic generation [196-198], which is about 83 μm in our case. The shorter the effective length is, the wider the acceptance bandwidth becomes [199]. Another major factor responsible for the broadening is the imperfection of the produced domain

structures. It is known that in any poling processes the random period errors are unavoidable. Such random deviations from the optimal QPM period will also shorten the effective interaction length of nonlinear processes and broaden the acceptance bandwidth [199].

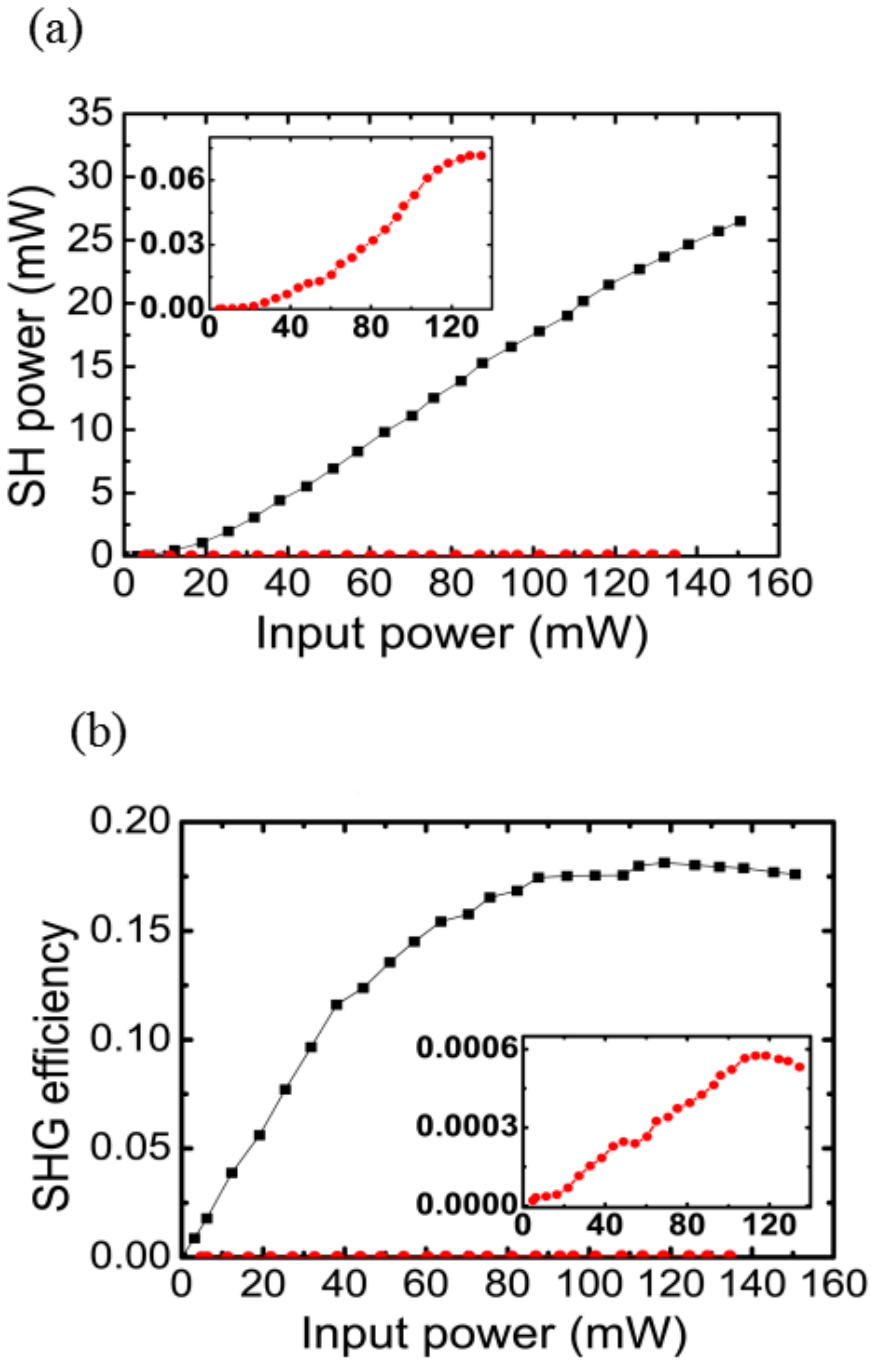

Figure 3. 13 (a) Average power and (b) conversion efficiency of second harmonic versus the average power of a fundamental wave at the optimal quasi-phase matching temperature 62.5 °C. The black squares and red dots represent the results

of quasi-phase matched and pure waveguides without poling, respectively. The inset depicts details of SHG in the latter case.

Figure 3. 13 shows the output average power and conversion efficiency of the quasi-phase matched SHG process as a function of the input power of the fundamental wave. The power of second harmonic follows the square law for low input powers. However, the growth slows down above 85 mW of input power as a consequence of back conversion. A second-harmonic power of 15.28 mW was obtained for 87.55 mW of input power. This corresponds to conversion efficiency of 17.45%, and the normalized conversion efficiency of 199.28% $W^{-1}cm^{-2}$. It should be noted that because our experiments were conducted with short pulses, the frequency conversion process was adversely affected by the group velocity mismatch between the fundamental and second-harmonic pulses [196-198]. The group velocity mismatch restricted the effective interaction length of a nonlinear process. The second-harmonic wave generated within this length can grow coherently. Beyond this length, the newly generated harmonic wave is essentially incoherent with the previously formed, but it still contributes to the total output. Therefore, one may expect an even higher conversion efficiency by using longer (picosecond or nanosecond) pulses and longer samples. For comparison, we also measured the SHG signal of the $LiNbO_3$ waveguide without domain inversion (shown with red dots in Figure 3. 13). It can be seen that periodic poling leads to over a 440-fold increase of the conversion efficiency. It is worth noting that the inscribed QPM domain patterns basically did not affect transmission characteristics of the waveguide. We have compared the output powers of the fundamental wave from the QPM and pure waveguides in an undepleted pump regime and found that an average propagation loss caused by the inscribed periodic domain patterns to be below 0.06 dB/cm, which is two orders of magnitude less than that measured in other femtosecond laser engineered QPM schemes[174, 192].

3.6 Summary

An optical approach to pole ferroelectric lithium niobate crystals using tightly focused infrared femtosecond pulses has been demonstrated. This technique

does not involve any external electric field at any stage of the poling process. The process of ferroelectric domain inversion as well as the quality of the reverted domains can be monitored and characterised via Cerenkov second harmonic generation, which is sensitive to the appearance of ferroelectric domain walls. Owing to the high transparency of a lithium niobate crystal in the infrared, we were able to produce inverted domains extending from the surface up to 60 μm inside the crystal. This is a significant result surpassing the capabilities of the optical UV poling technique, which usually enables domain inversion in a shallow layer (few hundred nanometers below the surface). The separation between the centers of neighbouring inverted domains was as small as 1.5 μm, thus allowing the production of fine two-dimensional structures. In fact, we expect to achieve even higher resolution of domain patterning by using spatial beam shaping and tighter focusing with oil immersed objectives. Finally, we have demonstrated fabrication of quasi-phase matched structures based on ferroelectric domain inversion in $LiNbO_3$ waveguides using this all optical poling method. The proposed scheme allows one to realize an efficient quasi-phase matching using the highest modulation depth of nonlinearity from $+\chi^{(2)}$ to $-\chi^{(2)}$, without introducing propagation loss for interacting waves. Conversion efficiency of 17.45% is measured for the second-harmonic generation in a 10 mm long domain inverted pattern. Our results indicate that the infrared laser poling constitutes a powerful method for fabricating periodic ferroelectric domains in an all-optical manner, thereby allowing for a wealth of new possibilities for precise and flexible domain engineering.

Chapter 4 Broadband optical frequency conversion using Calcium Barium Niobate crystals

4.1 Introduction

Ferroelectric crystal has been exploited in a wide range of devices since its discovery in the 1920s [200]. These devices include filters for wireless communications, modulators in optical circuits, and optical frequency converters in laser technology. Most of these functions are based on 180° antiparallel ferroelectric domains and the ability to engineer these domains on the micro or submicron scale [201]. Of the many ferroelectrics, those as grown with random-sized ferroelectric domains form a unique group. As far as application in nonlinear optics is concerned, the random domain pattern results in a spatially random modulation of the quadratic nonlinearity of the material. Thus, a pool of reciprocal lattice vectors with random orientations and random magnitudes is created to phase match nonlinear interactions over a broad spectrum of wavelengths. Such a technique is known as random quasi-phase matching (QPM) [120, 202, 203].

A good case in point is strontium barium niobate ($Sr_xBa_{1-x}Nb_2O_6$, SBN) crystal, which has been commonly used for broadband second harmonic generation (SHG) [80], cascaded third harmonic generation [84, 85], and even Cerenkov-type nonlinear interactions [73, 86]. However, the phase transition temperature (Curie temperature, T_c) of the SBN crystal is low [204], which is a main drawback for laser applications. At high pump power, the crystal will undergo a transition to the paraelectric state, and consequently, the quadratic nonlinear optical effects will disappear [205]. Compared with SBN, calcium barium-niobate ($Ca_xBa_{1-x}Nb_2O_6$, CBN) crystal is more suitable for practical optical devices operating at higher pump powers because of its

higher phase transition temperature. For example, the CBN crystal exhibits a transition temperature of about 539 K for the congruently melting composition with 28 mol. % of calcium (x = 0.28, CBN-28) [206, 207], but the SBN crystal shows a lower transition temperature of about 353 K for the congruently melting composition with 61 mol. % of strontium content (x = 0.61, SBN-61) [76, 208]. Recently, Cerenkov-type SHG has been demonstrated in the CBN-28 crystal, which can be used as a nonlinear prism [209-211].

In this chapter, we show that the CBN crystal is superior over the traditional SBN crystal in terms of the frequency mixing process, which leads to a higher conversion efficiency. We demonstrate experimentally that the broadband SHG process in the CBN crystal is three to four times higher than that in the same size SBN crystal. We also analyze the polarization properties of the emitted radiation and determine the ratio of d_{32} and d_{33} components of the second-order susceptibility tensor of the CBN crystal.

4.2 Experimental setup

In experiments we used $Ca_{0.28}Ba_{0.72}Nb_2O_6$ (CBN-28) crystal grown at the Institute of Electronic Materials Technology, Warsaw, Poland by using the Czochralski technique. The dimensions of the sample were 5 mm × 5 mm for the transverse cross section (defined by the x–y crystallographic directions) and 4 mm in thickness (z). All surfaces of the crystal were polished. As a reference we used the same-sized $Sr_{0.61}Ba_{0.39}Nb_2O_6$ (SBN-61) crystal. To visualize ferroelectric domain structures inside these crystals, we employed the discussed earlier Cerenkov SH microscopy technique [172, 183]. Figure 4. 1 shows a typical x–z scan of the antiparallel ferroelectric domains inside the CBN-28 and SBN-61 crystals, respectively. It can be clearly seen that both crystals exhibited random-sized ferroelectric domain distributions, which makes them attractive for the phase matching of broadband nonlinear interactions.

To demonstrate the performance of the CBN-28 and SBN-61 crystals as broadband frequency converters, the SHG process was experimentally

studied. For the laser source we used an optical parametric amplifier (Palitra) pumped by 150 femtosecond laser pulses with a repetition rate of 1 kHz. The output beam, which passes through a half-wave plate, was then focused by a lens (15 cm focal length) so that the beam was incident at a normal angle onto the *yz* surface of the sample. The input polarization of the fundamental beam can be varied from ordinary to extraordinary by adjusting the half waveplate. A short-pass filter was used to separate the fundamental beam and its SH so their corresponding powers and spatial intensity distributions could be measured and recorded using a power meter and CCD camera, respectively. In addition, a polarizer enabled measurements of the ordinary and extraordinary components of the generated harmonic.

4.3 Experimental results

When the fundamental beam was launched into the CBN-28 crystal, the SH beam was readily observed. The image in Figure 4. 1 (c) depicts the spatial light intensity distribution of the harmonic beam (for an extraordinary polarized fundamental wave at 1.36 μm). Because the emission region was small (≈100's μm) compared to the crystal-screen distance, this image represents in fact the far field or spatial spectrum of the emitted wave. It can be clearly seen that the SH had a broad spatial distribution of the intensity in the transverse direction (*y*). This is a result of simultaneous phase matching of both collinear and noncollinear frequency doubling processes using different reciprocal vectors with continuously varied magnitudes and directions, as schematically shown by the phase-matching diagram in Figure 4. 1(d).

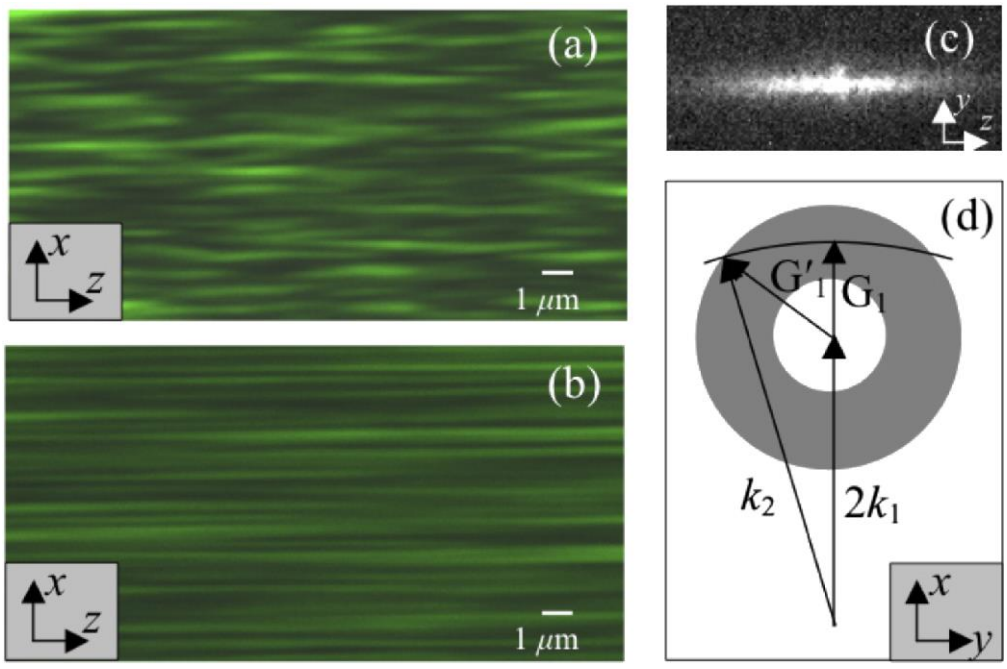

Figure 4. 1 Image of the random ferroelectric domain pattern in the *xz* plane of (a) CBN-28 and (b) SBN-61 crystal. These images were obtained by using Cerenkov SH microscopy. (c) Experimentally recorded transverse intensity distribution of the SH in the CBN-28 crystal. (d) Diagram of the phase matching for the SHG in the random CBN crystal. The grey disk represents the continuous distribution of reciprocal vectors in the crystal. Reciprocal vectors G_1 and G_{01} phase match the collinear and noncollinear SHG, respectively. k_1 and k_2 represent the wave vectors of the fundamental and SH waves, respectively.

In our experiment we tuned the fundamental wavelength continuously from 1.35 to 1.46 μm, and observed continuous generation of the corresponding SH signals. In Figure 4.2 (a) we depict the wavelength tuning curves of the SHG, i.e., the power of the emitted SH versus the fundamental wavelength with a constant input power of 2.0 mW. It can be seen that the SH power changes very weakly with the tuning of the fundamental wavelength, which is indicative of a homogenous Fourier spectrum of reciprocal lattice vectors in the CBN-28 crystal. In Figure 4. 2(b) we depict the output power of the SH signal generated in the CBN crystal with the fundamental beam at λ_1 =1.36 μm. We obtained an average power of 10 μW with a 4.9 mW input; the Fresnel reflections were accounted for. This corresponds to an internal conversion efficiency of 0.2%, and the SHG was demonstrated only in the fundamental wavelength range of 1.35-1.46 μm. The limitations of the

bandwidth were mainly given by the transparency window of the CBN-28 crystal, which covers the region 0.37-6.20 μm.

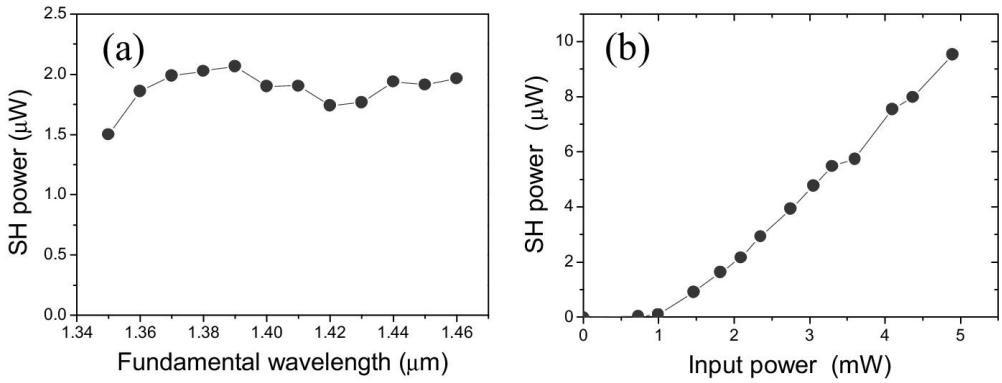

Figure 4. 2 (a) Wavelength tuning curve of the SHG in the CBN-28 crystal for a constant input power of 2.0 mW. (b) Power of the SHG as a function of the average power of the fundamental wave at 1.36 μm.

As a comparison we also measured the broadband SHG in the SBN crystal of the same size. The results are shown in Figure 4. 3. It can be seen, by comparing Figure 4. 2 and Figure 4. 3, that for most input wavelengths, the SH power generated in the SBN crystal was more than four times lower than that produced in the CBN crystal. Taking the SHG at the fundamental wavelength of 1.36 μm as an example, the conversion efficiency was about 0.05% at 4.9 mW of input in the SBN crystal, while it was 0.2% in the CBN crystal at the same input energy level. It is known that with assumptions of negligible pump depletion and weak focusing, the conversion efficiency of a quadratic process is proportional to the square of the effective nonlinear coefficient. Therefore, we may conclude that the effective nonlinear coefficient of the CBN-28 crystal was larger by at least a factor of 2 than that of the SBN-61 crystal, which includes not only the effect of the quadratic nonlinear coefficient of the material but also the effect of its spatial modulation in the QPM scheme.

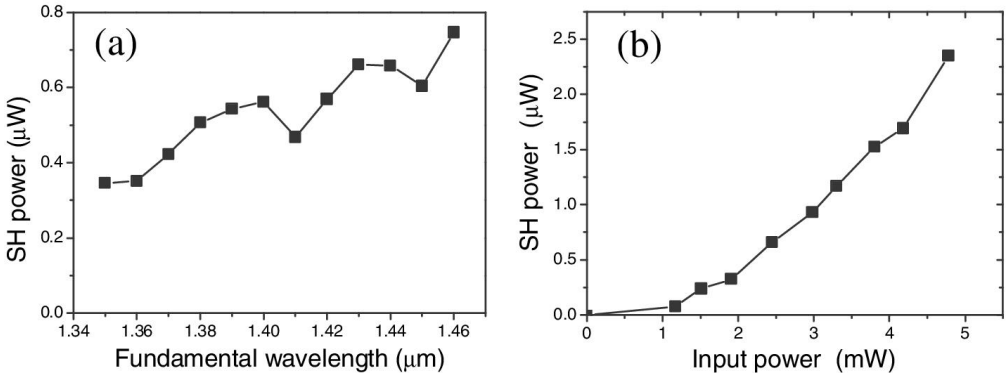

Figure 4. 3 (a) Wavelength tuning curve of the SHG in the SBN-61 crystal. (b) Power of the SHG as a function of the average power of the fundamental wave. The experiment parameters were the same as those used for the CBN-28 crystal.

Next, we studied the polarization properties of the emitted SHs from the random ferroelectric crystal. To this end, while the azimuthal angle of the linearly polarized fundamental wave was varied from zero to 360°, the powers of both ordinary and extraordinary components of the SH signals were measured. Interestingly, in our experiments the ordinary component of the SH was negligibly weak. Hence, the SH was always extraordinary polarized. Figure 4. 4 shows the power dependence of the extraordinary SHG in the CBN-28 and SBN-61 crystals. The experimental data are represented by dots and squares. Clearly, the strongest SH was recorded for the extraordinary fundamental wave. The solid curves in the graphs represent the theoretical predictions that were obtained by considering all possible processes that may contribute toward the generation of the SH.

We denote by O_j and E_j the ordinary and extraordinary components of the j-th wave (j = 1, 2 for the fundamental and SH, respectively). The extraordinary SH is formed via the following two processes: $E_1E_1 \rightarrow E_1$ and $O_1O_1 \rightarrow E_1$. The strength of each of these nonlinear processes is determined by the corresponding effective nonlinearity. In homogeneous media, all these processes contribute coherently to the total amplitude of the generated harmonic. However, because of the randomness in the domain distribution, this is no longer the case. As discussed earlier [212], the randomness in a nonlinear crystal leads to the incoherent buildup of generated waves. As a result, the two constituent processes in the SHG are mutually incoherent.

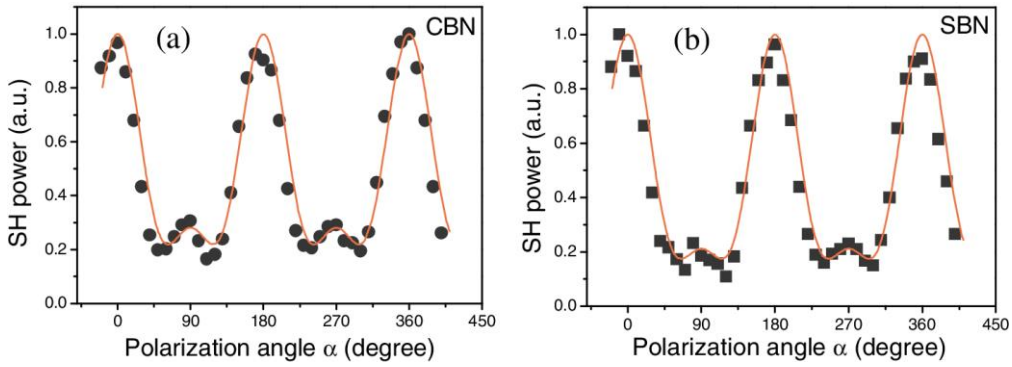

Figure 4. 4 Power of the extraordinary SH as a function of the input polarization angle of the fundamental beam in (a) CBN-28 and (b) SBN-61 crystals. 0° corresponds to the extraordinary fundamental wave. Points represent the experimental data; lines represent the theoretical fit using Eq. (4.1).

Hence, we can present the intensity of the extraordinary components of the SH by the following relation:

$$I_{(2\omega)}^{(e)} \propto I_{(\omega)}^{2}(\cos^4\alpha + R\sin^4\alpha), \qquad (4.\ 1)$$

where α represents polarization angle of the fundamental wave against the optical axis and R is the ratio of the nonlinear coefficient d_{32} to d_{33} in the crystal. Here, R is used as a free parameter in fitting Eq. (4. 1) to the experimental data, as shown in Figure 4. 4. We found that the best agreement between the experimental data and theory was achieved for R = 0.52 in the case of the CBN-28 crystal and R = 0.46 in the SBN-61 crystal. However, it should be noted that since the nonlinear optical properties of CBN and SBN crystals depend on their composition and ferroelectric domain structures, the parameter R is not a fixed quantity but will vary with the degree of nonstoichiometry and ferroelectric domain size.

4.4 Summary

In conclusion, we have studied broadband SHG in ferroelectric crystals with random-sized ferroelectric domains. We have demonstrated a higher conversion efficiency of broadband nonlinear interaction in the CBN-28 crystal compared to that of the commonly used SBN-61 crystal. We also analyzed the spatial distribution of the intensity of the generated radiation as

well as its polarization properties. Our experimental results can be easily generalized to other nonlinear parametric processes such as the difference frequency mixing and optical parametric oscillation. This study contributes to a simpler and more efficient realization of broadband frequency conversion devices in wide class of nonlinear optical media.

Chapter 5 Enhanced fourth harmonic generation in periodically poled lithium niobate

5.1 Introduction

Because of its relatively high efficiency, Cerenkov interaction is attractive for frequency conversion. In particular, one can utilize sum frequency mixing involving fundamental and Cerenkov beams to generate higher harmonics of the single fundamental beam [213-215]. Starting with long wavelength fundamental beam such cascading process of sum frequency mixing has generated up to fifth harmonic of the original input wavelength [37, 216]. Moreover, because of material dispersion each generated harmonic is emitted at different angle leading to the formation of the so-called nonlinear colour fan. The major drawback of this, and other transverse interaction schemes is the quick decrease of conversion efficiency with increased cascading order. Therefore, the power of higher harmonics becomes progressively the weaker. In contrast, phase matched collinear frequency generation in periodically poled structures ensures strong energy transfer between the fundamental and its second harmonic.

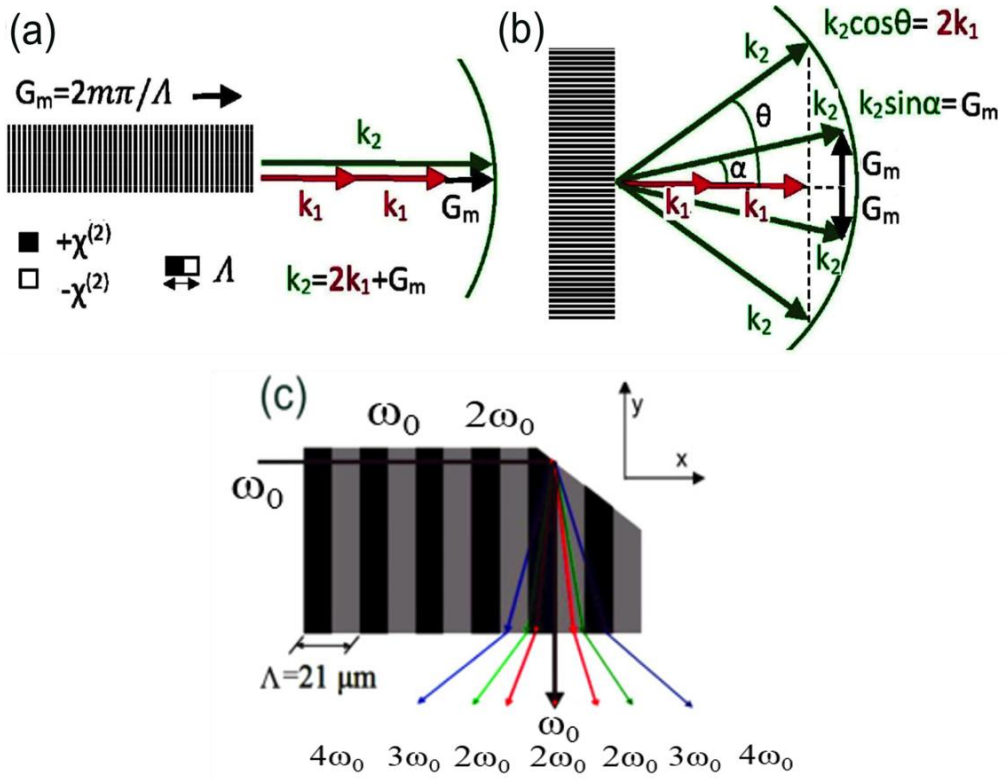

Figure 5. 1 Phase matching diagrams of (a) traditional collinear quasi-phase matched SHG and (b) transverse SHG. The arc represents the magnitude of the SH wave vector; α is the emission angle of m-th Raman-Nath SH wave, and θ is the Cerenkov SH emission angle that is determined solely by the longitudinal phase matching condition. (c) The geometry of multiple frequency mixing process that combines both, collinear and transverse types of interactions. Here the collinear SH generation is followed, after its total reflection at the 45° corner, by the Cerenkov second, third, and fourth harmonic generations.

In this chapter, we propose to combine traditional collinear QPM interaction with nonlinear Cerenkov frequency generation in a single sample of periodically poled nonlinear crystal. Our approach offers the advantages of both interaction mechanisms to achieve higher efficiency of high harmonic generation via $\chi^{(2)}$ cascading. As a proof of concept, we demonstrate enhanced fourth harmonic generation in a custom-cut periodically poled lithium niobate crystal.

5.2 Experimental design

The geometry of the proposed nonlinear optical interaction is schematically depicted in Figure 5. 1 (c). The rectangular shaped *z*-cut sample of

ferroelectric crystal (Lithium niobate, $LiNbO_3$) has one of its corners cut at 45°. The sample is periodically poled with period Λ along the, say, x axis. The fundamental beam (wavelength λ_0) propagates along the same axis until it is totally internally reflected at the 45° cut corner. After that the beam propagates along y-direction and finally leaves the sample. The nonlinear interaction in the crystal can be divided into two stages. Firstly, the input fundamental beam (FB) efficiently generates its second harmonic (SH) via quasi-phase matched collinear interaction using G_1 [Figure 5. 1 (a)]. To this end the poling period satisfies the following condition: $\Lambda = \lambda_0/2(n_{e2}-n_{e1})$, where n_{e1}, n_{e2} are extraordinary refractive indices of $LiNbO_3$ at the wavelengths of FB and SH, respectively. At the end of this collinear interaction both, FB and strong SH experience the total internal reflection, after which they propagate normally to the periodic $\chi^{(2)}$ modulation. During this second stage of propagation both beams serve as sources of transversely emitted higher harmonics as shown in Figure 5. 1 (c). Due to periodicity of the $\chi^{(2)}$ structure the transverse interaction involves both Raman-Nath and Cerenkov harmonic emissions. The effect of nonlinear Raman-Nath emission in sum frequency mixing has been discussed in detail in [216]. Since it is much weaker than the Cerenkov, we will neglect it in further discussions. Therefore, we are left with seven Cerenkov frequency conversion processes, schematically depicted in Figure 5. 2 (b-h) in terms of phase matching conditions. Here we do not consider Cerenkov SHG at the boundary between crystal and air in total internal reflection [212], which is expected to be much weaker than that caused by periodic $\chi^{(2)}$ modulation.

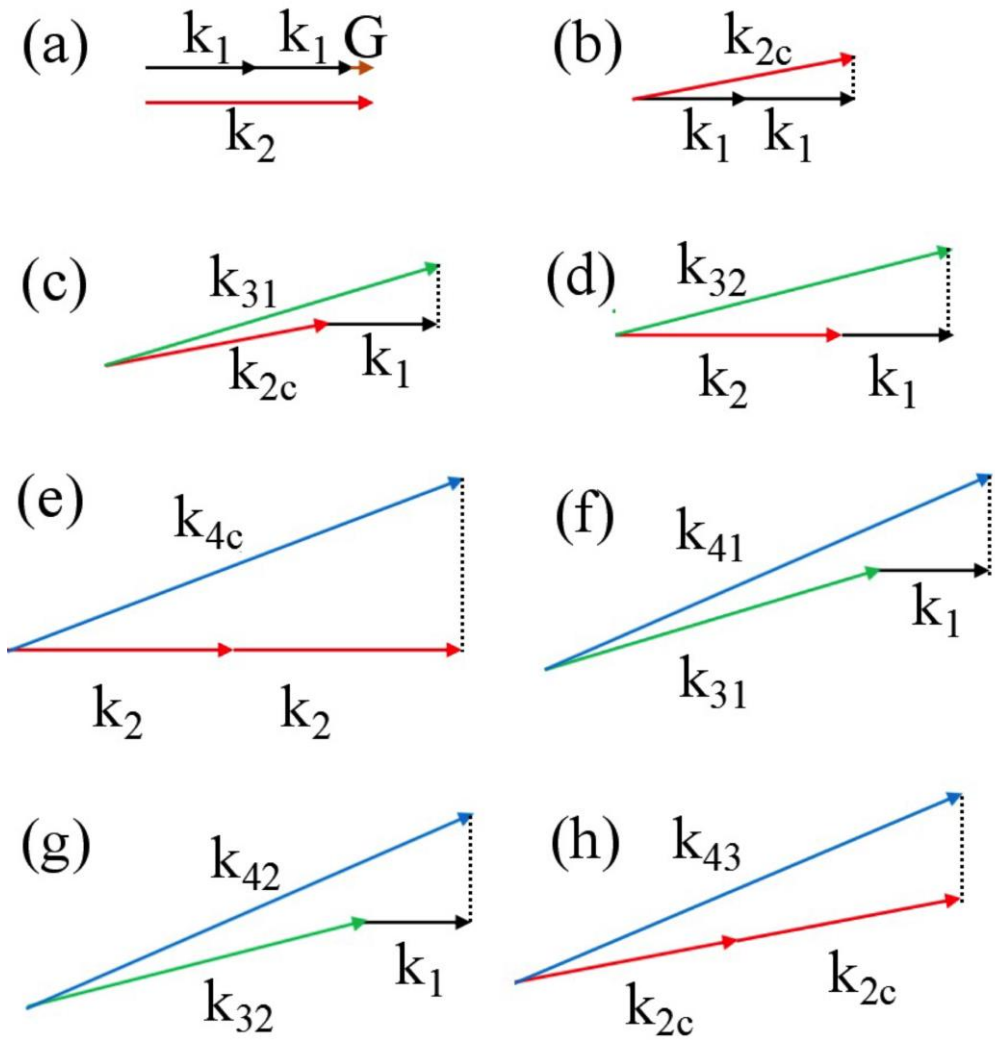

Figure 5. 2 Phase matching diagrams of frequency conversions in the customized structure. (a) Quasi-phase matched collinear SHG; (b) Cerenkov SHG; (c, d) Cerenkov THG via sum frequency mixing involving collinear and Cerenkov SH, respectively; (e, f) Cerenkov FHG via frequency doubling of collinear and Cerenkov SH, respectively; and (g, h) Cerenkov FHG via sum frequency mixing of the fundamental and different third harmonics.

Firstly, frequency doubling of collinear FB and SH results in appearance of Cerenkov second [Figure 5. 2(b)] and Cerenkov fourth [Figure 5. 2(e)] harmonics, with wave vectors k_{2c} and k_{4c}, respectively. The subsequent sum frequency mixing between FB and both, collinear SH and transverse Cerenkov SH leads to generations of two third harmonic waves with wave vectors k_{31} and k_{32}, respectively [see Figure 5. 2(c) and 2(d)]. There are three additional contributions to the forth harmonic generation. They include the wave formed via direct frequency doubling of Cerenkov second harmonic

(k_{41}) [Figure 5. 2(f)], and the other two formed via sum frequency mixing of the two third harmonics and the fundamental beam, denoted as k_{42} and k_{43} [Figure 5. 2(g) and 2(h)], respectively. Following the analysis above one can determine the emission angle for each harmonic. These angles along with the corresponding formulas, for which the Sellmeier equation of $LiNbO_3$ [217] was used, are listed in Table 5. 1. It is clearly seen that the emission angles of the Cerenkov harmonic waves depend only on the refractive indices of the material.

Table 5. 1 Internal emission angles of the Cerenkov harmonics.

Angles	$\cos\theta =$	Theoretical value	Measured value
θ_{2c}	$\frac{n_{e1}}{n_{e2}}$	10.84°	11.38°
θ_{31}	$\frac{n_{e1}+2n_{e2}}{3n_{e3}}$	14.31°	14.96°
θ_{32}	$\frac{n_{e1}}{n_{e3}}$	16.76°	16.75°
θ_{4c}	$\frac{n_{e2}}{n_{e4}}$	20.78°	21.26°
θ_{41}	$\frac{n_{e1}}{n_{e4}}$	23.33°	
θ_{42}	$\frac{n_{e1}}{n_{e4}}$	23.33°	
θ_{43}	$\frac{n_{e1}+n_{e2}}{2n_{e4}}$	22.09°	

5.3 Results and discussion

In the experiment we used a *z*-cut periodically poled lithium niobate crystal fabricated via electric-field poling technique. The sample's dimensions are 23 mm (*x*) ×7 mm (*y*) × 0.5 mm (*z*), respectively. The poling period was Λ = 21 μm with duty factor of 50% for the most efficient collinear second harmonic generation at fundamental wavelength of λ_0 = 1620 nm. One of the sample's corners was cut at 45° and the resulting plane was polished to ensure total internal reflection of both fundamental and SH beams. The 150 fs beam (25 nm bandwidth) from optical parametric amplifier (Coherent OPerA Solo, 1 kHz repetition rate) was first expanded and then loosely focused with the plano-convex lens (*f* = 500 mm) at the *x* facet of the crystal. The focal spot (roughly 100 μm wide) was located in the middle of the sample. With this width at least 5 periods of $\chi^{(2)}$ modulations were covered by the beam. The extraordinary input polarization ensured the strongest (*ee*-*e*) nonlinear interaction. The beam propagated through the sample for 20 mm along the *x*-direction until it was totally internally reflected at 45◦ surface and propagated along the *y*-direction (parallel to ferroelectric domain walls) for the next 5 mm, and finally left the sample. The emitted beams were projected onto the screen which was imaged with a CCD camera. The Glan prisms and half wave-plate were used to control the input beam power. To avoid material damage, the average input power was kept at a level of 150 μW.

On illuminating the sample with fundamental beam, we clearly observed a number of harmonic beams emitted from the *y*-surface of the sample as shown in Figure 5. 3. All beams were extraordinary polarized owing to the (*ee*-*e*) nonlinear interaction. The central spot represents both, fundamental and collinearly generated quasi-phase matched second harmonic. As the conversion efficiency of the collinear interaction reached 36%, both beams were of quite high intensity and had to be attenuated in order to make other beams visible on the CCD. The average power of the collinear SH was 55 μW. The bright, transversely emitted beams that are closest to the central spots are Cerenkov second harmonics (CSH) with an average power of 0.9 μW. Next, there is a pair of green spots representing third harmonic beams

(TH_1, TH_2) whose phase matching processes are depicted in Figure 5. 2 (c) and (d), respectively. Their combined power was 7.78 nW. These TH beams are significantly weaker than CSH. In fact, we could expect the beam TH_2 to be much weaker because it originates from the second cascading order of interaction. The beam TH_1 formed via sum frequency mixing of two strong beams, fundamental and collinear SH, and hence was expected to be relatively strong. Its low power is most likely caused by the use of short pulses (150 fs) in our experiments. In this regime the frequency conversion process is adversely affected by the group velocity mismatch between the fundamental and second harmonic pulses, which is estimated to be 0.27 ps/mm at 1620 nm for congruent $LiNbO_3$ crystal. The mismatch restricted the effective interaction distance. One may expect to achieve higher conversion efficiency for TH_1 by using longer (picosecond or nanosecond) pulses [198].

Finally, there is a pair of strong blue spots representing fourth harmonics of the fundamental wave. Its combined power was 57 nW. In the traditional scheme of cascading of nonlinear processes, the fourth harmonic should be much weaker than the third harmonics. This is not the case here since the major contribution to the FH comes from Cerenkov frequency doubling of the collinearly emitted SH. The order of this process is the same as Cerenkov SHG and hence the beam intensity is few times higher than the intensity of the third harmonic. Notice that the group velocity mismatch does not affect the Cerenkov fourth harmonic, as only the collinear second harmonic serves as the major source of the emission [see Figure 5. 2 (e)].

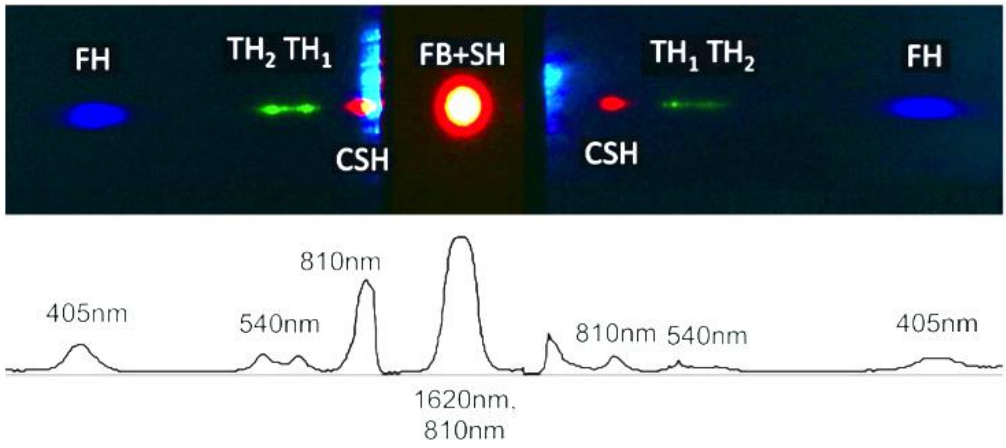

Figure 5. 3 Experimentally recorded angular distribution of multiple frequency signals. The central spot corresponds to overlapping fundamental and collinearly generated SH beams. The latter is shown using false red color. Due to large differences in the harmonic powers this is a composite picture with enhanced brightness and contrast of high harmonics. The vertical bright streaks around CSH beams are artefacts caused by scattering of the fundamental beam in the sample.

The measured internal emission angles for these harmonic beams, listed in Table 5.1, agree well with the theoretical values. Interestingly, we observed only one broad spot corresponding to the fourth harmonic generation. Therefore, the angle 21.26° refers to the maximum in the blue emission spot. Because of its 2.72° angular width, it most likely corresponds mainly to k_{4C} and k_{43} emission. The two other beams with wave-vectors k_{41} and k_{42} should be emitted at an angle close to the angle of total internal reflection. Therefore, these beams could be either trapped inside the sample or significantly attenuated due to the Fresnel reflection at the boundary. We attribute the small difference between measured and predicted emission angles to departure of the direction of fundamental beam from the ideal normal incidence inside the sample. While Cerenkov harmonic emission is always symmetric with respect to ferroelectric domain walls, any tilt of the fundamental beam (in the plane of the structure) leads to increased emission angle and angularly asymmetric emission with respect to the direction of fundamental beam [29]. From our measurements we estimated the angular tilt of the fundamental beam to be approximately 4°. The asymmetry of Cerenkov emission with respect to propagation direction of the fundamental beam, is clearly visible in Figure 5. 3 (a). Moreover, in agreement with theory

[31] the tilt of fundamental beam also causes asymmetric power distribution within the pair of Cerenkov beams, which is also evident in Figure 5. 3(a), where all beams propagating to the right of FB are stronger than their left counterparts. In fact, this property can be utilized in directing majority of emitted power into one set of Cerenkov beams.

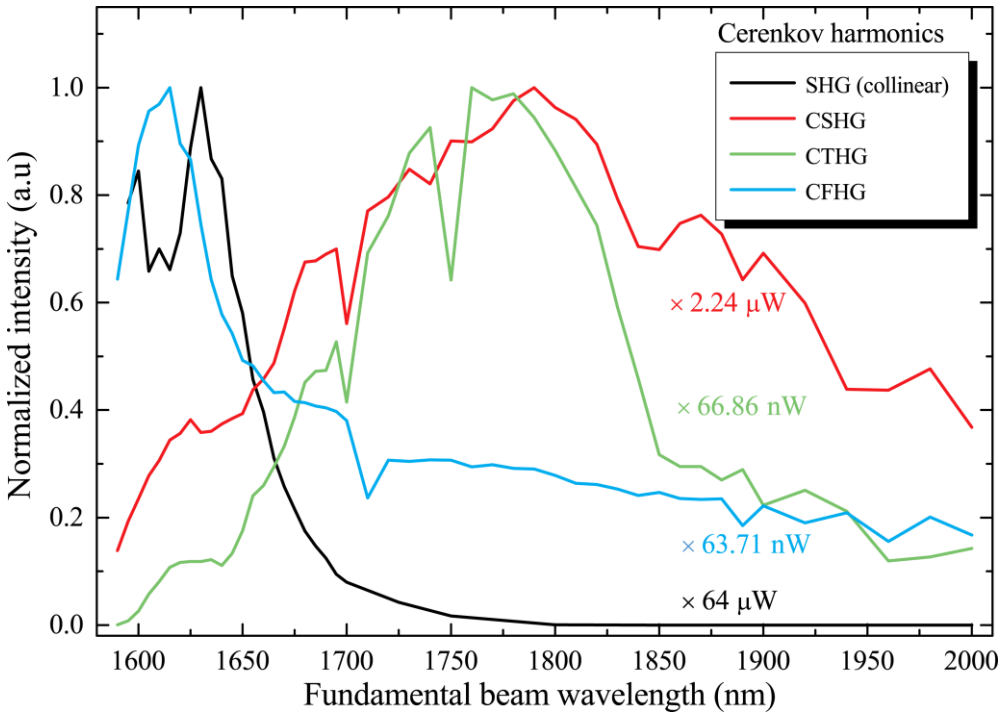

Figure 5. 4 Normalized intensity of the constituent harmonics as a function of the wavelength of fundamental beam. Numerical factors next to the plots represent the maximal power of each beam.

In Figure 5. 3 (b) we depict measured intensity of each emitted harmonics as a function of the wavelength of the fundamental beam. All curves are normalized to their maxima. It is clear that departure from the exact resonant wavelength (1620 nm) results in an immediate drop of the collinear SH and Cerenkov FH, indicating again that the collinear SH serves as the major emission source of the fourth harmonic generation [Figure 5. 2 (e)]. Note that the FH did not vanish even though the collinear SH became weak at longer wavelengths. This indicates the growing contributions to FH from the other phase matching processes, namely those involving the Cerenkov SHG [Figure 5. 2 (f-h)], which became stronger at longer wavelengths. The plot in Figure 5. 3 (b) also shows the nonmonotonic dependence of Cerenkov TH and SH on the fundamental wavelength. This

agrees with the fact that the Cerenkov frequency generation in a periodic structure strongly depends on the wavelength [182]. For certain wavelengths, both transverse and longitudinal phase matching conditions will be simultaneously satisfied, giving rise to the nonlinear Bragg diffraction which will enhance the Cerenkov emission [31]. In fact, the growth of CSH and CTH for longer wavelengths, seen in Figure 5. 3 (b) is very likely caused by this effect as we determined that Bragg resonances appear at 1680 nm and 1800 nm. The wavelength sensitivity could be weakened by incorporating weak disorder into the otherwise periodic domain pattern [181]. Moreover, the disorder could significantly broaden the bandwidth of our technique by easing the inherently narrow spectral response of collinear interaction [121]. Finally, the central frequency of our custom-cut ferroelectric crystal can be tuned by angular tilting of the incident fundamental beam. The tilting would also enhance the Cerenkov emission at angles corresponding to the Bragg nonlinear diffraction [31].

5.4 Summary

We studied multiple frequency generation via the nonlinear cascading process in nonlinear photonic structure. By employing the total internal reflection inside the sample, we combined quasi-phase matched collinear and Cerenkov nonlinear sum frequency mixing to realize enhanced fourth harmonic generation in a single periodically poled lithium niobate crystal.

Chapter 6 Nonlinear diffraction in orientation patterned Gallium Arsenide

6.1 Introduction

Over the past decade, significant progress has been achieved in functionalizing III-V semiconductors to emit, manage, and detect light for laser and photonic applications. Some III-V compounds, notably gallium arsenide (GaAs), gallium phosphide (GaP) and indium phosphide (InP), exhibit outstanding quadratic nonlinear optical properties due to their noncentrosymmetric zinc-blende (cubic) structure. The second-order nonlinear coefficients of GaAs $d_{14} = d_{25} = d_{36} = 150$ pm/V [218] are much greater than those of widely used nonlinear ferroelectric crystals, such as lithium niobate ($d_{33} = 27$ pm/V) and potassium titanium oxide phosphate ($d_{31} = 16.9$ pm/V). The ability of III-V semiconductors to efficiently mediate energy exchange between the interacting light waves makes them very attractive for parametric frequency conversion [219, 220]; terahertz generation [221]; quantum optical applications [222]; and ultrafast all-optical signal processing [223]. GaAs-based devices also benefit from the broad infrared transparency window of GaAs, which spans from 0.9 to 17 mm [218], and are, therefore, important for military and sensing applications [224]. Moreover, combining the second-order nonlinear effects with the existing mature GaAs-based platform significantly facilitates the integration of laser sources with modulators, amplifiers and photonic bandgap structures inside all-on-chip optoelectronic devices.

GaAs has a high quadratic nonlinearity, but lacks optical birefringence. As a result, phase matching, i.e. synchronisation of phases of the interacting waves to efficiently exchange energy, cannot be achieved by traditional

birefringence-based techniques. Many different approaches have been proposed to overcome this limitation [225, 226]. The most effective one seems to be QPM [12, 199] realised by periodic modulation of the second-order nonlinearity in orientation-patterned GaAs (OP-GaAs) crystals [220]. Spatial engineering of the orientation of an OP-GaAs crystal during its growth makes neighbouring regions have reversed crystallographic orientation and consequently the opposite sign of the second-order nonlinear coefficient $\chi^{(2)}$. It is noteworthy that different crystal orientations do not affect linear optical properties of the material.

So far, QPM in OP-GaAs has been employed to demonstrate a number of second-order nonlinear optical effects, including second harmonic generation (SHG) [219, 227]; cascaded third harmonic generation [228]; optical parametric amplification [229]; mid-infrared continuum generation [230]; and terahertz generation based on intracavity parametric down-conversion [231]. All these applications, however, rely on collinear light interaction, during which the participating waves propagate in the direction along which the $\chi^{(2)}$ nonlinearity is modulated, as shown in Figure 6. 1 (a). The periodic $\chi^{(2)}$ modulation is required to ensure QPM of the interacting waves via the introduction of a set of reciprocal lattice vectors, $\boldsymbol{G}_{\mathbf{m}}$. In the simplest case of collinear SHG, the QPM condition can be written as a scalar equation $k_2 - 2k_1 - G_m = 0$, where $k_1 = |\boldsymbol{k}_1|$ and $k_2 = |\boldsymbol{k}_2|$ are the absolute values of the wave vectors of the fundamental and second harmonic (SH) waves, respectively. The absolute value of a reciprocal lattice vector $G_m = |\boldsymbol{G}_{\mathbf{m}}|$ is given by $G_m = 2m\pi/\Lambda$, where Λ is the period of the $\chi^{(2)}$ modulation and m is an integer.

In this chapter, we demonstrate that second-order nonlinear interaction in orientation-patterned semiconductors can also be realised in a novel noncollinear (transverse) geometry. This phenomenon is analogous to the well-known linear diffraction of waves on a dielectric grating and is hence known as nonlinear diffraction (NLD) [25, 32, 114]. An example of NLD is a noncollinear SHG. In this scheme, the incident fundamental wave propagates in the direction normal to that along which the $\chi^{(2)}$ nonlinearity is modulated, and a diffraction-like pattern of SH light is generated. As shown in Figure 6.

1 (b)-1(d), three cases of noncollinear SHG can be distinguished. The first is Bragg SHG [25], which satisfies the full vectorial QPM condition $\boldsymbol{k}_2 - 2\boldsymbol{k}_1 - \boldsymbol{G}_m = 0$ [see Figure 6. 1 (b)]. The other two cases can be described by a partial QPM condition $\boldsymbol{k}_2 - 2\boldsymbol{k}_1 - \boldsymbol{G}_m - \Delta\boldsymbol{k}_{L(T)} = 0$ [32], where $\Delta\boldsymbol{k}_{L(T)}$ are the phase mismatches in the longitudinal and transverse directions, respectively. When $\Delta\boldsymbol{k}_T = 0$, the transverse QPM condition $k_2 \sin\theta + G_m = 0$ (θ is the nonlinear diffraction angle) is satisfied and Raman-Nath SHG can be observed even with a longitudinal phase mismatch $\Delta\boldsymbol{k}_L$ [see Figure 6. 1 (c)]. In a similar way, Cerenkov SHG (CSHG) becomes observable when the longitudinal QPM condition is fulfilled, i.e. $k_2 \cos\theta - 2k_1 = 0$ [see Figure 6. 1 (d)].

Such noncollinear interactions are of great interest because of their potential applications in all-optical signal processing. Firstly, they enable the generated wave to be emitted in a desired spatial direction, thus eliminating the necessity of filtering out the incident wave. Moreover, by combining different periodic structures it is possible to take advantage of different phase matching conditions responsible for different processes and realise, for instance, multiple frequency generation [232], higher order effects, such as third or fourth harmonic generation, as a result of cascading two lower order processes [37]. Furthermore, such transverse emission allows for the control of the transverse spatial distribution of the generated waves. For example, second harmonic generation in a form of Bessel or Airy beams have been demonstrated experimentally by illuminating a nonlinear crystal with a fundamental Gaussian beam [126]. Transverse frequency conversion has been also shown to be a convenient method to create entangled photons [233].

Moreover, as we demonstrate below the CSHG also occurs at a single boundary between oppositely oriented regions of OP-GaAs, which is similar to what occurs on the boundaries of ferroelectric domains [172, 180]. This effect enables three-dimensional (3D) visualisation of domain structure of the orientation-patterned semiconductors. Unlike traditional diagnostic techniques based on scanning electron microscopy or optical microscopy, which require cutting, polishing and etching of the samples, the Cerenkov-based technique is unique as it is nondestructive and enables one to characterise the QPM structure everywhere in the bulk of the sample.

6.2 Experimental setup

We used an OP-GaAs crystal grown by hydride vapour phase epitaxy (HVPE) [234, 235], the method of choice for achieving fast growth rates with excellent selectivity so as to produce thick OP-GaAs structures for QPM frequency conversions. The epitaxial growth on orientation patterned semiconductor crystals requires templates with modulated crystalline orientation, which constitute the seeds for the epitaxial regrowth. In a compound III-V semiconductor with the zinc-blende structure, such as GaAs, the reverse orientation is produced by exchanging atoms between the two sublattices, i.e. Ga and As, which is equivalent to a reversal of the IIIV bond stacking. The first stage of the sample fabrication is the template preparation. During this process two GaAs wafers with the [001] and [00-1] crystallographic orientations are firstly bonded and then the [00-1] side is lapped until only a thin layer of the [00-1] GaAs remains on the [001] wafer. After that the patterned template is etched to reveal the orientation-patterned gratings, whose period and duty cycle are defined by photolithography [235].

The second stage of the fabrication consists of the regrowth on the OP-GaAs template to obtain a thick OP-GaAs crystal required for bulk optical pumping. In order to optimise QPM the crystallographic orientations must be preserved all along the growth process and the duty cycle of the structure must be kept equal to that defined on the template. Atmospheric pressure HVPE [236] allows one to grow hundreds of micrometers of a high quality GaAs layer. The HVPE growth is mainly limited by the adsorption of the gaseous molecules onto the surface, decomposition of the adspecies and desorption processes. HVPE growth is highly orientation-selective as it depends on the intrinsic growth anisotropy of the crystal, which can be controlled by the growth temperature and the precursor gas composition [237].

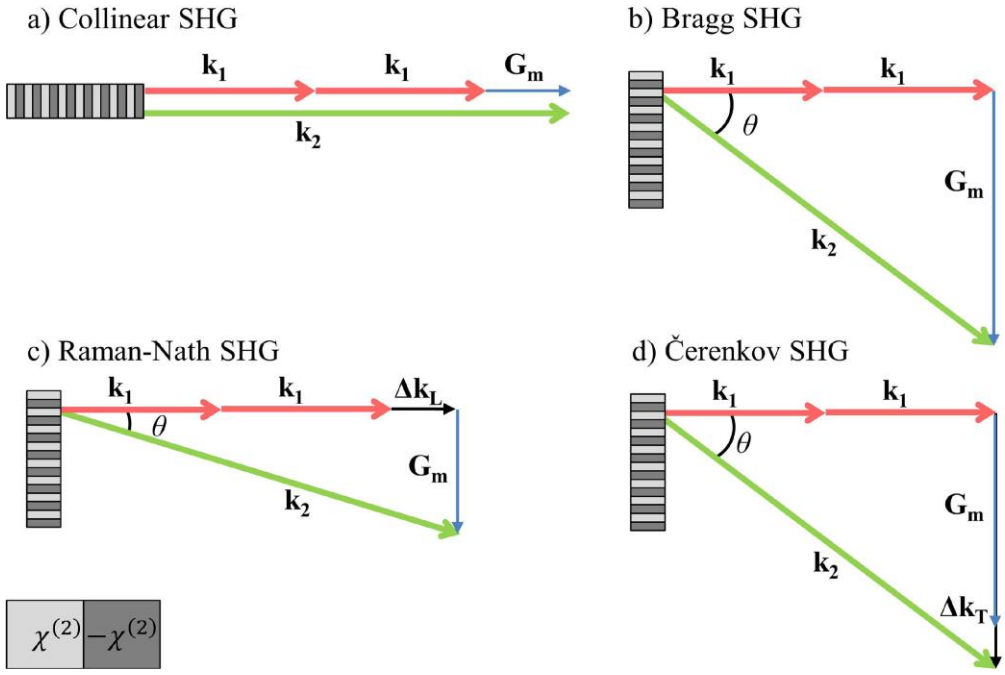

Figure 6. 1 Schematics of different types of SHG in OP-GaAs. (a) Traditional collinear SHG, (b) Bragg SHG satisfies the full vectorial quasi-phase matching condition, (c) Raman-Nath SHG satisfies only the transverse quasi-phase matching condition, and (d) Cerenkov SHG is defined by the longitudinal quasi-phase matching condition. $\boldsymbol{k}_1$ and $\boldsymbol{k}_2$ are the wave vectors of the fundamental and second harmonic waves, respectively, $\boldsymbol{G}_m$ is a reciprocal lattice vector and $\Delta\boldsymbol{k}_{L(T)}$ are the longitudinal and transverse phase mismatches, respectively.

An optical microscopy image of a chemically etched surface of the OP-GaAs crystal used in our studies is shown in Figure 6. 2. A periodic modulation of the crystal orientation with a period Λ = 64 μm and a 50% duty cycle is clearly visible. The thicknesses of the template and OP-GaAs layer were 300 μm and 500 μm, respectively. Before the nonlinear diffraction experiment, both top and bottom surfaces of the OP-GaAs crystal have been polished in order to avoid any effects from linear diffractions.

The experimental setup is shown in Figure 6. 3(a). As a light source we used an infrared (IR) femtosecond optical parametric amplifier (OPA) delivering 320 fs, 10 nJ pulses at a 21 MHz repetition rate. The central wavelength of the pulses was tunable from 2.9 to 4.0 μm [238]. The OP-GaAs sample was illuminated along the domain walls separating regions with positive and negative $\chi^{(2)}$ with loosely focused pulses from the OPA. The

focal spot inside the sample was approximately 300 μm in diameter and was large enough to cover 10 domain walls. The emitted SH signal was projected onto a ground silicon wafer which acted as a scattering screen and visualised with an InGaAs camera.

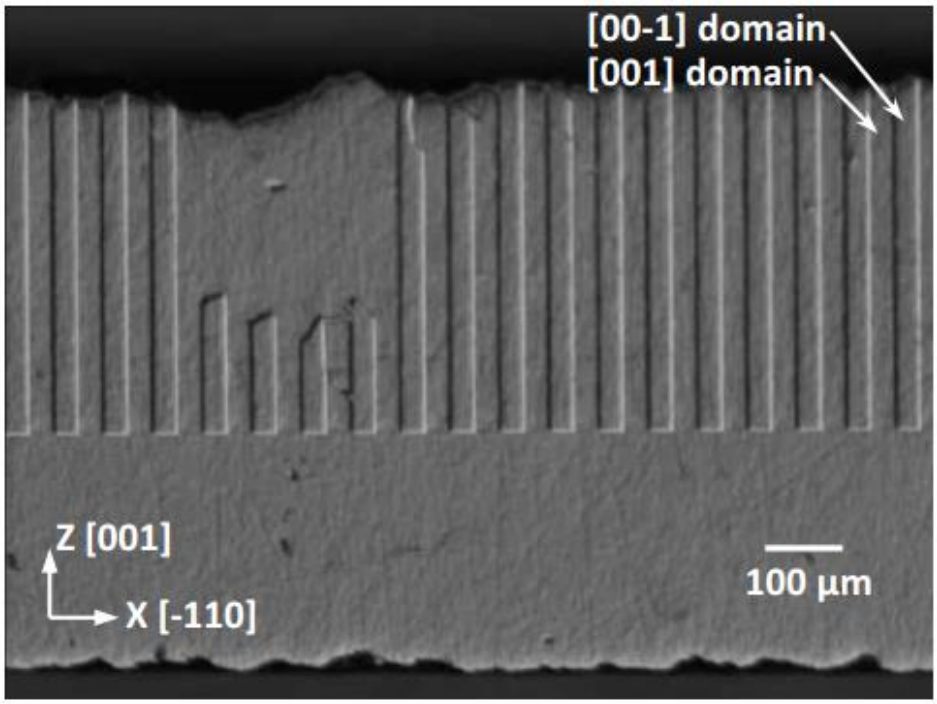

Figure 6. 2 Cross-sections of a 500 μm thick GaAs film grown on a OP-GaAs template of period Λ = 64 μm [183].

6.3 Results and discussion

During the NLD experiment we tuned the fundamental wavelength from 3.1 to 3.3 μm and recorded a NLD pattern at each wavelength. In Figure 6. 3 (a) we show a NLD pattern produced at a fundamental wavelength of 3.3 μm, which is representative of the whole frequency range investigated. The pattern consisted of (i) central diffraction spots, grouped around the fundamental beam position, and (ii) peripheral diffraction spots, located relatively far away from the central spots on both sides of the diffraction pattern (left and right spots on the screen in Figure 6. 3 (a)). The central diffraction spots included a collinear SH spot, which was observable only when the fundamental wave was focused at the OP-GaAs surface, and a pair of NLD spots, which were symmetric with respect to the collinear spot. The

measured external diffraction angle of the two NLD spots was ±1.5°. Figure 6. 3 (b) shows the normalised intensity of the peripheral NLD spots as a function of the fundamental wavelength λ and diffraction angle θ.

To explain the NLD pattern, we consider the intensity of SHG from a periodic $\chi^{(2)}$ structure, which can be written as [35, 239]:

$$I_{2\omega} \sim I_{\omega}^2 \times S_L^2 \times S_T^2, \qquad (6.\ 1)$$

where I_ω is the intensity of the fundamental beam inside the material and $S_{L(T)}$ are functions describing the longitudinal and transverse QPM conditions, respectively. The longitudinal QPM condition is satisfied when the function $S_L = \mathrm{sinc}\{z[(k_2\cos\theta)^2 - (2k_1)^2]/2\}$ approaches its maximum. In the above expressions, $\mathrm{sinc}(x) = \sin(x)/x$, and z is the interaction length. The SHG angle inside the sample satisfying this QPM condition is the Cerenkov angle:

$$\theta_c = \cos^{-1}\frac{n_1}{n_2}, \qquad (6.\ 2)$$

where n_1 and n_2 are the refractive indices of the medium at the fundamental and SH wavelengths, respectively. As in the previous case, the transverse QPM condition is defined by the maximum of the function $S_T = \sum_{m=0,\pm1,\pm2,\cdots} g_m e^{-w^2(k_2\sin\theta+G_m)^2/8}$, where w is the width of the fundamental beam and g_m are Fourier coefficients, which depend on the duty cycle of the $\chi^{(2)}$ nonlinear grating [35, 239]. The transverse QPM condition defines Raman-Nath angles $\theta_{RN,\,m}$ inside the sample:

$$\theta_{RN,\,m} = \sin^{-1}\frac{m\lambda}{2n_2\Lambda}, \qquad (6.\ 3)$$

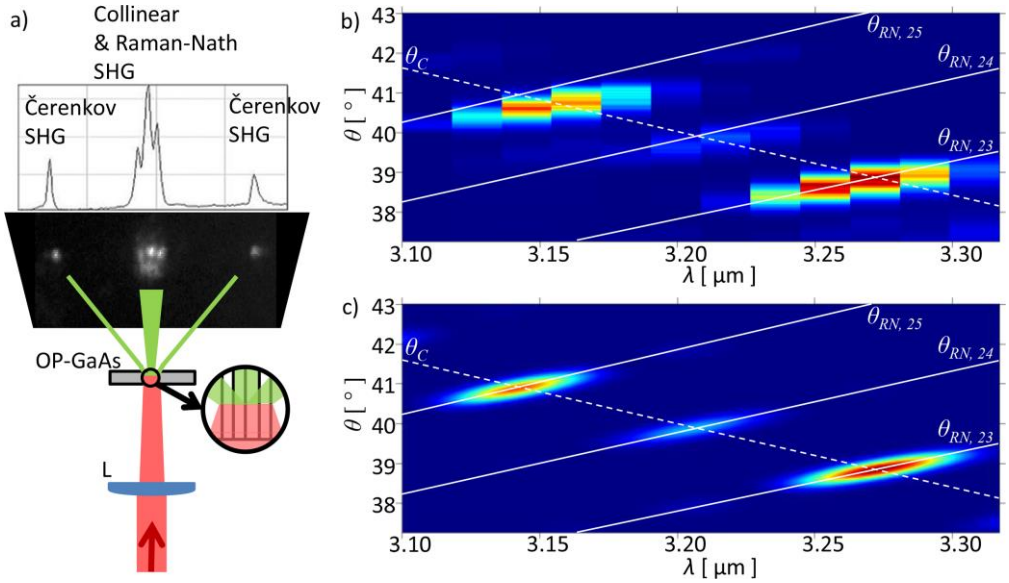

Figure 6. 3 (a) The experimental setup for observation of NLD. The incident laser beam is loosely focused with a lens (L, f = 150 mm) onto the OP-GaAs sample along the domain walls, which separate positive and negative $\chi^{(2)}$ domains. The closeup in the circle shows the focal spot, which covers multiple periods of the OP-GaAs. On the screen is shown the recorded nonlinear diffraction pattern at a fundamental wavelength of 3.3 μm together with the corresponding intensity profile. The experimentally measured (b) and modeled (c) intensity of the emitted SH signal as a function of the fundamental wavelength l and diffraction angle q outside the sample. In both cases the focal spot covers 10 domain walls. The solid lines represent Raman-Nath angles $\theta_{RN,\,m}$ for m = 23, 24 and 25 and the dashed lines represent the Cerenkov angle θ_C as a function of the fundamental wavelength.

Using the above equation, we calculated $\theta_{RN,\,1}$ = 1.5° for the first order of nonlinear R-NSHG outside the OP-GaAs with a period Λ = 64 μm, in agreement with the measured diffraction angle of the pair of SH spots in the central group. The refractive index of GaAs was calculated using the Sellmeier formula [240]. The intensities of the peripheral SH spots were calculated using Eq. (6. 1) and in Figure 6. 3 (c) the intensity of the peripheral diffraction spot $I_{2\omega}$ (λ, θ) is presented as a function of the fundamental wavelength and diffraction angle outside the sample. In Figure 6. 3 (b) and 3(c), the theoretical plots of the wavelength dependence of the Cerenkov angle θ_C (dashed lines) and Raman-Nath angles $\theta_{RN,\,m}$ (solid lines) outside the sample are produced using Eqs. (6. 2) and (6. 3), respectively.

It can be seen that the experimental results are in good agreement with the calculations. Importantly, the SH intensity gets much stronger when the Cerenkov angle θ_C becomes equal to a certain order of Raman-Nath angle $\theta_{RN,m}$. In fact, this is exactly the case of BSHG, when both the longitudinal and transverse QPM conditions are satisfied simultaneously. It can also be seen that the odd orders (m = 23, 25) of nonlinear diffraction are much more pronounced than the even order (m = 24). This is the direct consequence of an almost 50% duty cycle of the $\chi^{(2)}$ nonlinearity modulation, in which the regions with positive and negative nonlinear response have almost equal lengths [35, 239].

Here, we investigate SHG in OP-GaAs induced by a tightly focused fundamental beam, i.e. the beam whose width is much smaller than the period of the $\chi^{(2)}$ nonlinearity modulation. In this situation, the fundamental beam illuminates either a homogeneous region of the sample or the wall separating oppositely oriented domains. As we have shown recently [182], in this geometry only the Cerenkov SH signal is generated, which occurs when the fundamental beam illuminates a domain wall. No R-NSHG can be observed as it requires the participation of multiple grating periods.

The experimental setup is shown in Figure 6. 4 (a). The sample was mounted on a *xyz*-translation stage and could be scanned with a 60 nm resolution. We used the same OPA source as in Section 6. 2. The fundamental beam (λ = 3.5 μm) was chopped at 1 kHz and focused inside the sample using a molded chalcogenide lens with an effective NA = 0.3. The SH signal was collected with an IR-corrected objective with NA = 0.65. A spatial filter was used to block the surface-induced collinear SHG to ensure that only the Cerenkov SH signal was focused onto the InGaAs photodiode and processed using a lock-in amplifier.

In this configuration we measured the CSHG intensity as a function of the focal spot position inside the sample. Scanning at a constant velocity proceeded first along the *x* direction. The lock-in signal from the detector was triggered by the stage controller to synchronise the data acquisition process with the motion of the stage. In this way, we could achieve a 0.5 μm

resolution along the *x* axis. Scans along the *y* and *z* axes were performed at 2 and 20 μm resolution, respectively.

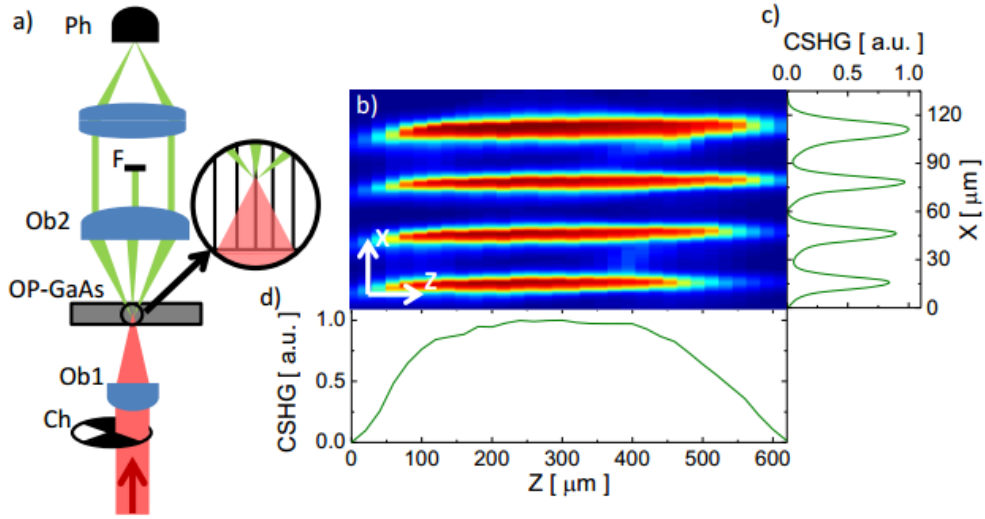

Figure 6. 4 (a) The experimental setup for observation of CSHG using a tightly focused fundamental beam: Ch - chopper, Ob1 - NA = 0.3 objective, Ob2 - NA = 0.65 objective, F - spatial filter, Ph - InGaAs photodiode. The inset shows the focusing configuration inside the OP-GaAs: the focal spot is much smaller than the period of the $\chi^{(2)}$ nonlinearity modulation. (b) The intensity of the emitted Cerenkov signal recorded by translating the sample in the *xz* plane. (c) and (d) show the Cerenkov intensity profiles along the *x* and *z* axes, respectively.

The resolution of the domain wall image is determined by both the resolution of the scanning system and the size of the OPA focus inside the sample. The focal radius w_0 of an incoming fundamental beam with a Gaussian intensity profile is given by $w_0 = \lambda/\pi\mathrm{NA}$ and in our case is estimated at 3.7 μm in the lateral, i.e. *xy*, plane. In the longitudinal, i.e. z, direction the size of the focus is determined by the Rayleigh length $z_R = (\pi n_1 w_0^2)/\lambda \approx 41$ μm. In addition, the resolution is also affected by spherical aberration caused by the high refractive index mismatch between the ambient air and the GaAs sample at both the fundamental and SH wavelengths.

Figure 6. 4(b) shows a two-dimensional intensity pattern of the Cerenkov SH signal in the *xz* plane. The colour change from blue to red reflects variation of the Cerenkov SH intensity from low to high. It can be seen that CSHG is very sensitive to the position of the focal spot with respect

to the domain walls. The maxima of the SH signal coincide with the locations of the domain walls in the OP-GaAs sample.

In Figure 6. 4(c), we plot a typical CSHG intensity profile along the *x* axis. The separation between the maxima is 32 mm, which is half of the $\chi^{(2)}$ nonlinearity modulation period Λ. This result confirms the 50% duty cycle. Figure 6. 4 (d) displays the CSHG intensity profile in the whole scanned region along the *z* direction. One can see that the strength of the CSHG remains almost constant inside the sample and decreases gradually at the ends of the sample. This is because the effective interaction length decreases when the focus of the fundamental beam moves out of the sample.

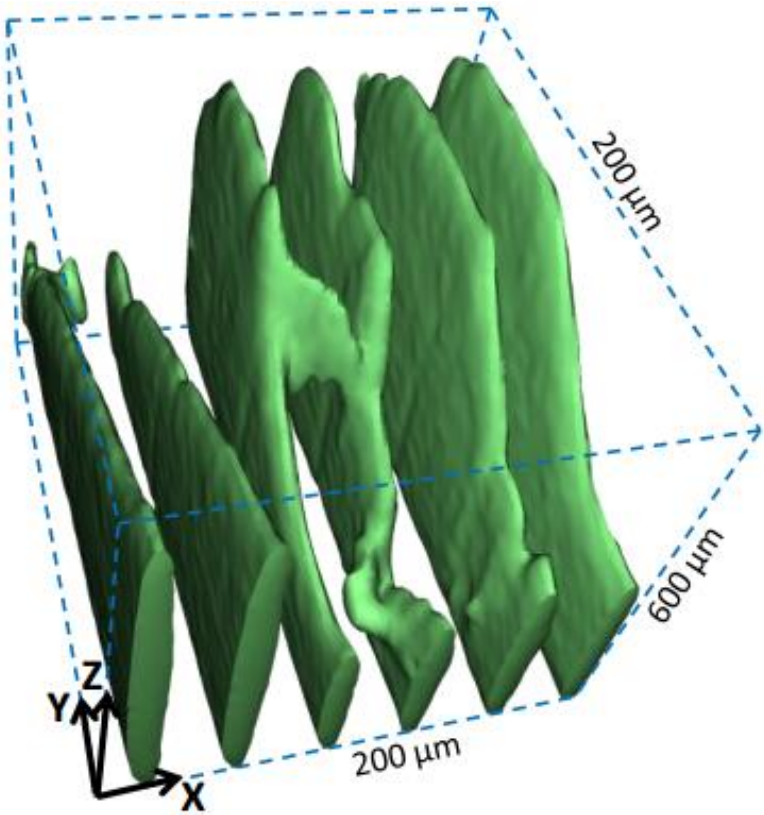

Figure 6. 5 A three-dimensional image of the OP-GaAs structure, obtained by scanning the fundamental beam inside the sample and recording the strength of the corresponding nonlinear Cerenkov diffraction at each position. The size of the box is $200 \times 200 \times 600\ \mu m^3$.

The sensitivity of CSHG to the presence of domain walls can be used to provide a contrast in scanning microscopy to visualise the domain structure of OP-GaAs in 3D. It should be stressed that, the demonstrated CSHG-based

scanning microscopy technique is totally non-destructive as it does not require any cutting or etching to reveal the bulk domain structure. In Figure 6. 5, we present a 3D image of the domain pattern inside the OP-GaAs sample. The image was created by stacking a number of *xy* scans recorded at different depths along Z axis. The box in the Figure 6. 5 represents the whole scanning volume 200 × 200 × 600 μm^3. It is clear that our CSHG-based microscopy technique allows us to not only reveal the nonlinear grating parameters such as the period and duty cycle, but also to determine the quality of orientation patterning in the bulk of a sample. For example, in Figure 6. 5 we show that the domain structure is nonuniform in the scanned region. In particular, the effect of merging of two neighbouring domains, which were initially separated, is evident.

6.4 Summary

We have presented the nonlinear diffraction in a OP-GaAs crystal. In particular, we have shown nonlinear Raman-Nath and Cerenkov second harmonic emission from a periodically modulated $\chi^{(2)}$ nonlinearity. We explain this effect by employing the concepts of longitudinal and transverse quasi-phase matching and show that the intensity of nonlinear diffraction is maximum, i.e. Bragg second harmonic generation, when these two conditions are satisfied simultaneously

We have also shown that Cerenkov second harmonic emission in the sample can be used to visualise the 3D structure of the $\chi^{(2)}$ nonlinearity modulation. Unlike traditional characterisation methods based on scanning electron microscopy or optical microscopy, which require cutting, polishing and etching of the samples, our technique is nondestructive and enables one to visualise the QPM structure everywhere in the bulk of the sample. This constitutes a unique nondestructive diagnostic tool for characterisation of orientation-patterned semiconductors and, potentially, any variations of the second-order nonlinearities in semiconducting materials.

Chapter 7 Conclusions and outlook

7.1 Outcomes

Quasi phase matching is a technique which enables efficient nonlinear interactions in nonlinear media. These nonlinear optical devices require proper structure design, material selection and ferroelectric domain engineering to realize specific functions. Although traditional electric field poling has been widely applied in various nonlinear media, it remains challenging to reliably invert domains below sizes of several microns. UV light can precisely produce submicron domain structures, but the very shallow depth has limited its practical applications.

This thesis can be divided into two parts. In the first part, a new optical poling method for fabricating ferroelectric domain structures has been proposed and demonstrated. Laser writing parameters for domain inversion were systematically investigated. Domain inversion in congruent lithium niobate crystals were realized using near-infrared femtosecond laser, without applying any external electric field. By moving the sample in three orthogonal directions, various two dimensional domain structures were fabricated. The minimal separation between neighbouring domains was as small as 1.5 μm, which was expected to be even smaller using objectives with higher numerical apertures. With the help of Cerenkov second harmonic microscopy, not only the optical induced domain inversion process can be monitored, but also the quality of the inverted domains can be characterized. It was found that the optically reversed domains can be as deep as 60 μm, which clearly surpasses the capability of the ultraviolet poling technique and can be applied in practical applications. As an experimental demonstration, a QPM structure in a $LiNbO_3$ channel waveguide was fabricated using this all optical poling technique. Comparing with the UV laser induced periodic

reduction of the nonlinearity, our all optical poling method utilized the highest modulation depth of nonlinearity from + $\chi^{(2)}$ to - $\chi^{(2)}$, eliminating unnecessary propagation loss for interacting waves. Doubling frequency of a 815 nm light was realized with a conversion efficiency of 17.45%. This study has demonstrated that this all optical poling method is a powerful technique which enables precise and flexible domain engineering for various applications.

In the second part, nonlinear interactions in some new structures and materials have been investigated. The first one is an initially rectangular shaped periodically poled lithium niobate crystal, which has one of its corners cut at 45°. This custom cut crystal enables combination of collinear second harmonic generation and transverse sum frequency mixing via the total internal reflection of the fundamental and collinear second harmonic beams. Multistep cascading frequency conversion processes in this crystal were investigated. With illuminating of a 1620 nm fundamental beam, apart from the Cerenkov SHG, two sets of Cerenkov THGs and Cerenkov FHG were clearly observed. It was also found that enhanced Cerenkov FHG was realized in this single periodically poled lithium niobate crystal.

The second research topic is using as-grown calcium barium niobate crystal in broadband frequency conversion. Normally, strontium barium niobate crystal are used for broadband harmonic generations, but the low phase transition temperature limits its application in high pump power lasers. In this study, it has been demonstrated that CBN crystal with 28 mol. % of calcium has better performance in broadband frequency conversion, due to its much higher phase transition temperature and larger nonlinearity comparing with strontium barium niobate crystal. In addition, the spatial distribution of the intensity of the generated radiation as well as its polarization properties were investigated.

Finally, nonlinear diffraction in an orientation-patterned semiconducting material has been experimentally demonstrated. Orientation patterned gallium arsenide grown by hydride vapour phase epitaxy was utlized for a new transverse geometry of interaction. Specifically, nonlinear Cerenkov

diffraction is defined by the longitudinal quasi-phase matching condition, nonlinear Raman-Nath diffraction satisfies only the transverse quasi-phase matching condition, and nonlinear Bragg diffraction fulfills the full vectorial quasi-phase matching conditions. In this study, the concept of transverse nonlinear parametric interaction has been extended toward infrared frequency conversion in semiconductors. It has also been demonstrated that Cerenkov second harmonic microscopy is an effective nondestructive method for visualising and diagnosing variations of second-order nonlinear coefficients inside semiconductors.

7.2 Outlook and future work

The highlight of this thesis is the demonstration of an all optical poling method, which has been used to fabricate quasi phase matching structure for efficient second harmonic generation. The future investigations of this all optical poling method can be carried out on two aspects, namely further optimizing the laser writing parameters and extending its application area.

Although considerable progress has been made in the quality of optical poled domains comparing with the UV poling technique, the depth of these reversed domains is still tens of micrometres, which limits its application in bulk crystals. Systematically investigation the parameters in laser writing is necessary, not only for better understanding of the physical mechanism, but also for finding optimal laser writing conditions for fabricating deeper domains. These parameters include wavelength, pulse duration, repetition rate, power, polarization of the laser and also the parameters of beam moving. In addition, spatial modulation of the laser beam may also be helpful for fabricating deeper domain structures. It has been reported that the spherical aberration caused by the refractive index mismatch can be corrected by using a liquid crystal spatial light modulator [191]. The size of the written structures after correction decreases dramatically, and the fabrication depth increases by a factor of two to three. This method allows one to fabricate high quality domain structures and maybe even three dimensional nonlinear photonic crystals.

Up to now, our all optical poling method has been applied predominantly to *z*-cut congruent lithium niobate crystals and waveguides. An immediate future direction is to extend this method to thin film lithium niobate, other cuts and compositions of lithium niobate such as MgO doped and SLN, and even other ferroelectric crystals such as lithium tantalate, KTP, SBN and CBN. In fact, our very recent experiments with CBN and BCT ($Ba_{0.77}Ca_{0.23}TiO_3$) crystals indicate applicability of the all-optical poling method to these media as well. Although electric field poling is feasible for many of these materials, most of the time cumbersome design of electrode pattern is required. If our all optical poling method is capable of inverting domains in more kinds of materials, it can be combined with other techniques such as direct laser writing of waveguides, making all optical engineered nonlinear photonic crystals achievable for a variety of applications.

References

[1] L. Schawlow, and C. H. Townes. Infrared and Optical Masers. Physical Review, Vol. 112, pp. 1940-1949, 1958.

[2] T. H. Mainman. Stimulated Optical Radiation in Ruby. Nature, 189 (1960), 493.

[3] P. A. Franken, A. E. Hill, C. W. Peters, and G. Weinreich. Generation of Optical Harmonics. Physical Review Letters, Vol. 7, pp. 118, 1961.

[4] M. Bass, P. A. Franken, A. E. Hill, C. W. Peters, and G. Weinreich. Optical Mixing. Physical Review Letters, Vol. 8, Iss. 1, pp. 18, 1962.

[5] R. C. Miller, and A. Savage. Harmonic Generation and Mixing of $CaWO_4$: Nd^{3+} and Ruby Pulsed Laser Beams in Piezoelectric Crystals. Physical Review, Vol. 128, Iss. 5, pp. 2175-2179, 1962.

[6] A. W. Smith, and N. Braslau. Observation of an Optical Difference Frequency. Journal of Applied Physics, Vol. 34, Iss. 7, pp. 2105-2106, 1963.

[7] C. C. Wang, and G. W. Racette. Measurement of Parametric Gain Accompanying Optical Difference Frequency Generation. Applied Physics Letters, Vol. 6, Iss. 10, pp. 213, 1965.

[8] J. A. Giordmaine, and R. C. Miller. Tunable Coherent Parametric Oscillation in $LiNbO_3$ at Optical Frequencies. Physical Review Letters, Vol. 14, Iss. 24, pp. 973–976, 1965.

[9] Y. H. Pao, and P. M. Rentzepis. The Journal of Chemical Physics, Vol. 43, pp. 1281, 1965.

[10] M. J. Hercher. Laser-induced damage in transparent media. Journal of the Optical Society of America, Vol. 54, Iss. 4, pp. 563, 1964.

[11] R. W. Hellwarth. Theory of stimulated Raman scattering. Physical Review, Vol. 130, Iss. 5, pp.1850, 1963.

[12] J. A. Armstrong, N. Bloembergen, J. Ducuing, and P. S. Pershan. Interactions between light waves in a nonlinear dielectric. Physical Review, Vol. 127, Iss. 6, pp. 1918-1939, 1962.

[13] D. A. Kleinman. Nonlinear Dielectric Polarization in Optical Media. Physical Review, Vol. 126, Iss. 6, pp. 1977-1979, 1962.

[14] J. E. Midwinter and J. Warner. The effects of phase matching method and of uniaxial crystal symmetry on the polar distribution of second-order nonlinear optical polarization. British Journal of Applied Physics, Vol. 16, Iss. 8, pp. 1135, 1965.

[15] P. A. Franken and J. F. Ward. Optical harmonics and nonlinear phenomena. Reviews of Modern Physics, Vol. 35, Iss. 1, pp. 23-39, 1963.

[16] P. D. Maker, R. W. Terhune, M. Nisenoff, and C. M. Savage. Effects of dispersion and focusing on the production of optical harmonics. Physical Review Letters, Vol. 8, Iss. 1, pp. 21-23, 1962.

[17] N. Bloembergen. Nonlinear Optics. Benjamin, New York, 1964.

[18] R. B. Miles, and S. E. Harris. Optical third-harmonic generation in alkali metal vapors. IEEE Journal of Quantum Electronics. Vol. 9, pp. 470, 1973.

[19] J. A. Giordmaine. Mixing of light beams in crystals. Physical Review Letters, Vol. 8, Iss. 1, pp. 19-21, 1962.

[20] A. Akmanov, S. Akhmanov, R. Khokhlov, A. Kovrigin, A. Piskarskos, and A. P. Sukhorukov. Parametric interactions in optics and tunable light oscillators. IEEE Journal of Quantum Electronics, Vol. 4, Iss. 11, pp. 828-831, 1968.

[21] R. Danielius, A. Piskarskas, P. Di Trapani, A. Andreoni, C. Solcia, and P. Foggi. Matching of group velocities by spatial walk-off in collinear three-wave interaction with tilted pulses. Optics Letters, Vol. 21, No.13, pp. 973, 1996.

[22] D. N. Nikogosyan. Properties of Optical and Laser-related Materials, Wiley, New York, 1997.

[23] B. Jaskorzynska, G. Arvidson and F. Laurell. Periodic structures for phase-matching in second harmonic generation in titanium lithium niobate waveguides. Proc. SPIE Vol. 651, pp.221, 1986.

[24] C. L. Tang, P. B. Bey. Phase matching in second harmonic generation using artificial periodic structures. IEEE J. Quantum Electron. QE-9, 9, 1973.

[25] I. Freund. Nonlinear diffraction. Physical Review Letters. Vol. 21, Iss. 19, pp. 1404, 1968.

[26] D. A. Kleinman. Theory of Second Harmonic Generation of Light. Physical Review, Vol. 128, Iss. 4, pp. 1761-1775, 1962.

[27] A. Zembrod, H. Puell, and J. A. Giordmaine. Surface radiation from nonlinear optical polarization. IEEE Journal of Quantum Electronics, Vol. 4, Iss. 5, pp. 396, 1968.

[28] S. M. Saltiel, Y. Sheng, N. Voloch-Bloch, D. N. Neshev, W. Krolikowski, A. Arie, K. Koynov, and Y. S. Kivshar. Cerenkov-type second harmonic generation in two dimensional nonlinear photonic structures. IEEE Journal of Quantum Electronics, Vol. 45, pp. 1465-1472, 2009.

[29] S. M. Saltiel, D. N. Neshev, W. Krolikowski, A. Arie, O. Bang, and Y. S. Kivshar. Multi-order nonlinear diffraction in frequency doubling processes. Optics Letters, Vol. 34, Iss. 6, pp. 848-850, March 2009.

[30] W. H. Bragg, and W. L. Bragg. The Reflection of X-Rays by Crystals. Proceedings of the Royal Society of London. Series A, 88, pp. 428, 1913.

[31] K. Kalinowski, P. Roedig, Y. Sheng, M. Ayoub, J. Imbrock, C. Denz, and W. Krolikowski. Enhanced Cerenkov second-harmonic emission in nonlinear photonic structures. Optics Letters, Vol. 37, Iss. 11, pp. 1832, 2012.

[32] A. Shapira, and A. Arie. Phase-matched nonlinear diffraction. Optics Letters, Vol. 36, Iss. 10, pp. 1933-1935, 2011.

[33] C. D. Chen, Y. Zhang, G. Zhao, X. P. Hu, P. Xu, and S. N. Zhu. Experimental realization of Cerenkov up-conversions in a 2D nonlinear photonic crystal. Journal of Physics D: Applied Physics, Vol. 45, Iss. 40, pp. 405101, 2012.

[34] K. Kalinowski, V. Roppo, T. Lukasiewicz, M. Swirkowicz, Y. Sheng, and W. Krolikowski. Parametric wave interaction in one-dimensional nonlinear photonic crystal with randomized

distribution of second-order nonlinearity. Applied Physics B, Vol. 109, Iss. 4, pp. 557-566, 2012.

[35] Y. Sheng, Q. Kong, V. Roppo, K. Kalinowski, Q. Wang, C. Cojocaru, and W. Krolikowski. Theoretical study of Cerenkov-type second-harmonic generation in periodically poled ferroelectric crystals. Journal of the Optical Society of America B, Vol. 29, Iss. 3, pp. 312, 2012.

[36] H. X. Li, S. Y. Mu, P. Xu, M. L. Zhong, C. D. Chen, X. P. Hu, W. N. Cui, and S. N. Zhu. Multicolor Cerenkov conical beams generation by cascaded-$\chi^{(2)}$ processes in radially poled nonlinear photonic crystals. Applied Physics Letters, Vol. 100, Iss. 10, pp. 101101, 2012.

[37] N. An, H. Ren, Y. Zheng, X. Deng, and X. Chen. Cherenkov high-order harmonic generation by multistep cascading in $\chi^{(2)}$ nonlinear photonic crystal. Applied Physics Letters, Vol. 100, Iss. 22, pp. 221103, 2012.

[38] C. D. Chen, X. P. Hu, Y. L. Xu, P. Xu, G. Zhao, and S. N. Zhu. Cerenkov difference frequency generation in a two-dimensional nonlinear photonic crystal. Applied Physics Letters, Vol. 101, Iss. 7, pp. 071113, 2012.

[39] L. V. Simagina, E. D. Mishina, S. V. Semin, N. A. Ilyin, T. R. Volk, R. V. Gainutdinov, and L. I. Ivleva. Second harmonic generation in microdomain gratings fabricated in strontium-barium niobate crystals with an atomic force microscope. Journal of Applied Physics, Vol. 110, Iss. 5, pp. 052015, 2011.

[40] Y. Sheng, W. Wang, R. Shiloh, V. Roppo, A. Arie, and W. Krolikowski. Third-harmonic generation via nonlinear Raman-Nath diffraction in nonlinear photonic crystal. Optics letters, Vol. 36, Iss. 16, pp. 3266, 2011.

[41] M. S. Piltch, C. D. Cantrell, and R. C. Sze. Infrared second-harmonic generation in nonbirefringent cadmium telluride. Journal of Applied Physics, Vol. 47, pp. 3514-3517, 1976.

[42] A. Szilagyi, A. Hordvik, and H. Schlossberg. A quasi-phase-matching technique for efficient optical mixing and frequency doubling. Journal of Applied Physics, Vol. 47, pp. 2025-2032, 1976.

[43] D. E. Thompson, J. D. McMullen, and D. B. Anderson. Second-harmonic generation in GaAs "stack of plates" using high power CO_2 laser radiation. Applied Physics Letters, Vol. 29, pp. 113-115, 1976.

[44] M. Okada, K. Takizawa, and S. Ieiri. Second harmonic generation by periodic laminar structure of nonlinear optical crystal. Optics Communications, Vol. 18, pp. 331-334, 1976.

[45] G. G. Gurzadian, V. G. Dmitriev, and D. N. Nikogosian. Handbook of nonlinear optical crystals. 3rd edition, Springer Series in Optical Sciences, Springer-Verlag, New York, 1999.

[46] O. F. Schirmer, O. Thiemann and M. Wöhlecke. Defects in $LiNbO_3$—I. experimental aspects. Journal of Physics and Chemistry of Solids, Vol. 52, Issue 1, pp. 185-200, 1991.

[47] S. C. Abrahams and C. Florea. Stoichiometry, defect structure and composition of $LiNbO_3$. In K. K. Wong (editor), Properties of

Lithium Niobate, EMIS data reviews series, 3-7, INSPEC, London, 2002.

[48] S. Sanna and W. Gero Schmidt. Ferroelectric Phase Transition in $LiNbO_3$: Insights From Molecular Dynamics, IEEE Transactions on Ultrasonics, Ferroelectrics and Frequency control. Vol. 59, Issue 9, pp. 1925-1928, 2012.

[49] R. W. Boyd. Nonlinear Optics. 3rd edition, Academic, 2008.

[50] K. K. Wong. Properties of Lithium Niobate. IEE Datareview series, IET, 2002.

[51] A. M. Prokhorov. Physics and Chemistry of Crystalline Lithium Niobate. Inst of Physics Pub Inc, 1990.

[52] I. U. S. Kuz'minov. Lithium Niobate Crystals. Cambridge International Science Publishing, 1999.

[53] R. S. Weis and T. K. Gaylord. Lithium niobate: Summary of physical properties and crystal structure. Applied Physics A: Materials Science & Processing, Vol. 37, Iss. 4, pp. 191-203, 1985.

[54] G. Zhong, J. Jian, and Z. Wu. Measurement of optically induced refractive-index change of lithium niobate doped with different concentration of MgO. In Proceedings of the 11th International Quantum Electronics Conference, pp. 631-635, 1980.

[55] A. Kuroda, S. Kurimura, and Y. Uesu. Domain inversion in ferroelectric MgO: $LiNbO_3$ by applying electric fields. Applied Physics Letters, Vol. 69, pp. 1565-1567, 1996.

[56] H. Ishizuki, I. Shoji, and T. Taira. Periodical poling characteristics of congruent MgO: $LiNbO_3$ crystals at elevated temperature. Applied Physics Letters, Vol. 82, pp. 4062-4064, 2003.

[57] T. Sugita, K.Mizuuchi, Y.Kitaoka, and K. Yamamoto. Ultraviolet light generation in a periodically poled MgO: $LiNbO_3$ waveguide. Japanese Journal of Applied Physics, Vol. 40, pp. 1751-1753, 2001.

[58] H. Ishizuki, T. Taira, S. Kurimura, J. H. Ro, and M. Cha. Periodic poling in 3-mm-thick MgO: $LiNbO_3$ crystals. Japanese Journal of Applied Physics, Vol. 42, pp. L108-L110, 2003.

[59] H. Ishizuki and T. Taira. High-energy quasi-phase-matched optical parametric oscillation in a periodically poled MgO: $LiNbO_3$ device with a 5 mm × 5 mm aperture. Optics Letters, Vol. 30, pp. 2918-2920, 2005.

[60] H. Ishizuki and T. Taira. High energy quasi-phase matched optical parametric oscillation using Mg-doped congruent $LiTaO_3$ crystal. Optics Express, Vol. 18, pp. 253-258, 2010.

[61] H. Ishizuki and T. Taira. Half-joule output optical-parametric oscillation by using 10-mm-thick periodically poled Mg-doped congruent $LiNbO_3$. Optics Express, Vol. 20, pp. 20002-20010, 2012.

[62] H. Karlsson, and F. Laurell. Electric field poling of flux grown $KTiOPO_4$. Applied Physics Letters, Vol. 71, Iss. 24, pp. 3474-3476, 1997.

[63] H. Karlsson, F. Laurell, and L. K. Cheng. Periodic poling of $RbTiOPO_4$ for quasi-phase matched blue light generation. Applied Physics Letters, Vol. 74, Iss. 11, pp. 1519-1521, 1999.

[64] V. Pasiskevicius, S. Wang, J. A. Tellefsen, F. Laurell, and H. Karlsson. Efficient Nd: YAG laser frequency doubling with periodically poled KTP. Applied Optics, Vol. 37, Iss. 30, pp. 7116-7119, 1998.

[65] G. Rosenmandag, A. Skliardag, Y. Findlingdag, P. Urenskidag, A. Englanderddag, P. A. Thomas and Z. W. Hu. periodically poled $KTiOAsO_4$ crystals for optical parametric oscillation. Journal of Physics D: Applied Physics, Vol. 32, No. 14, pp. L49-L52, 1999.

[66] C. Canalias, V. Pasiskevicius, M. Fokine, and F. Laurell. Backward quasi-phase-matched second-harmonic generation in submicrometer periodically poled flux-grown $KTiOPO_4$. Applied Physics Letters, Vol. 86, pp. 181105, 2005.

[67] K. Fradkin-Kashi, A. Arie, P. Urenski, and G. Rosenman. Characterization of optical and nonlinear properties of periodically-poled $RbTiOAsO_4$ in the mid-infrared range via difference-frequency generation. Applied Physics B, Vol. 71, pp. 251, 2000.

[68] M. Kawaji, K. Imura, T. Yaguchi, and I. Shoji. Fabrication of Quasi-Phase-Matched Devices by Use of the Room-Temperature-Bonding Technique. Advanced Solid-State Photonics, paper TuB24, 2009.

[69] R. V. Gainutdinov, T. R. Volk, O. a. Lysova, I. I. Razgonov, A. L. Tolstikhina, and L. I. Ivleva. Recording of domains and regular domain patterns in strontium barium niobate crystals in the field of atomic force microscope. Applied Physics B, Vol. 95, Iss. 3, pp. 505-512, 2009.

[70] M. O. Ramirez. Evaluation of ytterbium doped strontium barium niobate as a potential tunable laser crystal in the visible. Journal of Applied Physics, Vol. 95, Iss. 11, pp. 6185, 2004.

[71] V. V. Shvartsman, W. Kleemann, T. Lukasiewicz, and J. Dec. Nanopolar structure in $Sr_xBa_{1-x}Nb_2O_6$ single crystals tuned by Sr/Ba ratio and investigated by piezoelectric force microscopy. Physical Review B, Vol. 77, Iss. 5, pp. 1-7, 2008.

[72] K. Terabe, S. Takekawa, M. Nakamura, K. Kitamura, S. Higuchi, Y. Gotoh, and A. Gruverman. Imaging and engineering the nanoscale-domain structure of a $Sr_{0.61}Ba_{0.39}Nb_2O_6$ crystal using a scanning force microscope. Applied Physics Letters, Vol. 81, Iss. 11, pp. 2044, 2002.

[73] P. Molina, M. O. Ramírez, and L. E. Bausá. Strontium Barium Niobate as a Multifunctional Two-Dimensional Nonlinear Photonic Glass. Advanced Functional Materials, Vol. 18, Iss. 5, pp. 709-715, 2008.

[74] M. H. Francombe. The relation between structure and ferroelectricity in lead barium and barium strontium niobates. Acta Crystallographica, Vol. 13, pp. 131-140, 1960.

[75] B. Jaffe, W. R. Cook Jr., and H. Jaffe. Piezoelectric Ceramics. Academic press, New York, pp. 213, 1971.

[76] A. M. Glass. Investigation of the electrical properties of $Sr_xBa_{1-x}Nb_2O_6$ with special reference to pyroelectric detection. Journal of Applied Physics, Vol. 40, pp. 4699, 1969.

[77] R. R. Neurgaonkar, and W. K. Cory. Progress in photorefractive tungsten bronze crystals. Journal of the Optical Society of America B: Optical Physics, Vol. 3, Iss. 2, pp. 274-282, 1986.

[78] M. D. Ewbank, R. R. Neurgaonkar and W. K. Cory, J. Feinberg. Photorefractive properties of strontium barium niobate. Journal of Applied Physics, Vol. 62, Iss. 2, pp. 374, 1987.

[79] D. Rytz, B. A. Wechsler, M. H. Garrett, C. C. Nelson, and R. N. Schwartz. Photorefractive properties of $BaTiO_3$: Co. Journal of the Optical Society of America B, Vol. 7, Iss. 12, pp. 2244-2254, 1990.

[80] M. Horowitz, A. Bekker, and B. Fischer. Image and fixing method with $Sr_xBa_{1-x}Nb_2O_6$ crystals. Applied Physics Letters, Vol. 18, Iss. 22, pp.1964-1966, 1993.

[81] J. J. Romero, D. Jaque, J. Garcia Sole, and A. A. Kaminskii. Simultaneous generation of coherent light in the three fundamental colors by quasi cylindrical ferroelectric domains in $Sr_{0.6}Ba_{0.4}(NbO_3)_2$. Applied Physics Letters, Vol. 81, pp.4106-4108, 2002.

[82] J. J. Romero, C. Arago, J. A. Gonzalo, D. Jaque, and J. Garcia Sole. Spectral and thermal properties of quasi-phase matching second harmonic generation in Nd^{3+}: $Sr_{0.6}Ba_{0.4}(NbO_3)_2$ multi-self-frequency-converter nonlinear crystals. Journal of Applied Physics, Vol. 93, pp.3111-3113, 2003.

[83] M. O. Ramirez, J. J. Romero, P. Molina, and L. E. Bausa. Near infrared and visible tunability from a diode pumped Nd^{3+} activated strontium barium niobate laser crystal. Applied Physics B, Vol. 81, pp.827-830, 2005.

[84] W. Wang, V. Roppo, K. Kalinowski, Y. Kong, D. N. Neshev, C. Cojocaru, J. Trull, R. Vilaseca, K. Staliunas, W. Krolikowski, S. M. Saltiel, and Y. S. Kivshar. Third-harmonic generation via broadband cascading in disordered quadratic nonlinear media. Optics Express, Vol. 17, Iss. 22, pp. 20117-20123, 2009.

[85] W. Wang, K. Kalinowski, V. Roppo, Y. Sheng, K. Koynov, Y. Kong, C. Cojocaru, J. Trull, R. Vilaseca and W. Krolikowski. Second- and third-harmonic parametric scattering in disordered quadratic media. Journal of Physics B: Atomic, Molecular and Optical Physics, Vol. 43, No. 21, pp. 215404, 2010.

[86] A. R. Tunyagi, M. Ulex, and K. Betzler. Noncollinear optical frequency doubling in strontium barium niobate. Physical Review Letters, Vol. 90, pp. 243901, 2003.

[87] J. Trull, C. Cojocaru, R. Fischer, S. M. Saltiel, K. Staliunas, R. Vilaseca, D. N. Neshev, W. Krolikowski, and Y. S. Kivshar. Second harmonic parametric scattering in ferroelectric crystals with disordered nonlinear domain structures. Optics Express, Vol. 15, pp. 15868-15877, 2007.

[88] V. Roppo, D. Dumay, J. Trull, C. Cojocaru, S. M. Saltiel, K. Staliunas, R. Vilaseca, D. N. Neshev, W. Krolikowski, and Y. S. Kivshar. Planar second harmonic generation with noncollinear pumps in disordered media. Optics Express, Vol. 16, pp. 14192-14199, 2008.

[89] R. Fischer, D. N. Neshev, S. M. Saltiel, W. Krolikowski, and Y. S. Kivshar. Broadband femtosecond frequency doubling in random media. Applied Physics Letters, Vol. 89, pp. 191105, 2006.

[90] R. Fischer, D. N. Neshev, S. M. Saltiel, A. A. Sukhorukov, W. Krolikowski, and Y. S. Kivshar. Monitoring ultrashort pulses by the transverse frequency doubling of counterpropagating pulses in random media. Applied Physics Letters, Vol. 91, pp. 031104, 2007.

[91] W. Sakamoto, T. Yogo, K. Kikuta, L. Ogiso, A. Kawase, and S. Hirano. Synthesis of strontium barium niobate thin films through metal alkoxide. Journal of the American Ceramic Society, Vol. 79, Iss. 9, pp. 2283-2288, 1996.

[92] Y. Qu, A. Li, Q. Shao, Y. Tang, D. Wu, C. L. Mak, K. H. Wong and N. Ming. Structure and electrical properties of strontium barium niobate ceramics. Materials Research Bulletin, Vol. 37, pp. 503-513, 2002.

[93] S. P. Mahulikar, H. R. Sonawane, and G. A. Rao. Infrared signature studies of aerospace vehicles. Progress in Aerospace Science, Vol. 43, pp. 218-245, 2007.

[94] H. Amrania, A. McCrow, and C. Phillips. A benchtop, ultrafast infrared spectroscopic imaging system for biomedical applications. Review of Scientific Instruments, Vol. 80, pp. 123702, 2009.

[95] Z. Chen, L. Cao, B. Wang, X. Zhuang, N. Chen, and R. Guo. Outfield experiment research of mid-wave infrared detecting system by long distance mid-infrared laser. Infrared and Laser Engineering, Vol. 42, pp. 1700, 2013.

[96] P. S. Kuo. Thick film, orientation-patterned gallium arsenide for nonlinear optical frequency conversion. PhD thesis, Stanford University, 2008.

[97] L. P. Gonzalez, D. C. Upchurch, P. G. Schunemann, L. Mohokern, and S. Guha. Second harmonic generation of a tuneable continuous wave CO_2 laser in orientation-patterned GaAs. Optics Letters, Vol .38, pp. 320-322, 2013.

[98] M. Eichhorn. Quasi-three-level solid-state lasers in the near and mid infrared based on trivalent rare earth ions. Applied Physics B: Lasers and Optics, Vol. 93, pp. 269-316, 2008.

[99] T. A. Cool, R. R. Stephens, and J. A. Shirley. HCL, HF, and DF partially inverted CW chemical lasers. Journal of Applied Physics, Vol. 41, pp. 4038, 1970.

[100] Y. Yao, A. J. Hoffman, and C. F. Gmachl. Mid-infrared quantum cascade lasers. Nature Photonics, Vol. 6, pp. 432-439, 2012.

[101] S. D. Jackson. Towards high-power mid-infrared emission from a fibre laser. Nature Photonics, Vol. 6, pp. 423-431, 2012.

[102] Y. Sheng, W. Wang, K. Kalinowski, K. Koynov, and W. Krolikowski. Broadband third-harmonic generation in two-dimensional short-range ordered nonlinear photonic structure. Applied Physics B: Lasers and Optics, Vol. 103, Iss. 1, pp. 13-16, 2011.

[103] H. Hübel, D. R. Hamel, A. Fedrizzi, S. Ramelow, K. J. Resch, and T. Jennewein. Direct generation of photon triplets using cascaded photon-pair sources. Nature, Vol. 466, pp. 601-603, 2010.

[104] N. V. Bloch, K. Shemer, A. Shapira, R. Shiloh, I. Juwiler, and A. Arie. Twisting Light by Nonlinear Photonic Crystals, Physical Review Letters, Vol. 108, pp. 233902, 2012.

[105] H. Y. Leng, X. Q. Yu, Y. X. Gong, P. Xu, Z. D. Xie, H. Jin, C. Zhang, and S. N. Zhu. On-chip steering of entangled photons in nonlinear photonic crystals. Nature communications, Vol. 2, pp. 429, 2011.

[106] L. E. Myers, R. C. Eckardt, M. M. Fejer, R. L. Byer, and W. R. Bosenberg. Multigrating quasi-phase-matched optical parametric oscillator in periodically poled $LiNbO_3$. Optics Letters, Vol. 21, Iss. 8, pp. 591-593, 1996.

[107] P. E. Powers, Thomas J. Kulp, and S. E. Bisson. Continuous tuning of a continuous-wave periodically poled lithium niobate optical parametric oscillator by use of a fan-out grating design. Optics Letters, Vol. 23, Iss. 3, pp. 159-161, 1998.

[108] K. Kintaka, M. Fujimura, T. Suhara, and H. Nishihara. Third harmonic generation of Nd:YAG laser light in periodically poled $LiNbO_3$ waveguide. Electronics Letters. Vol. 33, Iss. 17, pp. 1459-1461, 1997.

[109] W. R. Bosenberg, J. I. Alexander, L. E. Myers, and R. W. Wallace. 2.5 W, continuous wave, 629 nm solid-state laser source. Advanced Solid State Lasers, Optical Society of America, pp. VL9, 1998.

[110] S. N. Zhu, Y. Y. Zhu, and N. B. Ming. Quasi-phase-matched third-harmonic generation in a quasi-periodic optical superlattice. Science, Vol. 278, Iss. 5339, pp. 843-846, 1997.

[111] M. H. Chou. Multiple-channel wavelength conversion by use of engineered quasi-phase-matching structures in $LiNbO_3$ waveguides. Optics Letters, Vol. 24, Iss. 16, pp. 1157-1159, 1999.

[112] M. A. Arbore, A. Galvanauskas, D. Harter, M. H. Chou, and M. M. Fejer. Engineerable compression of ultrashort pulses by use of second-harmonic generation in chirped-period-poled lithium niobate. Optics Letters, Vol. 22, Iss. 17, pp. 1341-1343, 1997.

[113] H. Norton and C. M. De Sterke. Aperiodic 1-dimensional structures for quasi-phase matching. Optics Express, Vol. 12, Iss. 5, pp. 841-846, 2004.

[114] V. Berger. Nonlinear photonic crystals. Pysical Review Letters, Vol. 81, No. 19, pp. 4136-4139, 1998.

[115] N. G. R. Broderick, G. W. Ross, H. L. Offerhaus, D. J. Richardson, and D. C. Hanna. Hexagonally Poled Lithium Niobate: A Two-Dimensional Nonlinear Photonic Crystal. Pysical Review Letters, Vol. 84, No. 19, pp. 4345-4348, 2000.

[116] A. Chowdhury, C. Staus, B. F. Boland, T. F. Kuech, and L. McCaughan. Experimental demonstration of 1525-1555 nm simultaneous optical wavelength interchange with a nonlinear photonic crystal. Optics Letters, Vol. 26, pp. 1353, 2001.

[117] N. G. R. Broderick, R. T. Brafalean, T. M. Monro, D. J. Richardson, and C. M. de Sterke. Temperature and wavelength tuning of second-, third-, and fourth-harmonic generation in a two-dimensional hexagonally poled nonlinear crystal. Journal of the Optical Society of America B, Vol. 19, pp. 2263, 2002.

[118] S. Saltiel and Y. S. Kivshar. Phase matching in nonlinear $\chi^{(2)}$ photonic crystals. Optics Letters, Vol. 25, pp. 1204-1206, 2000.

[119] S. Saltiel and Y. S. Kivshar. All-optical deflection and splitting by second-order cascading. Optics Letters, Vol. 27, pp. 921, 2002.

[120] M. Baudrier-Raybaut, R. Haidar, P. Kupecek, P. Lemasson, and E. Rosencher. Random quasi-phase-matching in bulk polycrystalline isotropic nonlinear materials. Nature, Vol. 432, Iss. 7015, pp. 374–376, 2004.

[121] Y. Sheng, J. Dou, B. Ma, B. Cheng, and D. Zhang. Broadband efficient second harmonic generation in media with a short-range order. Applied Physics Letters, Vol. 91, Iss. 1, pp. 011101, 2007.

[122] Y. Sheng, S. M. Saltiel, and K. Koynov. Cascaded third harmonic generation in a single short-range-ordered nonlinear photonic crystal. Optics Letters, Vol. 34, Iss. 5, pp. 656-658, 2009.

[123] K. Shemer, N. V. Bloch, A. Shapira, A. Libster, I. Juwiler, and A. Arie. Azimuthal and radial shaping of vortex beams generated in twisted nonlinear photonic crystals. Optics Letters, Vol. 38, No. 24, pp. 5470-5473, 2013.

[124] N. Voloch, T. Ellenbogen, and A. Arie. Radially symmetric nonlinear photonic crystals. Journal of the Optical Society of America B, Vol. 26, No. 1, pp. 42-49, 2009.

[125] A. Arie and N. Voloch. Periodic, quasi-periodic, and random quadratic nonlinear photonic crystals. Laser & Photonics Review, Vol. 4, No. 3, pp. 355-373, 2010.

[126] T. Ellenbogen, N. Voloch-Bloch, A. Ganany-Padowicz, and A. Arie. Nonlinear generation and manipulation of Airy beams. Nature Photonics, Vol. 3, pp. 395-398, 2009.

[127] D. Feng, N. B. Ming, J. F. Hong, Y. S. Yang, J. S. Zhu, Z. Yang, and Y. N. Wang. Enhancement of second harmonic generation in $LiNbO_3$ crystals with periodic laminar ferroelectric domains. Applied Physics Letters, Vol. 37, pp. 607-609, 1980.

[128] A. Feisst, and P. Koidl. Current induced periodic ferroelectric domain structures in $LiNbO_3$ applied for efficient nonlinear optical frequency mixing. Applied Physics Letters, Vol. 47, Iss. 11, pp. 1125, 1985.

[129] W. S. Wang, Q. Zou, Z. H. Geng, and D. Feng. Study of $LiTaO_3$ crystals grown with a modulated structure. I. Second harmonic generation in $LiTaO_3$ crystals with periodic laminar ferroelectric domains. Journal of Crystal Growth, Vol. 79, pp. 706-709, 1986,

[130] M. M. Fejer, J. L. Nightingale, G. A. Magel, and R. L. Byer. Laser-heated miniature pedestal growth apparatus for single-crystal optical fibers. Review of Scientific Instruments, Vol. 55, Iss. 11, pp. 1791, 1984.

[131] Y. S. Luh, R. S. Feigelson, M. M. Fejer, and R. Byer. Ferroelectric domain structures in $LiNbO_3$ single-crystal fibers. Journal of Crystal Growth, Vol. 78, pp. 125-143, 1986.

[132] J. Webjorn, F.Laurell, and G. Arvidsson. Fabrication of periodically domain inverted channel waveguides in lithium niobite for second harmonic generation. Journal of Lightwave Technology, Vol. 7, 00. 1597-1600, 1989.

[133] J. Webjorn, F.Laurell, and G. Arvidsson. Blue light generated by frequency doubling of laser diode light in a lithium neonate channel waveguide. IEEE Photonics Technology Letters, Vol. 1, pp. 316-318, 1989.

[134] E. J. Lim, M. M. Fejer, and R. L. Byer. Second harmonic generation of green light in periodically poled planar lithium niobate waveguide. Electronics Letters, Vol. 25, pp. 174-175, 1989.

[135] E. J. Lim, M. M. Fejer, R. L. Byer, and W. J. Kozlovsky. Blue light generation by frequency doubling in periodically poled lithium niobate channel waveguide. Electronics Letters, Vol. 25, pp. 731-732, 1989.

[136] E. J. Lim, H. M. Hertz, M. L. Bortz, and M. M. Fejer. Infrared radiation generated by quasi-phase-matched difference frequency mixing in a periodically poled lithium niobate waveguide. Applied Physics Letters, Vol. 59, Iss. 18, pp. 2207, 1991.

[137] J. D. Bierlein, D. B. Laubacher, J. B. Brown, and C. J. van der Poel. Balanced phase matching in segmented $KTiOPO_4$ waveguides. Applied Physics Letters, Vol. 56, pp. 1725-1727, 1990.

[138] C. J. van der Poel, J. D. Bierlein, J. B. Brown Co., and S. Colak. Efficient type I blue second harmonic generation in periodically segmented $KTiOPO_4$ waveguides. Applied Physics Letters, Vol. 57, pp. 2074-2076, 1990.

[139] S. Matsumoto, E. J. Lim, H. M. Hertz, and M. M. Fejer. Quasi phase-matched second harmonic generation of blue light in electrically periodically-poled lithium tantalate waveguides. Electronics Letters, Vol. 27, Iss. 22, pp. 2040-2042, 1991.

[140] M. Yamada, N. Nada, M. Saitoh, and K. Watanabe. First-order quasi-phase matched $LiNbO_3$ waveguide periodically poled by applying an external field for efficient blue second-harmonic generation. Applied Physics Letters, Vol. 62, pp. 435-436, 1993.

[141] L. E. Myers, R. C. Eckardt, M. M. Fejer, R. L. Byer, W. R. Bosenberg, and J. W. Pierce. Quasi-phase-matched optical parametric oscillators in bulk periodically poled $LiNbO_3$. Journal of the Optical Society of America B, Vol. 12, pp. 2102-2116, 1995.

[142] L. E. Myers. Quasi-phase-matched optical parametric oscillators in bulk periodically poled lithium niobate. Ph.D. thesis, Stanford University, 1995.

[143] C. Canalias, V. Pasiskevicius, R. Clemens, and F. Laurell. Submicron periodically poled flux-grown $KTiOPO_4$. Applied Physics Letters, Vol. 82, pp. 4233, 2003.

[144] T. Kishino, R. F. Tavlykaev, and R. V. Ramaswamy. 70+ μm deep domain inversion in X-cut $LiNbO_3$ and its use in a high-speed bandpass integrated-optic modulator. Applied Physics Letters, Vol. 76, pp. 3852, 2000.

[145] F. Genereux, G. Baldenberger, B. Bourliaguet, and R. Vallee. Deep periodic domain inversions in x-cut $LiNbO_3$ and its use for second harmonic generation near 1.5 μ m. Applied Physics Letters, Vol. 91, pp. 231112, 2007.

[146] H. Steigerwald, M. Lilienblum, F. von Cube, Y. J. Ying, R. W. Eason, S. Mailis, B. Sturman, E. Soergel, and K. Buse. Origin of

UV-induced poling inhibition in lithium niobate crystals. Physical Review B, Vol. 82, Iss. 21, pp. 214105, 2010.

[147] C. Y. J. Ying, A. C. Muir, C. E. Valdivia, H. Steigerwald, C. L. Sones, R. W. Eason, E. Soergel, and S. Mailis. Light-mediated ferroelectric domain engineering and micro-structuring of lithium niobate crystals. Laser & Photonics Review, Vol. 6, No. 4, pp. 526–548, 2012.

[148] A. C. Muir, C. L. Sones, S. Mailis, R. W. Eason, T. Jungk, A. Hoffman, and E. Soergel. Direct-writing of inverted domains in lithium niobate using a continuous wave ultra violet laser. Optics Express, Vol. 16, Iss. 4, pp. 2336, 2008.

[149] M. E. Lines and A. M. Glass. Principles and Application of Ferroelectrics and Related Materials. Clarenon Press, 1977.

[150] H. Steigerwald, Y. J. Ying, R. W. Eason, K. Buse, S. Mailis, and E. Soergel. Direct writing of ferroelectric domains on the x-and y-faces of lithium niobate using a continuous wave ultraviolet laser. Applied Physics Letters, Vol. 98, Iss. 6, pp. 062902, 2011.

[151] A. Boes, H. Steigerwald, T. Crasto, S. A. Wade, T. Limboeck, E. Soergel, and A. Mitchell. Tailor-made domain structures on the x- and y-face of lithium niobate crystals. Applied Physics B: Lasers and Optics, Vol. 115, pp. 577-581, 2014.

[152] C. E. Valdivia. Light-induced ferroelectric domain engineering in lithium niobate & lithium tantalite. PhD thesis, University of Southampton, 2007.

[153] S. Mailis, P. T. Brown, C. L. Sones, I. Zergioti, and R. W. Eason. Etch frustration in congruent lithium niobate single crystals induced by femtosecond ultraviolet laser irradiation. Applied Physics A: Materials Science & Processing, Vol. 74, Iss. 2, pp. 135-137, 2002.

[154] P. T. Brown, S. Mailis, I. Zergioti, and R. W. Eason. Microstructuring of lithium niobate single crystals using pulsed UV laser modification of etching characteristics. Optical Materials, Vol. 20, Iss. 2, pp. 125, 2002.

[155] S. Mailis, C. L. Sones, J. G. Scott, and R. W. Eason. UV laser-induced ordered surface nanostructures in congruent lithium niobate single crystals. Applied Surface Science, Vol. 247, Iss. 1-4, pp. 497-503, 2005.

[156] C. L. Sones, C. E. Valdivia, J. G. Scott, S. Mailis, R. W. Eason, D. A. Scrymgeour, V. Gopalan, T. Jungk, and E. Soergel. Ultraviolet laser-induced sub-micron periodic domain formation in congruent undoped lithium niobate crystals. Applied Physics B: Lasers and Optics, Vol. 80, Iss. 3, pp. 341-344, 2005.

[157] N. Ohnishi and T. Iizuka. Etching study of microdomains in LiNbO3 single crystals. Journal of Applied Physics, Vol. 46, Iss. 3, pp. 1063-1067, 1975.

[158] V. Y. Shur, D. K. Kuznetsov, A. I. Lobov, E. V. Nikolaeva, M. A. Dolbilov, A. N. Orlov, and V. V. Osipov. Formation of self-similar surface nano-domain structures in lithium niobate under highly nonequilibrium conditions. Ferroelectrics, Vol. 341, Iss. 1, pp. 85-93, 2006.

[159] M. Fujimura, T. Sohmura, and T. Suhara. Fabrication of domain-inverted gratings in MgO: $LiNbO_3$ by applying voltage under ultraviolet irradiation through photomask at room temperature. Electronics Letters, Vol. 39, Iss. 9, pp. 719-721, 2003.

[160] K. Terabe, M. Nakamura, S. Takekawa, and K. Kitamura. Microscale to nanoscale ferroelectric domain and surface engineering of a near-stoichiometric $LiNbO_3$ crystal. Applied Physics Letters, Vol. 82, No. 3, pp. 433-435, 2003.

[161] L. S. Kokhanchik, R. V. Gainutdinov, S. D. Lavrov, and T. R. Volk. Characteristics of microdomains and microdomain patterns recorded by electron beam irradiation on Y-cut LiNbO3 crystals. Journal of Applied Physics, Vol. 118, Iss. 7, pp. 072001, 2015.

[162] Y. Furuhata and K. Toriyama. New liquid-crystal method for revealing ferroelectric domains. Applied Physics Letters, Vol. 23, Iss. 7, pp. 361, 1973.

[163] Y. H. Hu, H. M. Chan, X. W. Zhang, M. P. Harmer. Scanning electron microscopy and transmission electron microscopy study of ferroelectric domains in doped $BaTiO_3$. Journal of the American Ceramic Society, Vol. 69, Iss. 8, pp. 594-602, 1986.

[164] E. Soergel. Visualization of ferroelectric domains in bulk single crystals. Applied Physics B: Lasers and Optics, Vol. 81, pp. 729-752, 2005.

[165] J. A. Hooton and W. J. Merz. Etch Patterns and Ferroelectric Domains in $BaTiO_3$ Single Crystals. Physical Review, Vol. 98, Iss. 2, pp. 409, 1955.

[166] C. L. Sones, S. Mailis, W. S. Brocklesby, R. W. Eason, and J. R. Owen. Differential etch rates in z-cut $LiNbO_3$ for variable HF/HNO_3 concentrations. Journal of Materials Chemistry, Vol. 12, pp. 295-298, 2002.

[167] F. Saurenbach and B. D. Terris. Imaging of ferroelectric domain walls by force microscopy. Applied Physics Letters, Vol, 56, Iss. 17, pp. 1703, 1990.

[168] O. Kolosov, A. Gruverman, J. Hatano, K. Takahashi, H. Tokumoto. Nanoscale visualization and control of ferroelectric domains by atomic force microscopy. Physical Review Letters, Vol. 74, pp. 4309, 1995.

[169] C. Gao, F. Duewer, Y. Lu and X. D. Xiang. Quantitative nonlinear dielectric microscopy of periodically polarized ferroelectric domains. Applied Physics Letters, Vol. 73, Iss. 8, pp. 1146, 1998.

[170] Y. Cho, K. Fujimoto, Y. Hiranaga, Y. Wagatsuma, A. Onoe, K. Terabe and K. Kitamura. Tbit/inch^2 ferroelectric data storage based on scanning nonlinear dielectric microscopy. Applied Physics Letters, Vol. 81, Iss. 23, pp. 4401, 2002.

[171] J. V. Jelley. Cerenkov radiation and its applications. New York: Pergamon Press, 1958.

[172] Y. Sheng, A. Best, H. Butt, W. Krolikowski, A. Arie, and K. Koynov. Three-dimensional ferroelectric domain visualization by Čerenkov-type second harmonic generation. Optics Express, Vol. 16, pp. 16539-16545, 2010.

[173] M. Ayoub, H. Futterlieb, J. Imbrock and C. Denz. 3D Imaging of ferroelectric kinetics during electrically driven switching. Advanced Materials, Vol. 29, Iss. 5, pp. 1603325, 2017.

[174] J. Thomas, V. Hilbert, R. Geiss, T. Pertsch, A. Tunnermann, and S. Nolte. Quasi phase matching in femtosecond pulse volume structured x-cut lithium niobate. Laser & Photonics Review. Vol. 7, Iss. 3, pp. L17-L20, 2013.

[175] A. Boes, H. Steigerwald, D. Yudistira, V. Sivan, S. Wade, S. Mailis, E. Soergel, and A. Mitchell. Ultraviolet laser-induced poling inhibition produces bulk domains in MgO-doped lithium niobate crystals. Applied Physics Letters, Vol. 105, pp. 092904 2014.

[176] S. Zheng, Y. Kong, H. Liu, S. Chen, L. Zhang, S. Liu, and Jingjun Xu. Pyroelectric effect in green light-assisted domain reversal of Mg-doped $LiNbO_3$ crystals. Optics Express, Vol. 20, pp. 29131, 2012.

[177] E. A. Mingaliev, V. Y. Shur, D. K. Kuznetsov, S. A. Negashev, and A. I. Lobov. Formation of stripe domain structures by pulse laser irradiation of $LiNbO_3$ crystals. Ferroelectrics, Vol. 399, Iss. 1, pp. 7-13, 2010.

[178] A. Boes, T. Crasto, H. Steigerwald, S. Wade, J. Frohnhaus, E. Soergel, and A. Mitchell. Direct writing of ferroelectric domains on strontium barium niobate crystals using focused ultraviolet laser light. Applied Physics Letters, Vol. 103, pp. 142904, 2013.

[179] D. Yudistira, A. Boes, A. R. Rezk, L. Y. Yeo, J. R. Friend, and A. Mitchell. UV direct write metal enhanced redox (MER) domain engineering for realization of surface acoustic devices on lithium niobate. Advanced Materials Interfaces, Vol. 1, Iss. 4, pp. 1400006, 2014.

[180] X. Deng and X. Chen. Domain wall characterization in ferroelectrics by using localized nonlinearities. Optics Express, Vol. 18, pp. 15597-15602, 2010.

[181] K. Kalinowski, Q. Kong, V. Roppo, A. Arie, Y. Sheng, and W. Krolikowski. Wavelength and position tuning of Čerenkov second-harmonic generation in optical superlattice. Applied Physics Letters, Vol. 99, pp. 181128, 2011.

[182] Y. Sheng, V. Roppo, K. Kalinowski, and W. Krolikowski. Role of a localized modulation of $\chi^{(2)}$ in Čerenkov second-harmonic generation in nonlinear bulk medium. Optics Letters, Vol. 37, pp. 3864, 2012.

[183] P. Karpinski, X. Chen, V. Shvedov, C. Hnatovsky, A. Grisard, E. Lallier, B. Luther-Davies, W. Krolikowski, and Y. Sheng. Nonlinear diffraction in orientation-patterned semiconductors. Optics Express, Vol. 23, pp. 14903, 2015.

[184] H. Chen, X. Chen, Y. Zhang and Y. Xia. Ablation induced by single-and multiple-femtosecond laser pulses in lithium niobate. Laser Physics, Vol. 17, Iss. 12, pp.1378-1381, 2007.

[185] A. Rosenfeld, M. Lorenz, R. Stoian and D. Ashkenasi. Ultrashort-laser-pulse damage threshold of transparent materials and the role of incubation. Applied Physics A, Vol. 69, Supplement 1, pp. S373-376, 1999.

[186] S. Juodkazis, M. Sudzius, V. Mizeikis, H. Misawa, E. Gamaly, Y. Liu, O. Louchev, and K. Kitamura. Three-dimensional recording by tightly focused femtosecond pulses in $LiNbO_3$ crystal. Applied Physics Letters, Vol. 89, pp. 062903, 2006.

[187] S. Fahy and R. Merlin. Reversal of ferroelectric domains by ultrashort optical pulses. Physical Review Letters, Vol. 73, pp. 1122, 1994.

[188] H. Lao, H. Zhu, and X. Chen. Threshold fluence for domain reversal directly induced by femtosecond laser in lithium niobate. Applied Physics A, Vol. 101, pp. 313, 2010.

[189] G. Zhou, A. Jesacher, M. Booth, T. Wilson, A. Rodenas, D. Jaque, and M. Gu. Axial birefringence induced focus splitting in lithium niobate. Optics Express, Vol. 17, pp. 17970, 2009.

[190] M. Gu. Advanced Optical Imaging Theory. Springer, 2000.

[191] B. P. Cumming, A. Jesacher, M. J. Booth, T. Wilson, and M. Gu. Adaptive aberration compensation for three-dimensional micro-fabrication of photonic crystals in lithium niobate. Optics Express, Vol. 19, pp. 9419, 2011.

[192] S. Kroesen, K. Tekce, J. Imbrock, and C. Denz. Monolithic fabrication of quasi phase-matched waveguides by femtosecond laser structuring the $\chi^{(2)}$ nonlinearity. Applied Physics Letters, Vol. 107, pp. 101109, 2015.

[193] X. Chen, P. Karpinski, V. Shvedov, K. Koynov, B. Wang, J. Trull, C. Cojocaru, W. Krolikowski, and Y. Sheng. Ferroelectric domain engineering by focused infrared femtosecond pulses. Applied Physics Letters, Vol. 107, pp. 141102, 2015.

[194] D. H. Jundt. Temperature-dependent Sellmeier equation for the index of refraction, ne, in congruent lithium niobate. Optics Letters, Vol. 22, pp. 1553, 1997.

[195] G. Imeshev, M. A. Arbore, M. M. Fejer, A. Galvanauskas, M. Fermann, and D. Harter. Ultrashort-pulse second-harmonic generation with longitudinally nonuniform quasi-phase-matching gratings: pulse compression and shaping. Journal of the Optical Society of America B, Vol. 17, pp. 304, 2000.

[196] J. Comly and E. Germire. Second harmonic generation from short pulses. Applied Physics Letters, Vol. 12, pp. 7, 1968.

[197] Z. Huang, C. Tu, S. Zhang, Y. Li, F. Lu, Y. Fan, and E. Li. Femtosecond second-harmonic generation in periodically poled lithium niobate waveguides written by femtosecond laser pulses. Optics Letters, Vol. 35, pp. 877, 2010.

[198] A. M. Weiner. Effect of group velocity mismatch on the measurement of ultrashort optical pulses via second harmonic generation. IEEE Journal of Quantum Electron, Vol. 19, pp. 1276, 1983.

[199] M. M. Fejer, G. A. Magel, D. H. Jundt, and R. L. Byer. Quasi-phase-matched second harmonic generation: tuning and tolerances. IEEE Journal of Quantum Electron. Vol. 28, pp. 2631, 1992.

[200] J. Valasek. Piezo-electric and allied phenomena in Rochelle salt. Physical Review, Vol. 17, pp. 475, 1921.

[201] D. Li and D. A. Bonnell. Controlled patterning of ferroelectric domains: fundamental concepts and applications. Annual Review of Materials Research, Vol. 38, pp. 351-368, 2008.

[202] Y. Sheng, D. Ma, M. Ren, W. Chai, Z. Li, K. Koynov, and W. Krolikowski. Broadband second harmonic generation in one-dimensional randomized nonlinear photonic crystal. Applied Physics Letters, Vol. 99, pp. 031108, 2011.

[203] I. Varon, G. Porat, and A. Arie. Controlling the disorder properties of quadratic nonlinear photonic crystals. Optics Letters, Vol. 36, pp. 3978, 2011.

[204] L. E. Cross. Relaxor ferroelectrics. Ferroelectrics, Vol. 76, Iss. 1, pp. 241-267, 1987.

[205] M. Ramirez, D. Jaque, L. Bausa, J. Garcia Sole, and A. Kaminskii. Coherent Light Generation from a Nd: SBN Nonlinear Laser Crystal through its Ferroelectric Phase Transition. Physical Review Letters, Vol. 95, pp. 267401, 2005.

[206] M. Eßer, M. Burianek, D. Klimm, and M. Mühlberg. Single crystal growth of the tetragonal tungsten bronze $Ca_xBa_{1-x}Nb_2O_6$ (x= 0.28; CBN-28). Journal of Crystal Growth, Vol. 240, Iss. 1, pp. 1-5, 2002.

[207] W. L. Gao, H. J. Zhang, D. Liu, and M. Xu. Growth and characterization of Nd-doped $Ca_{0.28}Ba_{0.72}Nb_2O_6$ crystal. Journal of Applied Physics, Vol. 105, pp. 023507, 2009.

[208] S. N. Gvasaliya, R. A. Cowley, L. I. Ivleva, S. G. Lushnikov, B. Roessli, and A. Zheludev. Random fields or domain walls of uniaxial disordered ferroelectric SBN. arXiv:1206.2012, 2012.

[209] P. Molina, Á. Garca, M. O. Ramírez, J. García-Solé, L. E. Bausá, H. Zhang, W. Gao, J. Wang, and M. Jiang. Nonlinear prism based on the natural ferroelectric domain structure in calcium barium niobate. Applied Physics Letters, Vol. 94, pp. 071111, 2009.

[210] H. H. Yu, H. J. Zhang, Z. P. Wang, H. H. Xu, Y. C. Wang, J. Y. Wang, and V. Petrov. Manifestation of quantum disordered wave functions with weak localization from conical second harmonic generation in ferroelectric crystal. Applied Physics Letters, Vol. 100, pp. 061119, 2012.

[211] W. L. Gao, G. Q. Xie, J. Ma, P. Yuan, L. J. Qian, J. Q. Di, X. D. Xu, J. Xu, and M. A. Swirkowicz. Self-frequency conversion laser in Nd-doped calcium barium niobate ferroelectric crystal. IEEE Photonics Technology Letters, Vol. 25, pp. 1405, 2013.

[212] V. Roppo, K. Kalinowski, Y. Sheng, W. Krolikowski, C. Cojocaru, and J. Trull. Unified approach to Čerenkov second harmonic generation. Optics Express, Vol. 21, pp. 25715, 2013.

[213] Y. Sheng, W. Wang, R. Shiloh, V. Roppo, Y. Kong, A. Arie, and W. Krolikowski. Cerenkov third-harmonic generation in $\chi^{(2)}$ nonlinear photonic crystal. Applied Physics Letters, Vol. 98, Iss. 24, pp. 241114, 2011.

[214] C. D. Chen, J. Lu, Y. H. Liu, X. P. Hu, L. N. Zhao, Y. Zhang, G. Zhao, Y. Yuan, and S. N. Zhu. Cerenkov third-harmonic generation via cascaded $\chi^{(2)}$ processes in a periodic-poled $LiTaO_3$ waveguide. Optics Letters, Vol. 36, Iss. 7, pp. 1227-1229, 2011.

[215] M. Ayoub, P. Roedig, J. Imbrock, and C. Denz. Cascaded Cerenkov third-harmonic generation in random quadratic media. Applied Physics Letters, Vol. 99, Iss. 24, pp. 241109, 2011.

[216] L. Mateos, P. Molina, J. Galisteo, C. Lopez, L. E. Bausa, M. O. Ramirez. Simultanoeus generation of second to fifth harmonic conical beam in a two-dimensional nonlinear photonic crystal. Optics Express, Vol. 20, Iss. 28, pp. 29940-29948, 2012.

[217] D. E. Zelmon, D. L. Small, and D. Jundt. Infrared corrected Sellmeier coefficients for congruently grown lithium niobate and 5% magnesium oxide-doped lithium niobate. Journal of the Optical Society of America B, Vol. 14, Iss. 12, pp. 3219-3222, 1997.

[218] M. M. Choy and R. L. Byer. Accurate second-order susceptibility measurements of visible and infrared nonlinear crystals. Physical Review B, Vol. 14, pp. 1693-1706, 1976.

[219] P. S. Kuo, J. Bravo-Abad, and G. S. Solomon. Second-harmonic generation using 4-quasi-phasematching in a GaAs whispering-gallery-mode microcavity. Nature Communications, Vol. 5, pp. 3109, 2014.

[220] A. Grisard, E. Lallier, and B. Gerard. Quasi-phase-matched gallium arsenide for versatile mid-infrared frequency conversion. Optical Materials Express, Vol. 2, pp. 1020-1025, 2012.

[221] K. Suto, T. Sasaki, T. Tanabe, K. Saito, J. Nishizawa, and M. Ito. GaP THz wave generator and THz spectrometer using Cr: Forsterite lasers. Review of Scientific Instruments, Vol. 76, pp. 123109, 2005.

[222] K. D. Greve, L. Yu, P. L. McMahon, J. S. Pelc, C. M. Natarajan, N. Y. Kim, E. Abe, S. Maier, C. Schneider, M. Kamp, S. Hoefling, R. H. Hadfield, A. Forchel, M. M. Fejer, and Y. Yamamoto. Quantum-dot spin-photon entanglement via frequency down-conversion to telecom wavelength. Nature, Vol. 491, pp. 421-426, 2012.

[223] O. Wada. Femtosecond all-optical devices for ultrafast communication and signal processing. New Journal of Physics, Vol. 6, pp. 183, 2004.

[224] M. Nikodem, D. Weidmann, and G. Wysocki. Chirped laser dispersion spectroscopy with harmonic detection of molecular spectra. Applied Physics B, Vol. 109, pp. 477-483, 2012.

[225] A. Helmy, P. Abolghasem, J. Stewart Aitchison, B. Bijlani, J. Han, B. Holmes, D. Hutchings, U. Younis, and S. Wagner. Recent advances in phase matching of second-order nonlinearities in monolithic semiconductor waveguides. Laser & Photonics Review, Vol. 5, pp. 272-286, 2011.

[226] R. Lodenkamper, M. L. Bortz, M. M. Fejer, K. Bacher, and J. S. Harris. Surface-emitting second-harmonic generation in a semiconductor vertical resonator. Optics Letters, Vol. 18, pp. 1798-1800, 1993.

[227] T. Skauli, K. L. Vodopyanov, T. J. Pinguet, A. Schober, O. Levi, L. A. Eyres, M. M. Fejer, J. S. Harris, B. Gerard, L. Becouarn, E. Lallier, and G. Arisholm. Measurement of the nonlinear coefficient of orientation-patterned GaAs and demonstration of highly efficient

second-harmonic generation. Optics Letters, Vol. 27, pp. 628-630, 2002.

[228] L. Becouarn, E. Lallier, M. Brevignon, and J. Lehoux. Cascaded second-harmonic and sum-frequency generation of a CO2 laser by use of a single quasi-phase-matched GaAs crystal. Optics Letters, Vol. 23, pp. 1508-1510, 1998.

[229] G. Bloom, A. Grisard, E. Lallier, C. Larat, M. Carras, and X. Marcadet. Optical parametric amplification of a distributed-feedback quantum-cascade laser in orientation-patterned GaAs. Optics Letters, Vol. 35, pp. 505-507, 2010.

[230] P. S. Kuo, K. L. Vodopyanov, M. M. Fejer, D. M. Simanovskii, X. Yu, J. S. Harris, D. Bliss, and D. Weyburne. Optical parametric generation of a mid-infrared continuum in orientation-patterned GaAs. Optics Letters, Vol. 31, pp. 71-73, 2006.

[231] J. Schaar, K. Vodopyanov, P. Kuo, M. Fejer, X. Yu, A. Lin, J. S. Harris, D. Bliss, C. Lynch, V. Kozlov, and W. Hurlbut. Terahertz sources based on intracavity parametric down-conversion in quasi-phase-matched gallium arsenide. IEEE Journal of Selected Topics in Quantum Electronics, Vol. 14, pp. 354-362, 2008.

[232] W. Wang, Y. Sheng, Y. Kong, A. Arie, and W. Krolikowski. Multiple Cerenkov second-harmonic waves in a two-dimensional nonlinear photonic structure. Optics Letters, Vol. 35, pp. 3790-3792, 2010.

[233] E. Megidish, A. Halevy, H. S. Eisenberg, A. Ganany-Padowicz, N. Habshoosh, and A. Arie. Compact 2D nonlinear photonic crystal source of beamlike path entangledphotons. Optics Express, Vol. 21, pp. 6689-6696, 2013.

[234] D. Faye, A. Grisard, E. Lallier, B. Gerard, M. Avella, and J. Jimenez. Distribution of point defects in orientation-patterned GaAs crystals: A cathodoluminescence study. Applied Physics Letters, Vol. 93, pp. 151115, 2008.

[235] D. Faye, E. Lallier, A. Grisard, and B. Gerard. Thick low-loss Orientation-Patterned Gallium Arsenide (OP-GaAs) samples for Mid-Infrared Laser Sources. Proceedings Volume 6740, Optical Materials in Defence Systems Technology IV, 67400I, 2007.

[236] L. A. Eyres, P. J. Tourreau, T. J. Pinguet, C. B. Ebert, J. S. Harris, M. M. Fejer, L. Becouarn, B. Gerard, and E. Lallier. All-epitaxial fabrication of thick, orientation-patterned GaAs films for nonlinear optical frequency conversion. Applied Physics Letters, Vol. 79, pp. 904-906, 2001.

[237] E. Gil-Lafon, J. Napierala, D. Castelluci, A. Pimpinelli, R. Cadoret, and B. Gerard. Selective growth of GaAs by HVPE: keys for accurate control of the growth morphologies. Journal of Crystal Growth, Vol. 222, pp. 482-496, 2001.

[238] Y. Yu, X. Gai, P. Ma, D. Y. Choi, Z. Yang, R. Wang, S. Debbarma, S. Madden, and B. Luther-Davies. A broadband, quasi-continuous, mid-infrared supercontinuum generated in a chalcogenide glass waveguide. Laser & Photonics Review, Vol. 8, pp. 792-798, 2014.

[239] Y. Sheng, Q. Kong, W. Wang, K. Kalinowski, and W. Krolikowski. Theoretical investigations of nonlinear Raman-Nath diffraction in

the frequency doubling process. Journal of Physics B: Atomic, Molecular and Optical Physics, Vol.45, pp. 055401, 2012.

[240] M. Bass, C. DeCusatis, J. Enoch, V. Lakshminarayanan, G. Li, C. MacDonald, V. Mahajan, and E. Van Stryland. Optical Properties of Materials. Nonlinear Optics, Quantum Optics, Vol. 4 of Handbook of Optics, 3rd edition, McGraw-Hill Education, 2009.